
Electronic Theses and Dissertations, 2020-

2020

Refining the Data Collection Methodology of Outdoor Forensic Scenes Involving Scattered Human Remains Using Close-Range Photogrammetry

Megan Mccollum
University of Central Florida



Part of the [Biological and Physical Anthropology Commons](#)

Find similar works at: <https://stars.library.ucf.edu/etd2020>

University of Central Florida Libraries <http://library.ucf.edu>

This Masters Thesis (Open Access) is brought to you for free and open access by STARS. It has been accepted for inclusion in Electronic Theses and Dissertations, 2020- by an authorized administrator of STARS. For more information, please contact STARS@ucf.edu.

STARS Citation

Mccollum, Megan, "Refining the Data Collection Methodology of Outdoor Forensic Scenes Involving Scattered Human Remains Using Close-Range Photogrammetry" (2020). *Electronic Theses and Dissertations, 2020-*. 254.

<https://stars.library.ucf.edu/etd2020/254>



REFINING THE DATA COLLECTION METHODOLOGY OF OUTDOOR
FORENSIC SCENES INVOLVING SCATTERED HUMAN REMAINS USING
CLOSE-RANGE PHOTOGRAMMETRY

by

MEGAN L. MCCOLLUM
B.S. Central Washington University, 2017

A thesis submitted in partial fulfillment of the requirements
for the degree of Master of Arts
in the Department of Anthropology
in the College of Science
at the University of Central Florida
Orlando, Florida

Summer Term
2020

Major Professor: John J. Schultz

© 2020 Megan L. McCollum

ABSTRACT

The documentation of outdoor forensic crime scenes involving human remains poses multiple challenges to law enforcement officials documenting the context of the scene. More rigorous protocols for the documentation of these scenes are needed, and recent advances in technology open up the possibility of three-dimensional (3D) documentation of the scene. More commonly used in archaeological contexts, close-range photogrammetry (CRP) creates reliable 3D models through triangulation of overlapping points between multiple photographs. This documentation technique allows for the preservation of the entire 3D context and the virtual manipulation without evidence destruction. However, CRP has only been preliminarily used in the field of forensic archaeology. To further refine data collection and processing protocols for the use of CRP on forensic scenes, four mock crime scenes on different complex ground surfaces involving a surface scatter of human remains were created. Photographs were collected using a Nikon D7200 camera and processed using Agisoft Metashape Professional. The first scene, a mixed surface dominated by leaves, was used to test the number of images that should be incorporated into a 3D scene. The second (mixed surface dominated by grass), third (mixed surface dominated by pine needles), and fourth (ground surface of mixed leaves and dirt) scenes were used to test data collection techniques, the capability of documenting a scene using CRP on different complex surfaces, as well as to illustrate complex variables that may affect the final model. Accuracy was determined through an estimation of the final root mean square error (RMSE) and visual analysis of qualitative errors. Results show that CRP can be used to accurately and reliably document the 3D context of real-life scenes in a time-efficient and cost-effective manner. This new methodology should be integrated into current forensic crime scene documentation and may eventually replace current methods of mapping the scene context.

To my mom, dad, and sister, who have supported me through everything.

ACKNOWLEDGMENTS

Many people have contributed to both this research and my life during the period of writing this thesis. First, I want to say thank you to my advisor, Dr. John Schultz, who, despite me taking longer than he would like to finish, has been supportive till the end. Thanks to my committee members, Dr. John Walker and Dr. Scott Branting, who always gave valuable insights into this research. Thank you to Ms. Dominique Langis-Barsetti, who, along with Dr. Scott Branting, generously donated their time to come out into the field and help refine the data collection methods and processing methods. Much appreciation also goes out to Mr. John Guziejka for help with facilitating the use of the UCF natural lands for this research. Thank you so much to Ms. Morgan Ferrell, a fellow graduate student who was with us for every step of the field documentation process. As always, I thank my family and friends back home for being so supportive of me my entire life. And finally, a special thanks goes out to fellow graduate students Ms. Julie Rogers and Mrs. Amber Grissom, without whom I most certainly would have gone insane. Amber, thanks for hanging out outside of class and all the convention experiences, both within and outside the state of Florida. Julie, thanks for the comedy, the Netflix binge sessions, Cheddars, hanging out with the dogs, road trips, Universal days, and just generally being there when I needed someone.

TABLE OF CONTENTS

LIST OF FIGURES	viii
LIST OF TABLES	xiii
CHAPTER ONE: INTRODUCTION.....	1
CHAPTER TWO: PROCESSING PROCEDURES AND INFLUENCE OF NUMBERS OF PHOTOGRAPHS ON QUALITATIVE VISUAL ERRORS	6
Introduction.....	6
Background.....	8
Materials and Methods.....	13
Location and Scene Construction	13
Scene Preprocessing and Image Collection	15
Processing in Agisoft Metashape Professional.....	18
Determining accuracy and assessing visual error	35
Results.....	37
Model 1	37
Model 2	43
Model 3	48
Discussion.....	55
Time and weather complications	58
Number of photographs needed	60
Guidelines for integrating CRP.....	61
Conclusions.....	65
CHAPTER THREE: APPLICATION OF PHOTOGRAMMETRY ON DIFFERENT GROUND SURFACES USING DIFFERENT IMAGE COLLECTION TECHNIQUES	66
Introduction.....	66
Background.....	67
Materials and Methods.....	70
Equipment and Scene Preparation	70
Data Collection Methods	72
Model 4	75
Model 5	75
Model 6	76
Pre-processing Photographs.....	77
Processing in Agisoft Metashape.....	77

Post-Processing – measures of error and accuracy	81
Results.....	82
Model 4 – Mixed surface dominated by grass	83
Model 5 – Mixed surface dominated with pine needles	91
Model 6 – Mixed leaves and dirt	98
Discussion.....	106
Data collection methods.....	106
Reducing visual errors	111
Conclusion	113
CHAPTER FOUR: DISCUSSION AND CONCLUSION.....	115
APPENDIX A: PROCESSING REPORTS.....	118
MODEL 1 PROCESSING REPORT	119
MODEL 2 PROCESSING REPORT	126
MODEL 3 PROCESSING REPORT	133
MODEL 4 PROCESSING REPORT	140
MODEL 5 PROCESSING REPORT	147
MODEL 6 PROCESSING REPORT	154
LIST OF REFERENCES	161

LIST OF FIGURES

Figure 1. Location of the mock forensic scenario on the UCF natural lands (red box)..... 14

Figure 2. Examples of the look angles. A) Close-Up Photographs, B) Look Angle 1, C) Look Angle 3, D) Look Angle 4, E) Look Angle 6..... 16

Figure 3. Screenshot of the final Model 1 showing the location where all the photographs were taken from (Blue squares). 17

Figure 4. Generalized linear process of creating a 3D model using Agisoft Metashape Professional 20

Figure 5. Main windows and functions of the Agisoft Metashape Professional interface. The blue arrow is pointing at the drop-down menus that contain all the tools and processing commands. The yellow arrow is pointing at the navigation and view toolbar that controls actions possible in the large viewing window (green box) in the center of the screen. On the left side of the viewing window is the workspace/reference window (red box). The workspace and the reference windows can be selected between the tabs on the bottom of this window (red arrow). The black box shows the photos/console/jobs window directly below the viewing window. These three windows can be selected by choosing the corresponding tab on the bottom of the window (black arrow). 21

Figure 6. Step 1 to add photographs into the Agisoft Metashape Professional program, click on the add photos button in the workspace window. 22

Figure 7. Step 2 to add photos into the Agisoft Metashape Professional software, navigate to the folder where the photos are located, then select all the photographs to create the model, then click the open button 23

Figure 8. Agisoft Metashape Professional interface with photographs added into the program. To begin the estimation of image quality, click the drop-down view menu for the photos window and click “details” to view the detailed view for the photographs..... 23

Figure 9. Details view of the photos window in Agisoft Metashape Professional. To run the Estimation of image quality, select all the photographs in this view, right click and select the “estimate image quality” command 24

Figure 10. Details view of the photos window in Agisoft Metashape Professional. After running the estimation of image quality, a value will appear under the quality column (red box). It is suggested in the Agisoft Metashape Professional (2019) user manual that all photos with a quality of less than .5 should be removed from the program. This is done by selecting the photographs with a value of less than .5, right clicking and pressing the “remove cameras” command. 24

Figure 11. To run the marker registration in Agisoft Metashape Professional, click the "tools" drop-down menu and select "detect markers"..... 25

Figure 12. To create the sparse point cloud (SPC), use the drop-down workflow menu and click the "align photos" command. 25

Figure 13. Step 2 to create the SPC, make sure the accuracy is set to high, that the key point limit is set to 60,000, and the tie point limit is set to 0 and then press “ok” to start processing..... 26

Figure 14. The resulting SPC in the viewing window of Agisoft Metashape Professional. In case any mistakes are made in the optimization, duplicate the chunk by right clicking on the chunk title (red arrow) and choose “Duplicate Chunk”. 26

Figure 15. On the duplicated chunk, the first step in the SPC optimization process is to delete the unneeded points around the scene. Using the selection tool (red arrow) to select the scene boundaries and then inverting the selection by using the “Edit” drop-down menu then selecting “Invert selection” command. Next, delete the outlying points.	28
Figure 16. For further optimization, select the "Model" drop-down menu and click the "Gradual Selection" command.	29
Figure 17. First use the "Reconstruction Uncertainty" command, then the “Projection Accuracy” and finally, the “Reprojection error” optimization commands, repeating the previous step and this one each time.....	29
Figure 18. Reference window of Agisoft Metashape Professional software. During the entire optimization process, the goal is to get the error value (red box) below 1. Photographs that have fewer than 100 projections (blue box) should be removed from the software.	30
Figure 19. After each optimization step, the cameras should be optimized. In the “Tools” drop-down menu, select the “Optimize camera alignment” command. Accept all the default fits and press “OK” to optimize the camera alignment.....	30
Figure 20. To set up the batch process, click on the "Workflow" drop-down menu and select "Batch process".	31
Figure 21. Setting up the batch process to create the 3D model in Agisoft Metashape Professional. Make sure the box is checked to save the project after each step (red arrow). Click on the “Add...” button.	32
Figure 22. First, the dense point cloud must be generated. On the “Job type” drop-down, choose “Build Dense Cloud”, on the “Apply to” drop-down, choose “Selection” to only choose the optimized SPC that was created. In the next section down, under Quality, make sure the value is set to “High” (red arrow). Click “OK”, accepting all other default values.	32
Figure 23. Next, the mesh should be generated. On the “Job type” drop-down menu, choose “Build Mesh”, on the “Apply to” drop-down menu, choose “Selection” then make sure only the optimized chunk is selected. On the “Depth maps quality” property, make sure the value is set to “High” (red arrow). Click “OK” and accept all other default values.....	33
Figure 24. Next, the texture should be generated. On the “Job type” drop-down menu, choose “Build Texture”, on the “Apply to” drop-down menu, choose “Selection” then make sure only the optimized chunk is selected. On the “Texture size” property, change the value to “8192” (red arrow). Click “OK” and accept all other default values.	33
Figure 25. Finally, the orthomosaic should be generated. On the “Job type” drop-down menu, choose “Build Orthomosaic”, on the “Apply to” drop-down menu, choose “Selection” then make sure only the optimized chunk is selected. Click “OK” and accept all default values.	34
Figure 26. Final screen for the batch process set-up. Make sure the box to “Save project after each step” is checked. Click "OK".....	34
Figure 27. Results of the batch process. A) Dense point cloud, B) Mesh, and C) Textured model.	35
Figure 28. Overhead screenshot of Model 1 showing little visual error except on the left tibia (white arrow).....	38

Figure 29. Zoomed in screenshots showing the textured (top) and geometry (bottom) of the head region of Model 1. White arrows indicate areas with poor ground surface-subject interface and the white box indicates an area of scale distortion.....	40
Figure 30. Zoomed in screenshot of the textured (top) and geometry (bottom) area of the torso for Model 1. White boxes indicate the most obvious areas of subject-subject interfacing errors. The one on the left is pointing at the interface between the shirt, vertebrae, and rib. The one on the right indicates the lumbar vertebrae, the shirt and the ground surface. The arrow is pointing to the poor interface between the head of the left humerus and the left scapula.....	41
Figure 31. Zoomed in screenshot of the texture (left) and geometry (right) of the lower leg portion of Model 1. The arrows show poor ground surface-subject interface in the areas of the left ulna (top right) and the unserriated ribs (left). The white box is showing the misrendered geometry of the left tibia.....	42
Figure 32. Overall screenshot of Model 2 showing an accurate representation of all the skeletal elements, clothing, and scales.....	44
Figure 33. Zoomed-in screenshot of the texture (top) and geometry (bottom) of Model 2 showing most of the same visual error as the previous model. White arrows show areas with poor ground surface-subject interface on the ribs (left arrow) and on the cervical vertebrae.....	46
Figure 34. Screenshots of the texture (top) and geometry (bottom) of the torso region of Model 2. White arrows show areas of poor subject-subject interface and ground surface-subject interface in the areas of the vertebrae.....	47
Figure 35. Screenshots of the texture (left) and geometry (right) of the lower leg portion of Model 2. White arrows are pointing out the misrendered geometry on the shafts of the left femur and tibia (on the left) and the ground surface-subject interfacing error on the ribs and the left radius (right).....	48
Figure 36. Overall screenshot of Model 3 showing an accurate representation of all the skeletal elements, clothing, and scales.....	50
Figure 37. Screenshots of the textured (top) and geometry (bottom) of the head section of Model 3. White arrows are pointing out the ground surface-subject interfacing error in the right humerus (left) and the unserriated cervical vertebrae (right).....	51
Figure 38. Screenshots of the texture (top) and geometry (bottom) of the torso region of Model 3. Ground surface-subject interfacing with the scale (Yellow box). The ground surface-subject interface error and misrendered geometry in the ribs (Yellow arrow). Subject-subject and ground surface-subject interfacing errors present in the lower unserriated vertebrae (White boxes).....	52
Figure 39. Screenshots of the texture (left) and geometry (right) layers of the lower leg portion of Model 3. White arrow showing the misrendered geometry on the left tibia, and the white box showing the ground surface-subject interfacing error on the scale bar due to leaf litter covering.....	53
Figure 40. Steps taken during set-up and preprocessing of the scene.....	72
Figure 41. Screenshot from Agisoft Metashape illustrating the look angles.....	74
Figure 42. Screenshots from the Agisoft Metashape Professional software program showing 1) the sparse point cloud, 2) the optimized sparse point cloud, 3) the batch process which consists of 3A) the dense point cloud, 3B) the mesh layer, and 3C) the textured 3D model.....	79

Figure 43. Workflow for processing a 3D model in Agisoft Metashape Professional software. .	80
Figure 44. Overall screenshot of Model 4	85
Figure 45. Zoomed in screenshots of Model 4 showing both the textured (top) and mesh (bottom) models. The oval shows the subject-subject interface issue connecting the manubrium and the body of the sternum, and the arrow shows the misrendered geometry on the right ascending ramus of the mandible.	86
Figure 46. Overhead screenshot of Model 4 in both the textured (top) and mesh (bottom) models. The left arrow shows an area of poor subject-subject interface between two right ribs, and the right arrow shows an area with visual distortion of the texture in the area of the left ribs. The ovals show areas of poor subject-subject interface.	87
Figure 47. Oblique screenshot of the pelvis region of Model 4 showing both the textured (top) and mesh (bottom) models. The arrow is pointing at the misrendered geometry on the ischiopubic ramus of the right os coxa.....	88
Figure 48. Slightly zoomed in overhead screenshot of the lower legs of Model 4 showing both the textured (left) and mesh (right) models. The arrow shows the misrendered geometry in the right femoral shaft and the oval shows the subject-subject interface error between the distal left tibia and the left fibula shaft.....	89
Figure 49. First overall orthophoto of Model 4 showing issues in the orthorectification process in the feet in the upper left corner and the distorted scales in the same area.	90
Figure 50. Second orthophoto generated for Model 4 by manually inspecting and removing photographs from the program. This orthophoto shows improvement in the shadows over the scene as well as the removal of the scale distortion and the feet of the researchers.....	91
Figure 51. Overall screenshot of Model 5 showing accurate visual representation of the scene with little visual distortion.	93
Figure 52. Zoomed in screenshots of Model 5 showing both the textured (top) and mesh (bottom) models. The left arrow shows an area of misrendered geometry on the right ascending ramus of the mandible. The oval shows a subject-subject interfacing error between the manubrium and sternal body, and the right arrow shows ground surface-subject interface error between the axis and the ground surface.	94
Figure 53. Overhead screenshot of Model 5 in both the textured (top) and mesh (bottom) models. The left arrow shows an area of misrendered geometry on the right scapula, the left arrow shows an area of poor subject-subject interface between a left rib and the scale, and the circle shows an area with poor subject-subject interface, poor ground surface-subject interface, and misrendered geometry.....	95
Figure 54. Oblique screenshots of Model 5 showing both the textured (top) and geometry (bottom) models. The oval indicates an area of misrendered geometry on the shorts on top of the left os coxa and the arrow is showing the poor ground surface-subject interface errors between the cranium and the ground surface.....	96
Figure 55. Slightly zoomed in overhead screenshot of the lower legs of Model 5 showing both the textured (left) and mesh (right) models. The arrows show areas of slight misrendered geometry on the left and right tibiae and the oval indicates an area of subject-subject interfacing error between the left femur and pant leg.	97
Figure 56. Orthophoto of Model 5 showing little differences between the orthophoto and the screenshot of the model.....	98

Figure 57. Overall screenshot of Model 6 showing accurate visual representation of the scene with little visual distortion. 99

Figure 58. Zoomed in screenshots of Model 6 showing both the textured (left) and mesh (right) models. The arrows show the ground surface-subject interfacing errors between the cervical vertebrae and the ground surface..... 100

Figure 59. Overhead screenshot of Model 6 in both the textured (left) and mesh (right) models. The ovals show areas of poor subject-subject interface between the right shirt sleeve, the right humerus, and a right rib (top), between a right rib and the left os coxa (center), and between the right os coxa and the short leg (bottom). The arrow shows an area of poor ground surface-subject interface between the scale and the ground surface. 101

Figure 60. Slightly zoomed in oblique screenshots of the head and torso regions of Model 6 shown in both the textured (top) and geometry (bottom) models. The oval shows the area around the right humerus and scapula that show poor subject-subject interface. The arrow shows the misrendered geometry on the ischiopubic ramus of the right os coxa. 102

Figure 61. Slightly zoomed in overhead screenshot of the lower legs of Model 6 showing both the textured (left) and mesh (right) models. The arrows show areas of misrendered geometry on the left and right femora. The white boxes indicate areas where leaves have been moved to cover the scales during data collection, causing ground surface-interfacing errors around the scale bars. 103

Figure 62. Overall orthophoto of Model 6 showing issues in the orthorectification process in the form of dappled shadows from inconsistent lighting, the distortion of scales on the upper left and bottom center scales, and bones that show linear banding causing a double image of the bones (boxes)..... 104

LIST OF TABLES

Table 1. Processing time in Agisoft Metashape Professional for the creation of a 3D model (in hours)	43
Table 2. Summary of the number of photographs excluded from each model.....	54
Table 3. Summary of qualitative visual errors.....	55
Table 4. Summary of the information for models used in Chapter 3.	74
Table 5. Model generation times for chapter 3 models processed in Agisoft Metashape Professional (in hours)	104
Table 6. Visual analysis from the screenshots – summary and comparison table.....	105
Table 7. Summary of some laser scanning and photogrammetry technologies and their cost. ..	116

CHAPTER ONE: INTRODUCTION

The forensic documentation of indoor crime scenes is generally conducted under strict and well-established protocols. In these instances, there are clear standards for the collection of all necessary contextual information, for establishing a chain of custody, and for the determination of forensic significance (Dirkmaat, 2012; Dirkmaat and Cabo, 2016). When the forensic scene is outdoors, variables that affect the scene become much more complex, and documentation becomes much less comprehensive. Both types of crime scenes have the same basic questions that need to be answered; who the individual is, how they got there, how long they have been there, and how they died. However, outdoor crime scenes are generally subjected to many more unpredictable variables than indoor crime scenes (such as temperature, humidity, plants, animals, insects, water, gravity, ground cover, etc.: Mann et al., 1990). These variables can all alter the original context of the scene and thus make it more difficult to recover the required contextual evidence. All of this results in a scene that tends to be much larger and more complex than indoor crime scenes and requires a more in-depth examination of the postmortem alterations that may have occurred, and what the exact agents of these deposition patterns may be (Dirkmaat, 2012; Dirkmaat and Cabo, 2016).

In cases where such an in-depth contextual examination is needed, detailed and complete documentation of the crime scene is paramount for further investigation. In the 1980s, it was recognized that the goal of archaeological site documentation was similar to the goal of forensic scene documentation: to reconstruct past human events by examining the evidence found in a highly altered context (Dirkmaat, 2012; Dirkmaat and Cabo, 2016). Thus, the field of forensic archaeology was created to use well-established and detailed archaeological techniques to document and interpret outdoor forensic crime scenes. These archaeological techniques are

employed in the documentation and search for clandestine graves, surface scatters, and in cases of fire and mass disaster investigations (Dirkmaat and Cabo, 2016). With slight modifications to meet forensic standards, these techniques provide the methods and principles to find, document, and collect forensic evidence and understand distribution patterns through stratigraphy, contextual information, and associations between objects (Schultz and Dupras, 2008; Dirkmaat and Cabo, 2016).

The traditional methodology for this documentation consists of drawn detailed scene maps that are made through processes of measuring and scaling the measurements on paper (Dupras et al., 2012). Two different maps are standard in the detailed drawings, the site plan map that reduces the entire scene to a two-dimensional view from above, and the section drawing, which is meant to show the elevation of objects relative to each other. These section maps consist of two axes, where depth is measured from an arbitrary datum set up by the archaeologist down the mid-line of the site. Despite this attempt to show objects in vertical relation to each other, this type of map still takes a complex, three-dimensional object and turns it into a two-dimensional drawing (Dupras et al., 2012). This same criticism has also been leveled at another traditional documentation process: photography, where three-dimensional real-world objects are represented as two-dimensional photographs (Errickson et al., 2014; Milliet et al., 2014). Because of this simplification, much of the detail and relational information can be lost.

In recent years, with significant advancements in technology, researchers in the field of archaeology have begun using 3D-modelling techniques to represent real-world objects and events digitally. This kind of documentation began with technology such as global positioning system (GPS) data and total station systems which are used to determine 3D coordinates on the spot or to create digital point maps for the location of objects (Dupras et al., 2012). However,

beginning in the early 2000s, the field of archaeology began expanding research methods to include more complex 3D documentation methods. These include laser scanning and photogrammetric methods such as structure-from-motion (SfM) algorithms.

Structure-from-motion (SfM) refers to a set of algorithms within some photogrammetry software that simultaneously determines the camera calibration (how the camera's optical system processes light), and the pose of the camera (the camera's original position and orientation relative to the scene) for every photograph (CHI, 2020). This program results in a sparse point cloud (SPC) that is created from convergent pixel neighborhoods present in multiple photographs of the scene. The precision (or positional uncertainty) of these points is then reduced in an iterative process to refine the virtual 3D representation of the real-world scene. This iterative reduction of the precision of the sparse point cloud increases the precision of the camera calibration and the pose. Once this has been optimized, the SfM process is finished. For photogrammetry, building the SPC is only the beginning step to create a full 3D model. The next step for many software packages is to use multi-viewpoint stereo (MVS) algorithms to build a dense point cloud (DPC: CHI, 2020).

Multi-viewpoint stereo (MVS) algorithms calculate the precise volume of projection points that two or more cameras have in common with each other (CHI, 2020). Projections that are in the same location from multiple cameras occupy the same volume, and the smaller this volume is, the more certain the point's location and precision are. The optimal number for intersection is nine. When nine optimized, posed, and oriented photographs with nine projections intersect, the points will be small, precise, and have low positional uncertainty (CHI, 2020). The resulting visualization is a precise 3D model made of individual points that show an almost solid object on the computer screen. The next few steps to creating a fully textured 3D model rely on

the DPC for the precise location of the objects, and the individual photographs themselves to create an orthographic overlay on the 3D model.

The most common software package used in archaeological research is a program created by Agisoft LLC (e.g., Garstki et al., 2018; Howland et al., 2018; Jalandoni et al., 2018; Jones and Church, 2020; Novotny, 2019; Pierdicca, 2018). The program was previously called Agisoft PhotoScan, but with the newest update (version 1.5), the name was changed to Agisoft Metashape (Agisoft, 2019). Agisoft Metashape allows for the complete integration of the 3D process into one software program in a single linear workflow and provides the bonus of letting the researcher choose the processing and optimization settings after each step. This step-by-step transparency is opposed to programs like 3DF Zephyr, another commercial program in which the researcher plugs in the desired processing values, and a 3D model, is produced automatically as a result (Faulkingham, 2016).

These 3D technologies, and photogrammetry specifically, have only recently been applied to the documentation of forensic crime scenes (e.g., Gidusko, 2018; Urbanova et al., 2017). Because it offers unique opportunities to capture and manipulate 3D scenes and smaller-scale evidence before the context is destroyed through evidence processing, photogrammetry provides a potentially invaluable methodology that should be integrated into the methodology of forensic archaeology. Specifically, photogrammetry provides a much faster and cost-effective method for the 3D documentation of evidence at a crime scene, while using technology that is already commonly used in this field (i.e., digital cameras).

The purpose of this research is to determine how terrestrial close-range photogrammetry (CRP) can be used to improve the documentation process of outdoor crime scenes involving human remains. For this research, a composite skeleton of real human remains, as well as a few

articles of clothing (a hat, a shirt, a pair of shorts, and a pair of shoes), will be used to construct multiple mock forensic crime scenes. Chapter 2 will focus on CRP processing procedures, guidelines for how CRP methodology can be integrated into the traditional forensic archaeology documentation methods, as well as the number of photographs needed to document small-scale scenes with scattered human remains. Chapter 3 will discuss the application of CRP for the documentation of different complex ground surfaces (a surface dominated by grass, a surface dominated by pine needles, and a surface dominated by leaves), as well as data collection techniques, confounding variables for photogrammetry documentation, and best practices for reducing visual errors present in the final models. Finally, Chapter 4 will present a short discussion and conclusion of the information herein.

CHAPTER TWO: PROCESSING PROCEDURES AND INFLUENCE OF NUMBERS OF PHOTOGRAPHS ON QUALITATIVE VISUAL ERRORS

Introduction

Forensic archaeology has been growing and evolving as a field since its inception in the 1980s (Dirkmaat and Cabo, 2016). It first began as a field concerned with the excavation of clandestine burials. However, it soon became evident that archaeological methods and techniques could be applied to document many more aspects of outdoor forensic investigations (Dirkmaat and Cabo, 2016). Today, there are five responsibilities associated with forensic archaeologists. These are 1) locating areas of interest or eliminating them from consideration, 2) interpreting the contextual information at the scene, 3) documenting the scene through mapping, 4) excavating human remains where applicable, and 5) collecting the human remains and associated evidence according to the chain of custody requirements (Dupras et al., 2012: 5). The techniques have been modified slightly from their original archaeological use to accommodate legal and law enforcement standards, significant time constraints, media coverage, and in some cases, instances where the human remains have not been fully decomposed (Dupras et al., 2012).

The traditional methods used to document the context and map outdoor forensic scenes have remained mostly unchanged since they were first implemented in the 1980s, apart from the inclusion of new technology. In most forensic cases, hand-drawn maps are the predominant documentation method to record location and context (Dirkmaat and Cabo, 2016; Dupras et al., 2012). The hand-drawn maps give detailed location information on scaled maps that can often more accurately indicate the location of objects to each other than a single photograph of the scene (Dupras et al., 2012). However, the map drawing is still only a two-dimensional representation of the complex 3-dimensional (3D) information present at a crime scene, even if

the depth is measured using a datum. Reducing 3D context into 2D representations will always result in a reduction of the information present at the scene. This same criticism also applies to another traditional documentation process: photography, where three-dimensional real-world objects are reduced to two-dimensional photos (Errickson et al., 2014; Milliet et al., 2014). This reductive (3D to 2D) process can involve the loss of important information due to technology such as camera acquisition process, lens distortion, depth focus, and zoom features (Douglass et al., 2015; Errickson et al., 2014; Milliet et al., 2014). The photography can also be distorted based on the photographer, especially by the lighting and effects used, how the subject is framed, and the point of view chosen (Douglass et al., 2015; Errickson et al., 2014; Milliet et al., 2014). Thus, photography produces a limited record of the real-world based on a subjective photographer, which causes the photograph to be only a representation of a subjective reality, not a completely accurate representation (Milliet et al., 2014).

In recent years, with significant advancements in technology, researchers in the field of archaeology have begun using 3D-modelling techniques to represent real-world objects and events digitally. This kind of documentation began with technology such as global positioning system (GPS) data and total station systems, which determine 3D coordinates and create digital maps based on the position of these data points. However, beginning in the early 2000s, there was an increased number of researchers interested in using more sophisticated methods of 3D documentation, including laser scanning and photogrammetric methods. These technologies have most recently been applied to the documentation of forensic crime scenes because they offer unique opportunities to capture and manipulate 3D scenes and smaller-scale evidence before it is destroyed with other documentation methods or through the handling of evidence. Specifically,

close-range terrestrial photogrammetry provides a much faster and more cost-effective method for the documentation of evidence at a crime scene (Gidusko, 2018).

The purpose of this chapter is to illustrate the complex process of completing 3D models using the Agisoft Metashape Professional software and to evaluate the number of photographs needed to create visually accurate 3D models of outdoor forensic crime scenes using the digital close-range photogrammetry (CRP) method commonly used in archaeological site documentation. This purpose will be completed by creating one mock forensic crime scene to simulate a situation involving a limited scatter of skeletal remains. The scene was photographed three times using a different number of photographs and the same number of look angles. The resulting images were processed in Agisoft Metashape Professional to create 3D models of the crime scene. The resulting 3D models will be evaluated for qualitative visual error to discuss how many photographs are necessary to create a visually accurate and detailed 3D model. The data collection process and data processing procedures will be described in detail.

Background

Photogrammetry is a commonly used method of context documentation in archaeology. In the age of digital archaeology, this consists of taking systematic photographs around an object or scene and uploading the photographs into a computer program that uses projective geometry to estimate the position of the photographs around the object and takes measurements of the overlapping points between multiple photographs. The following section will provide a brief overview of the uses of photogrammetry in recent years.

Within the last five years, the use of close-range photogrammetry (CRP) in archaeology has increased as the cost of equipment has decreased, making photogrammetry software more

accessible (Forte, 2014). Photogrammetry has been used extensively for the mapping of sites through aerial photogrammetry (Chiabrando et al., 2018; Howland et al., 2018; Landeschi et al., 2016; Pierdicca, 2018; Thomas, 2017). Occasionally, this aerial documentation is used to track changes over time at specific archaeological sites (Andreou et al., 2017; Landeschi et al., 2016). There has also been an increase in the use of photogrammetry as an integrated tool for archaeological documentation (Al-Ruzouq and Dabous, 2017; Douglass et al., 2015; Forte, 2014). Photogrammetry has been frequently used to document features within the site after excavation has taken place (Drap et al., 2017; Garstki et al., 2018; Haukaas and Hodgetts, 2016; Lynch et al., 2017; Peng et al., 2017). It is also used to document artifacts found on the surface of features such as in the case of rock art (Jalandoni et al., 2018) or cave paintings (Majid et al., 2005). Photogrammetry software is also commonly used in conjunction with other geographic information systems (GIS) to further visualize the 3D models that are created (Al-Ruzouq and Dabous, 2017; Drap et al., 2017). In these situations, other GIS systems can be used to orient the geographic location of scenes within the world or used for situations such as accident reconstruction and animation of 3D models. There has even been a surge of research in the subject of underwater photogrammetry (Balletti et al., 2015; Drap et al., 2015; Fulton et al., 2016; Yamafune et al., 2017). Underwater photogrammetry uses the methodology and technology used for terrestrial photogrammetry and applies it to cases that are underwater such as shipwrecks and plane crashes.

As opposed to this diverse use of photogrammetry in archaeology, publications using photogrammetry in forensic science are mostly limited to a few well-established fields. Least applicable to this research, photogrammetry has long been used for the process of identification of perpetrators and victims based on photogrammetric measurement of facial and other body

features (e.g., Aldridge et al., 2005; Cavagnini et al., 2009; Galantucci et al., 2010).

Photogrammetry is also used extensively for the documentation of patterned bodily injuries, both on the soft tissue and the skeletal tissue (e.g., Bruschiweiler et al., 2003; Kottner et al., 2017; Slot et al., 2014; Thali et al., 2000, 2003). Finally, the third most common type of photogrammetric documentation is accident reconstruction which most often comes in the form of traffic accident reconstruction (e.g., Aziz et al., 2010; Bruschiweiler et al., 2003; Fraser et al., 2005; Fraser et al., 2008; Zhan and Zhang, 2006).

In most recent years, there has been a slight increase in the use of photogrammetry outside these fields. For example, the use of aerial photogrammetry in documenting forensic engineering surveys. Smaller-scale evidence at forensic crime scenes such as footwear impressions and blood spatter patterns have been documented using photogrammetry (Andalo et al., 2011; Faulkner, 2017; Holowko et al., 2016). There has also been an increase in the documentation of entire indoor crime scenes with photogrammetry (e.g., Agosto et al., 2008; Constantino et al., 2016; Sansoni et al., 2011; Zancajo-Blazques et al., 2015). However, for this research, the most relevant publications are those on documenting outdoor crime scenes and specifically those involving human remains using CRP documentation methods (Gidusko, 2018; Ruotsala, 2016; Sansoni et al., 2011; Urbanova et al., 2017).

Sansoni and colleagues (2011) use a photogrammetric optic digitizer, which consists of two cameras mounted to a central unit that collects overlapping images (stereoscopic images) and automatically creates a 3D point cloud based on these overlapping images. The methodology is not the same as the methods used for single-camera CRP. However, the authors were successful in proving that stereoscopic 3D digitization of real human remains is possible and

highly valuable. This is especially true in cases where remains may be fragmented, and all the remains and pieces must be documented in situ to preserve the original contextual information (Sansoni et al., 2011).

Also using a burial situation, but single-camera CRP methods, Ruotsala (2016) presents a methodology for the 3D photogrammetric documentation of the forensic excavation of a mass grave. This research consisted of multiple 3D models from different excavation layers with photographs taken after the layer had been uncovered. The results of this research demonstrate that while there are some issues of trying to integrate photogrammetry data collection into a pre-established research methodology, the 3D photogrammetric documentation of mass graves provides much more robust data than the documentation using total stations or other mapping methods that are more commonly used. This more robust data is because while a total station or mapped drawing show only those points preselected by the researcher, photogrammetry offers the ability to map the excavation process with an infinite number of points without taking up a significant amount of time in the field (Ruotsala, 2016).

Urbanova and colleagues (2017), in their second experimental scenario, presented research on photogrammetric documentation using an unmanned aerial vehicle (UAV) of a collection of isolated human bones at the bottom of a large quarry slope. They found that documenting the scene in such a large-scale resulted in 3D models not able to pinpoint the exact location of the human bones. They were unable to be found because they blended in with both the textured and mesh models created. However, when using close-range aerial photogrammetry, they were able to create a detailed, textured model where the individual bones could be seen distinctly from the rocky ground surface they were on. Nevertheless, these bones were again

difficult to distinguish when the texture was disabled, and the mesh layer was examined. It was interesting to note that the number of long-range aerial images used in the 3D model was only 161 out of 700 total photographs, and the number of close-range images used was only 18 (Urbanova et al., 2017). It is unclear if this relatively small number of images, especially in the close-range aerial documentation of the scene, contributed to the lack of distinction between the ground surface and the geometry of the bones. In the case of isolated bones, it may also be essential to incorporate much closer terrestrial photographs from around the scene, especially in cases of complex geometry (which will be discussed further in the next chapter). While this research documented semi-scattered real human remains in an outdoor scene context, the use of aerial photogrammetry diminishes the comparability to the current research presented here.

More recently, Gidusko (2018) researched the documentation of outdoor forensic crime scenes, including scenarios with buried, slightly scattered, and large scatters of human remains. This research did succeed in providing preliminary guidelines for the documentation of outdoor scatter scenes used for the research presented in this thesis. However, Gidusko (2018) used faux human skeletal remains in all scenarios and suggested in the conclusion section that many of the issues present in the model may have been the result of the highly reflective smooth, flat surface of the plastic remains that does not represent the reflectivity or surface of real human bone. This comparison was made by Gidusko (2018), who created a small 3D model showing a side-by-side comparison of faux and real skeletal material. There were a few other issues that make this research non-applicable to forensic settings. The first is that all the scenarios covered were in open areas with no visual obstructions from objects around the scene, a perfect scenario that is rarely ever seen in forensic science. This lack of obstacles made it possible for tripods to be used to document the scene, creating more standardized look angles, and also caused a lack of

shadows over the scene, obstructing the view. Second, for this research, the number of photographs taken of each scenario was limited, with 146 photographs taken for the largest scatter scenario. These models also used a limited number of look angles around the scene. While this limited number of photographs created detailed 3D models that were deemed accurate, there are many instances of qualitative visual errors on the skeletal remains that may be improved with more photographs. Despite some of the visual issues seen in the models, Gidusko (2018) concluded that CRP could be an accurate and useful tool to document the context of these forensic scenes.

Materials and Methods

Location and Scene Construction

The site used for this research was part of the University of Central Florida (UCF) natural lands in an area that was relatively open with tree cover overhead and a ground surface dominated by leaves (Figure 1). The vegetation at the site is a typical oak hammock and pine flatwood that is common in Central Florida (Volk et al., 2017). As these are some of the most common ecosystems in central Florida, this scene is more representative of a forensic crime scene.

The skeletal material was compiled based on relative size, morphology, and coloring from the Department of Anthropology osteological collection at the University of Central Florida. A composite skeleton consisting of a cranium, a mandible, both the atlas and the axis, three unserriated cervical vertebrae, a sternum (both manubrium and sternal body), both left and right scapulae, humeri, radii, and ulnae, six unserriated left ribs, six unserriated right ribs, two unserriated lower thoracic vertebrae, three unserriated lumbar vertebrae, the sacrum, both left, and right os coxae, femora, tibiae, and fibulae, and the right patella and calcaneus were arranged to create the scene. Clothing including a hat, shirt, pair of shorts, and pair of sneakers, was laid out at the scene and placed as if it were interacting with the skeletal material (e.g., the right scapula was placed inside the right sleeve of the shirt) to better simulate the conditions of a forensic crime scene. Because this research focused on determining the number of photographs required to create a 3D model, only one scene was constructed, and the skeletal inventory remained the same for all the 3D models.

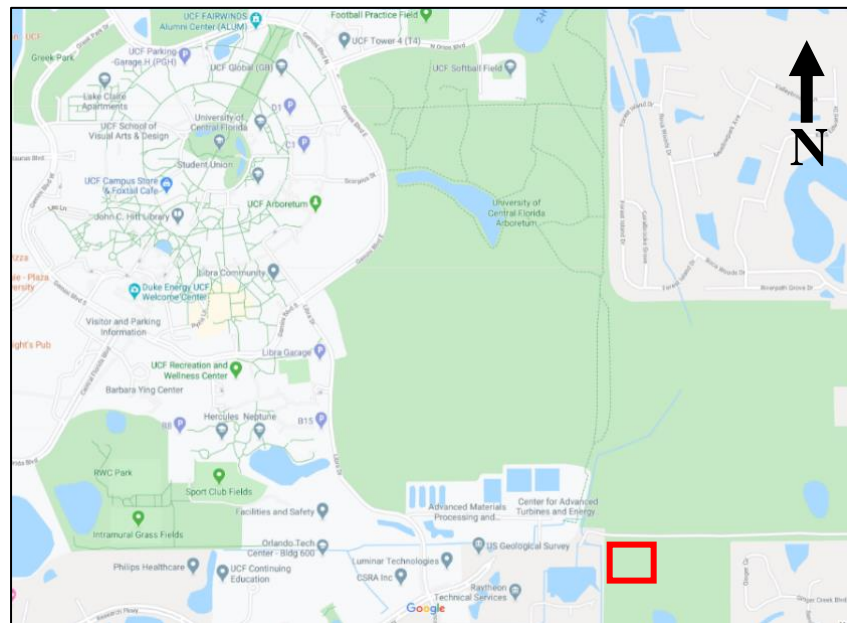


Figure 1. Location of the mock forensic scenario on the UCF natural lands (red box).

Scene Preprocessing and Image Collection

After setting up the scene, the scene limits were determined, and calibrated photogrammetric scale bars purchased from Cultural Heritage Imaging LLC were placed around the boundaries of the scene. These scale bars are professionally calibrated to be accurate within one-tenth of a millimeter and have been specially designed for photogrammetry with integrated coded targets on them (CHI, 2020). Next, any vegetation around the remains was cleared to allow the remains to be photographed from all angles. The vegetation was also removed around the perimeter of the scene, leaving a buffer area to ensure the scales could be seen clearly and to allow for easy movement around the scene. For this research, the same scene, image collection techniques, and camera settings were used to create all three models. For data collection, a Nikon D7200 camera was used to take the photographs. The camera was set to fully automatic settings to see how well the automatic camera settings would capture images to use in the Agisoft Metashape Professional software. The camera focus was also set to autofocus. Following guidelines present in the Agisoft Metashape Professional (Agisoft, 2019) user manual, the images were taken in RAW format and preprocessed into TIFF files to avoid unwanted compression of the image. Data collection utilized the handheld technique described below.

In this case, six semi-standardized look angles were used (Figures 2, 3). Look Angle 1 was taken with the camera held close to the ground and the researcher on their knees to collect an oblique angle from around the scene (Figure 2B). For Look Angle 2, the camera was held slightly higher, so the researcher was on their knees, and the camera was held at about the stomach-level. Look Angle 3 was taken with the researcher slightly raised on their knees, and the camera held at about chest-level (Figure 2C). Look Angle 4 was taken by the researcher standing

upright, and the camera held at about chest-level (Figure 2D). For Look Angle 5, the researcher was standing upright with the camera held at about eye-level. Finally, Look Angle 6 consisted of photographs taken from directly over the scene with an overhead extension pole held over the researcher's head and parallel to the ground surface (Figure 2E). These look angle levels were taken from around the scene to ensure maximum overlap between photographs. An extra level of Close-Up Photographs was taken from a close-up view of all areas of interest to ensure that every area of the scene was captured (Figure 2A). These close-up images were taken to capture every detail of the scene and to try and improve the ground surface-subject interfacing errors that have been seen in prior research. These close-up images were taken from inside the perimeter of the scene and were used to ensure that every aspect of the bones were recorded in situ.



Figure 2. Examples of the look angles. A) Close-Up Photographs, B) Look Angle 1, C) Look Angle 3, D) Look Angle 4, E) Look Angle 6.

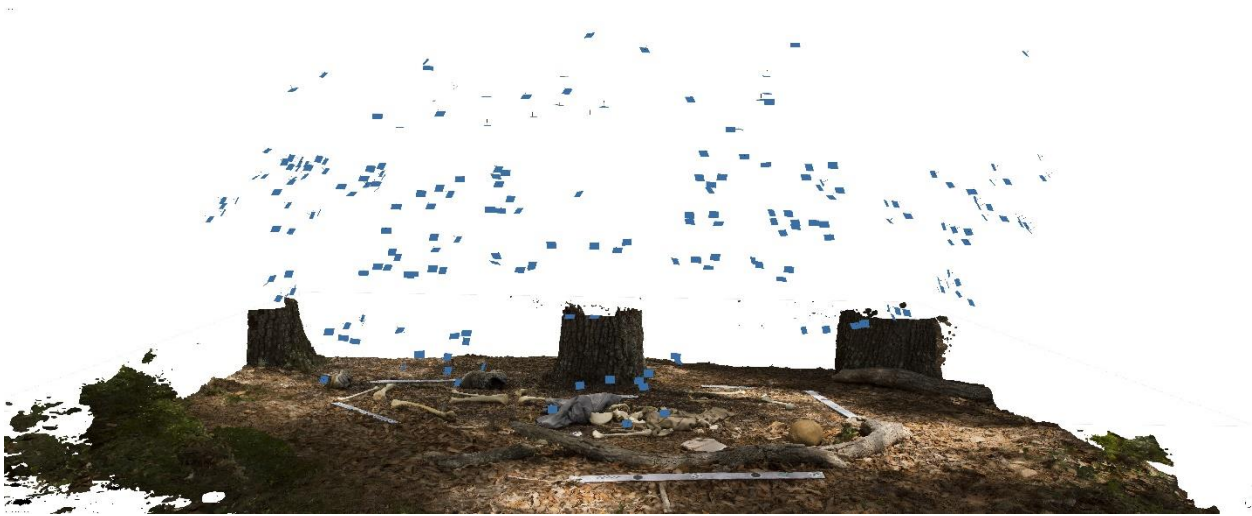


Figure 3. Screenshot of the final Model 1 showing the location where all the photographs were taken from (Blue squares).

While each iteration of the scene incorporated the same number of look angles, the only thing that changed was the number of photographs taken for each model. For Model 1, 281 photographs were taken in total; however, only 223 were used for the final model (see the results section for more details). For Model 2, 279 photographs were taken, and 250 were used to create the final model. Finally, for Model 3, 387 photographs were taken, and 358 photographs were used for the final model.

Preprocessing of the photographs was necessary in order to create a final 3D model. All images used were captured in .raw format in order to maximize the amount of data contained in each image. .raw file formats automatically capture all image data that is recorded by the camera sensors when the photograph is taken. This step also allows the avoidance of unwanted distortion that can happen when images are compressed into .jpg formats. However, because the Agisoft Metashape Professional software cannot process .raw photographs, the photographs taken had to be converted from their original .raw format into .tiff files. This conversion was completed using

Adobe Bridge software. While completing this conversion from .raw to .tiff, the photographs were also white balanced based on the white from one of the scale bars to make sure the color is an accurate representation of the real-world scenario. The resulting white-balanced .tiff photographs were then uploaded into Agisoft Metashape Professional to be processed into a 3D model.

Processing in Agisoft Metashape Professional

The Agisoft Metashape Professional software was chosen for this research for multiple reasons. Many researchers have already set a precedent in both archaeological research and forensic archaeological research. Another reason for choosing this software is that it is known for creating accurate 3D models while presenting a semi-automated approach through the structure-from-motion (SfM) software without making the entire process a black-box operation (Green et al., 2014). In other words, Agisoft Metashape Professional creates a complete and fully textured 3D model without the researcher having to use multiple software programs (like Bundler, VisualSfM, CloudCompare, and Meshlab) to create different levels of the model. Agisoft Metashape Professional also allows the operator to choose the processing parameters that are used (unlike software such as 123D Catch, which produces a completed 3D model automatically with uploaded photographs; Green et al., 2014).

Processing in Agisoft Metashape Professional follows a very generalized and linear workflow (Agisoft, 2019; Figure 4). First, photographs are uploaded into the software (Figures 5,6,7). The estimation of image quality algorithm is then used to streamline the process and remove blurry images before they are included in the sparse point cloud step (Figures 8,9,10). For this research, a marker registration algorithm was also run in order to make sure the markers

are detected before the images are aligned (Figure 11). This extra step just streamlines the process for the best results but is not necessary for the sparse point cloud to generation. Next, the sparse point cloud (SPC) was created with the quality set to generate on high, the key point limit set to 60,000 (key point: the number of points in images that are going to be used to find tie points) and the tie point limit set to 0 (tie point: key points that an image has in common with at least one other image; 0 means no limit) (Figures 12,13,14). The photographs that were not aligned during this process were removed from the Agisoft Metashape Professional software. Optimization of the sparse point cloud was conducted following the guidelines set out in the Agisoft Metashape Professional user manual (2019), the USGS UAV photogrammetry guidelines (2016), and guidelines provided by Mayer and colleagues (2018). This optimization serves the purpose of tightening the precision and accuracy of the tie points in order to best estimate the position of the photographs around the scene (Agisoft, 2019). First, all the scales were added into the model based on the distances between the coded targets present on the calibrated scale bars, and the distances were updated and saved so measurements could now be taken from the model (Agisoft, 2019). Next, a bundle block adjustment was performed to optimize the cameras by accepting all the default internal and external camera calibration parameters in the dialog box (Agisoft, 2019, see Figure 19).

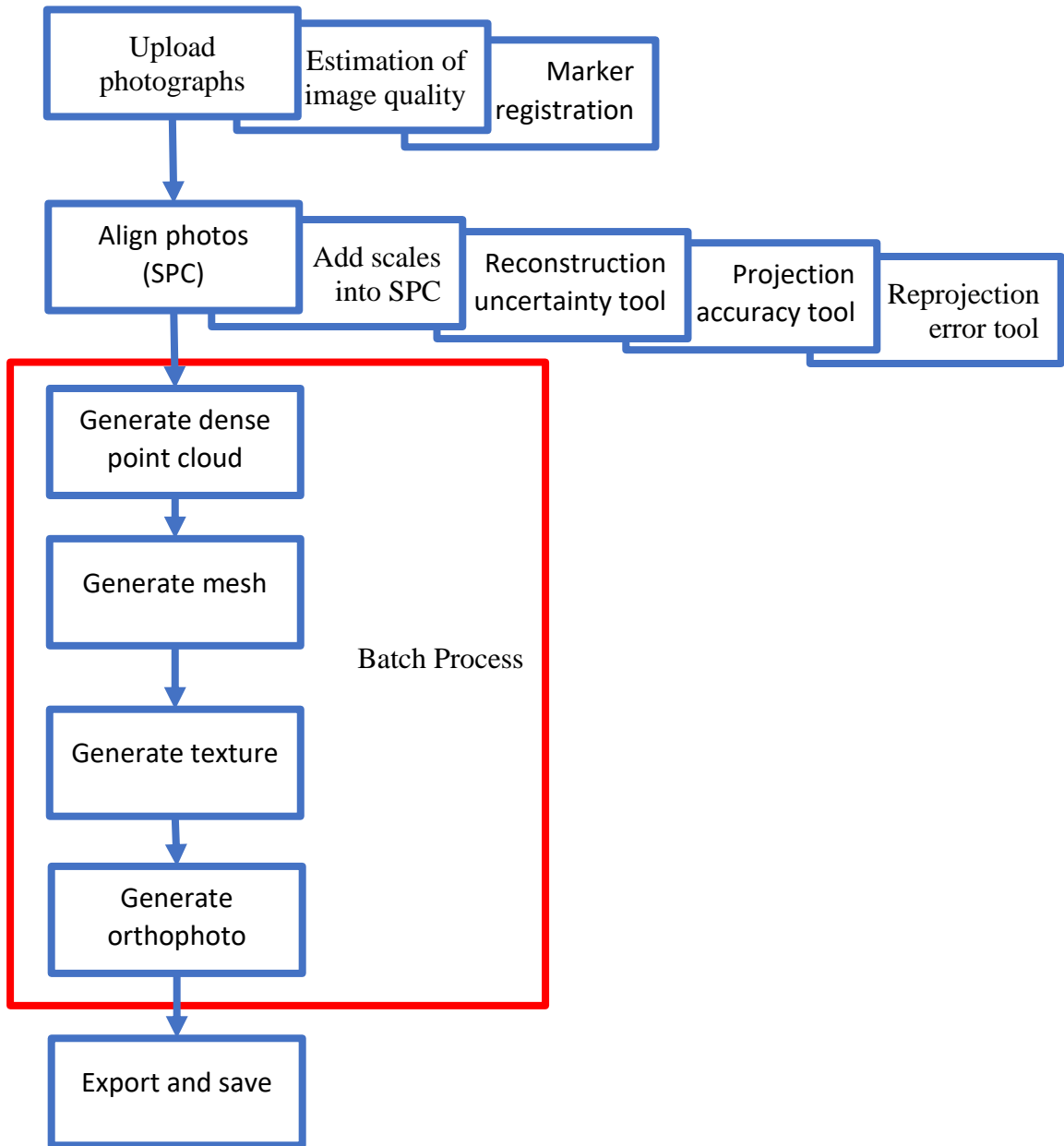


Figure 4. Generalized linear process of creating a 3D model using Agisoft Metashape Professional

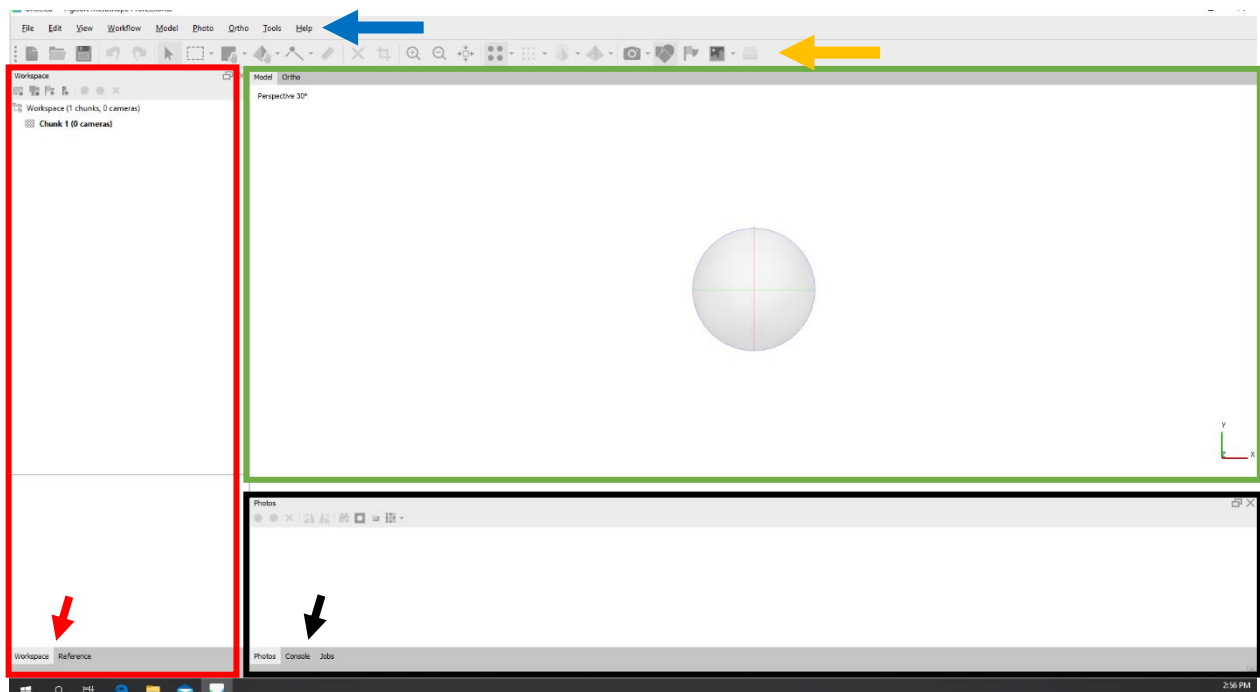


Figure 5. Main windows and functions of the Agisoft Metashape Professional interface. The blue arrow is pointing at the drop-down menus that contain all the tools and processing commands. The yellow arrow is pointing at the navigation and view toolbar that controls actions possible in the large viewing window (green box) in the center of the screen. On the left side of the viewing window is the workspace/reference window (red box). The workspace and the reference windows can be selected between the tabs on the bottom of this window (red arrow). The black box shows the photos/console/jobs window directly below the viewing window. These three windows can be selected by choosing the corresponding tab on the bottom of the window (black arrow).

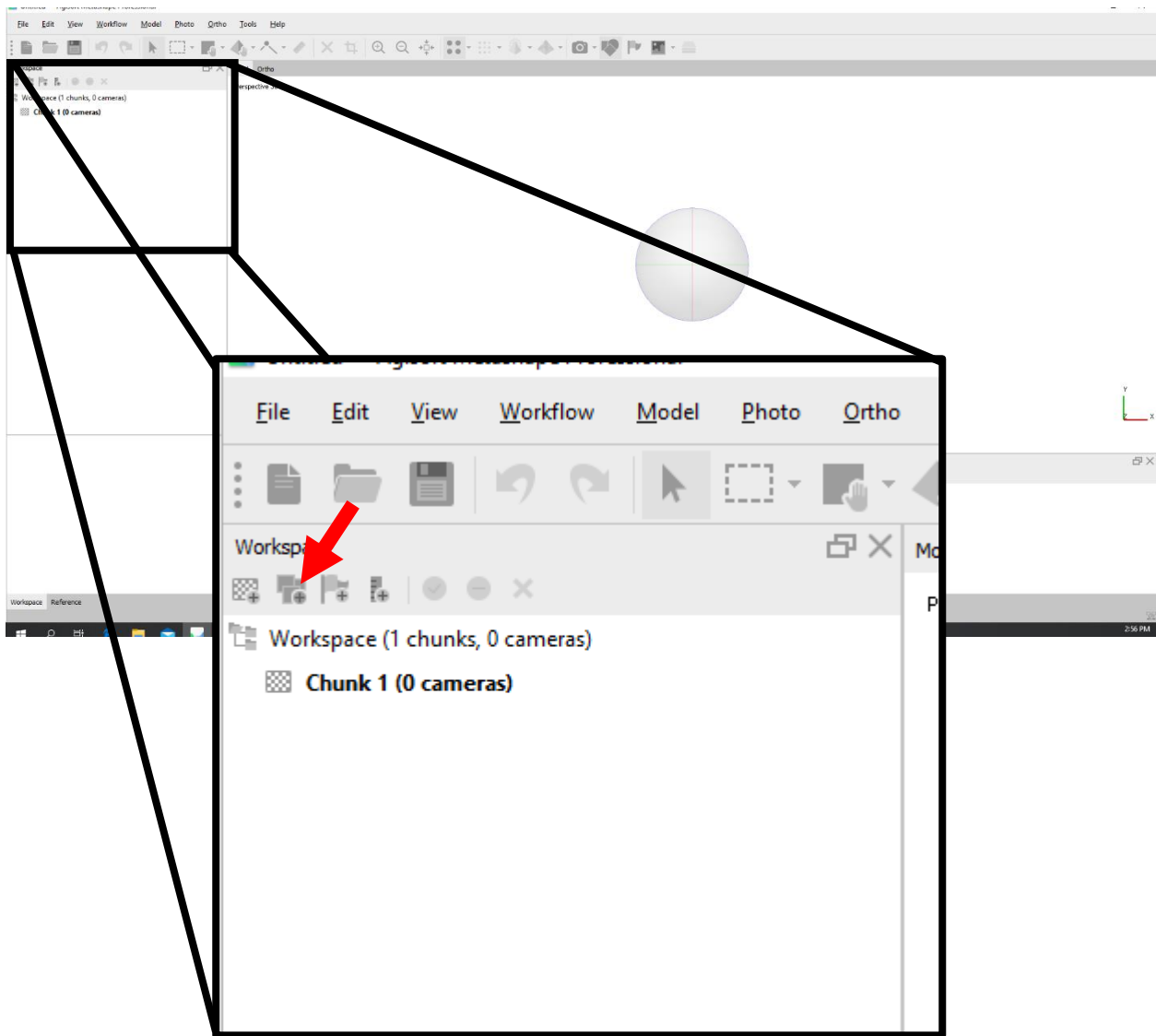


Figure 6. Step 1 to add photographs into the Agisoft Metashape Professional program, click on the add photos button in the workspace window.

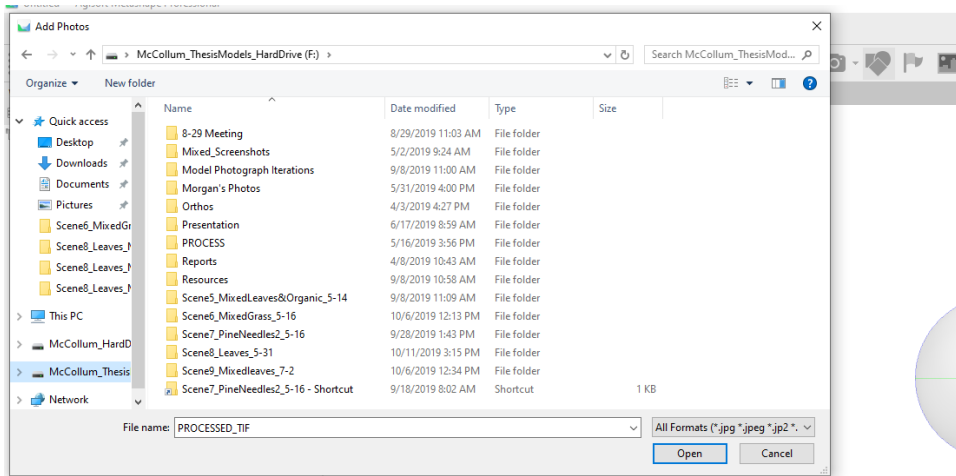


Figure 7. Step 2 to add photos into the Agisoft Metashape Professional software, navigate to the folder where the photos are located, then select all the photographs to create the model, then click the open button

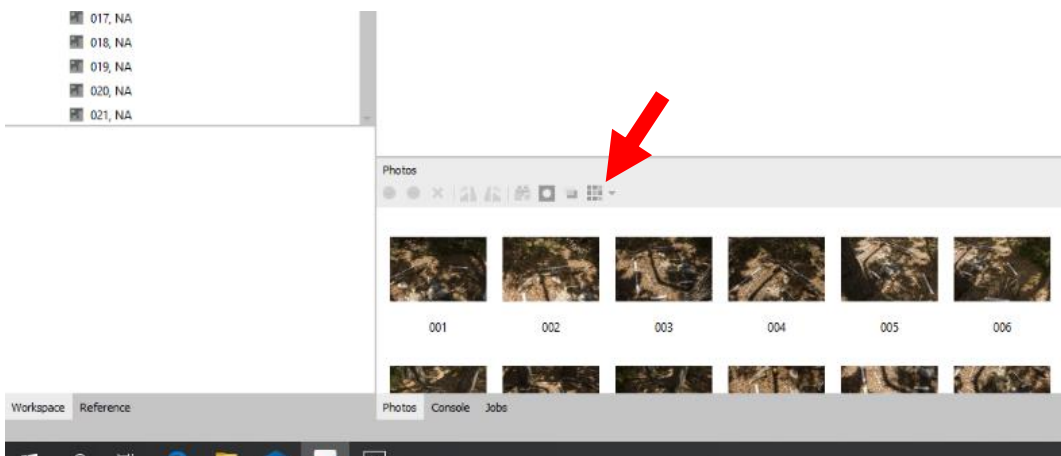


Figure 8. Agisoft Metashape Professional interface with photographs added into the program. To begin the estimation of image quality, click the drop-down view menu for the photos window and click “details” to view the detailed view for the photographs.

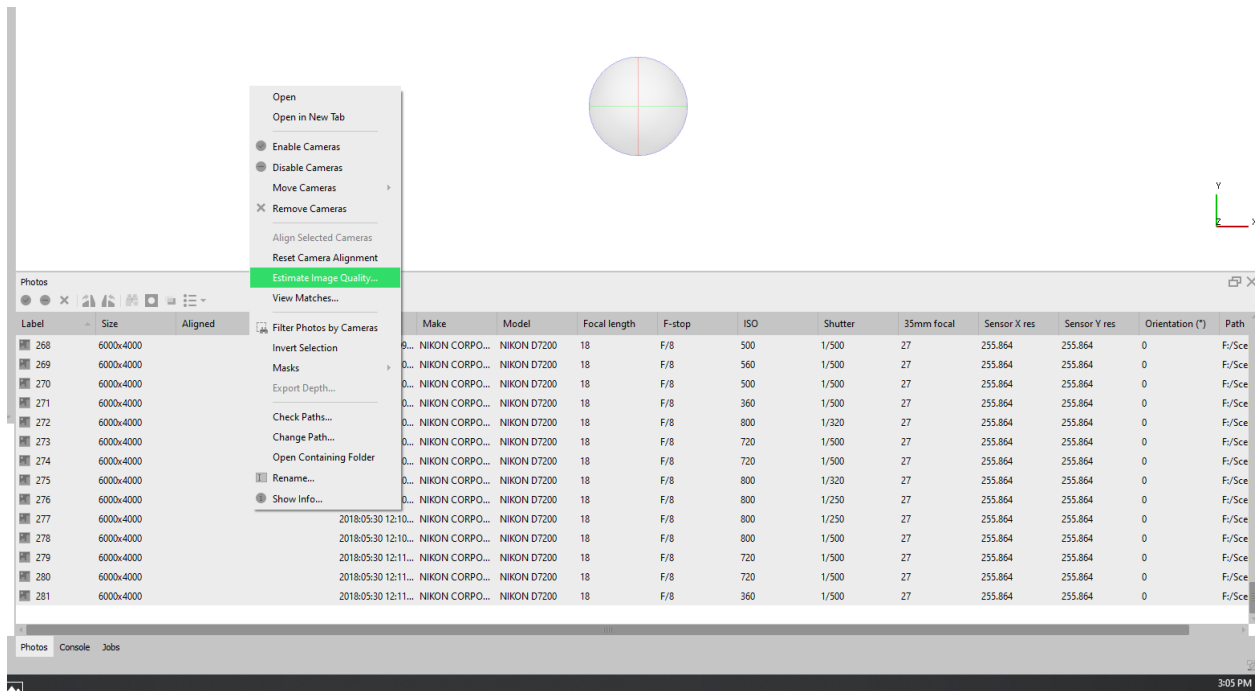


Figure 9. Details view of the photos window in Agisoft Metashape Professional. To run the Estimation of image quality, select all the photographs in this view, right click and select the “estimate image quality” command

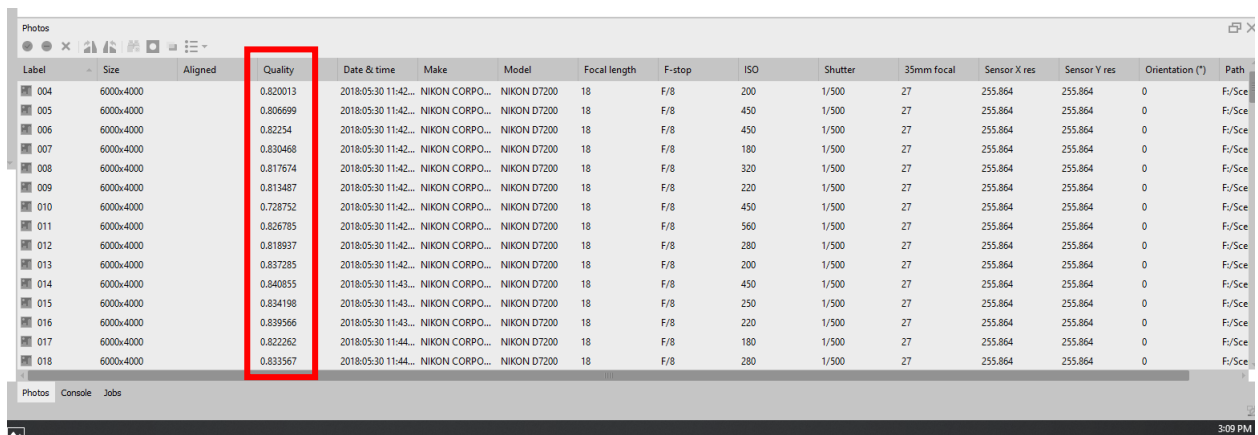


Figure 10. Details view of the photos window in Agisoft Metashape Professional. After running the estimation of image quality, a value will appear under the quality column (red box). It is suggested in the Agisoft Metashape Professional (2019) user manual that all photos with a quality of less than .5 should be removed from the program. This is done by selecting the photographs with a value of less than .5, right clicking and pressing the “remove cameras” command.

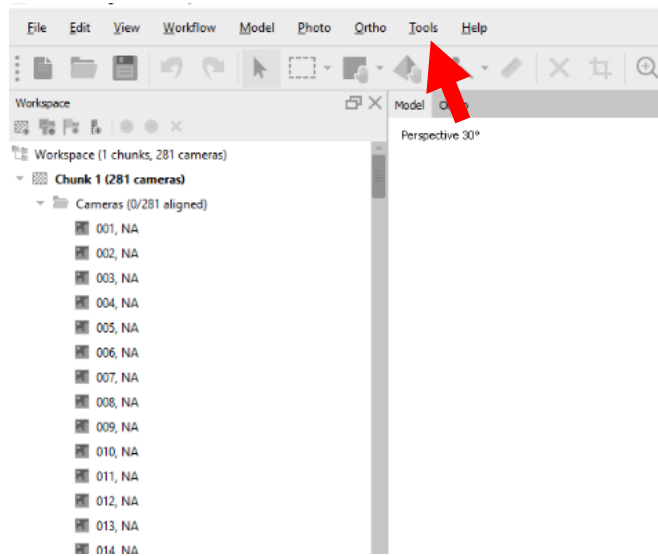


Figure 11. To run the marker registration in Agisoft Metashape Professional, click the "tools" drop-down menu and select "detect markers".

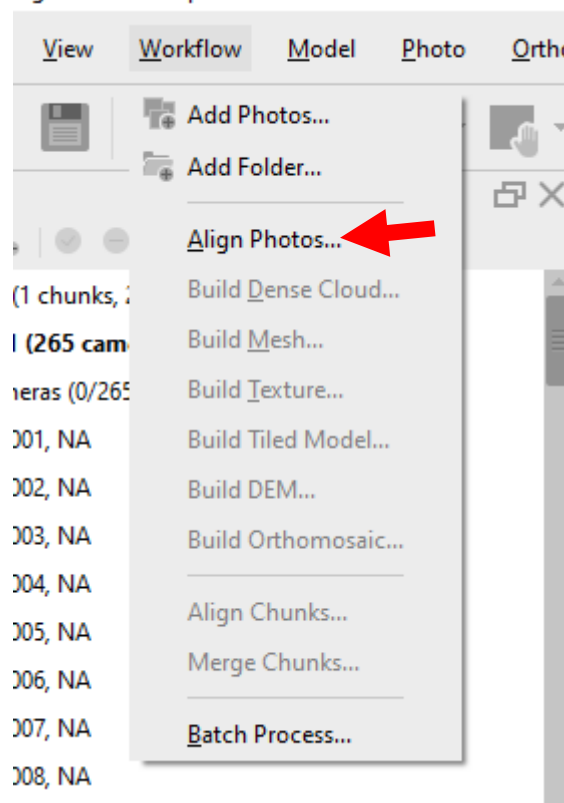


Figure 12. To create the sparse point cloud (SPC), use the drop-down workflow menu and click the "align photos" command.

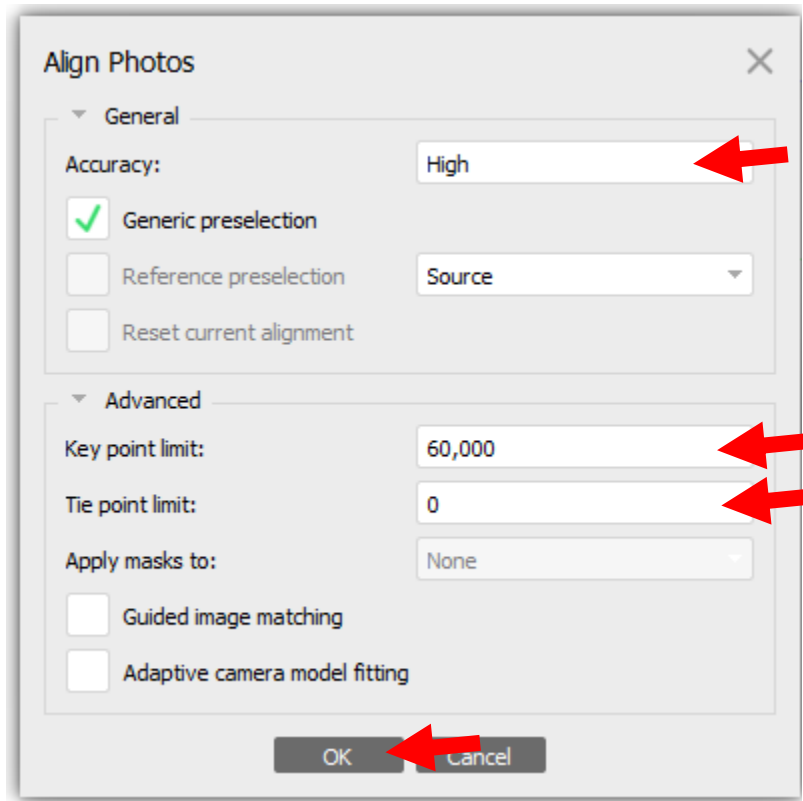


Figure 13. Step 2 to create the SPC, make sure the accuracy is set to high, that the key point limit is set to 60,000, and the tie point limit is set to 0 and then press “ok” to start processing.



Figure 14. The resulting SPC in the viewing window of Agisoft Metashape Professional. In case any mistakes are made in the optimization, duplicate the chunk by right clicking on the chunk title (red arrow) and choose “Duplicate Chunk”.

The chunk with the resulting sparse point cloud was then duplicated so that if any mistakes were made during further optimization processes, the original was saved without having to repeat the first camera alignment step (Figure 14). After this, three optimization tools were used to further optimize the tie points (and by effect, the position of the cameras) by adjusting the levels within the corresponding dialog box (Agisoft, 2019).

The first optimization tool used was the reconstruction uncertainty tool, which allows the deletion of points with a low base-to-height ratio (Mayer et al., 2018; USGS, 2017: Figures 16,17). As a result, the noise of the subsequent point clouds is reduced, and the remaining points have high base-to-height ratios, allowing the camera positions to be more accurately estimated (Agisoft, 2019). The remaining optimization process is dedicated to reducing the error values given for each camera per pixel, as seen in the reference tab of the software (Mayer et al., 2018; USGS, 2016: Figure 18). After this, the bundle block adjustment should be rerun, accepting all default fit parameters in the dialog box (Figure 19). The next tool used to do this is the projection accuracy tool (Figures 16,17). This optimization tool allows for the deletion of tie points that were poorly located based on the size of the point relative to those with strong point determination (Agisoft, 2019). Using this optimization tool, tie points with a statistically weighted error value 'x' times higher than the tie point with the least amount of estimated uncertainty can be deleted (Mayer et al., 2018). As a result, the remaining tie points have the best tie point precision values. As in previous steps, the cameras should be optimized after each step, still selecting the default camera optimization parameters. Finally, the reprojection error will be optimized (Figures 16,17). This value represents the distance between the real and reconstructed position of the cameras and is used to remove points that have large residuals or that were falsely matched between photographs (Agisoft, 2019; Mayer et al., 2018; USGS, 2017). The levels

indicated in this optimization parameter are given in pixel units, and this parameter had the most significant influence on the RMSE given in the final report (Mayer et al., 2018). This process only needs to be run once, and afterward, the accuracy of the tie points should be tightened using all the fit parameters available in the bundle block adjustment, not just the defaults (Mayer et al., 2018; USGS, 2016).

According to the USGS (2016), all the cameras should have more than 100 projections present. It is suggested in this resource that the Agisoft program does not include the cameras with less than 100 projections, however, during this research, it was found that there was less noise introduced into the final model when these cameras with less than 100 projections were removed from the program entirely (Figure 18).

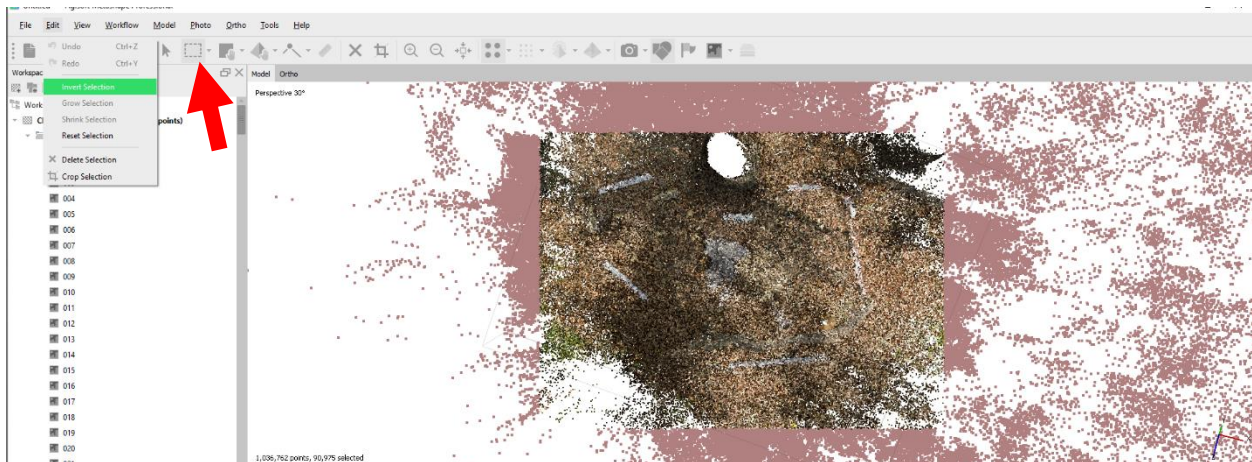


Figure 15. On the duplicated chunk, the first step in the SPC optimization process is to delete the unneeded points around the scene. Using the selection tool (red arrow) to select the scene boundaries and then inverting the selection by using the “Edit” drop-down menu then selecting “Invert selection” command. Next, delete the outlying points.

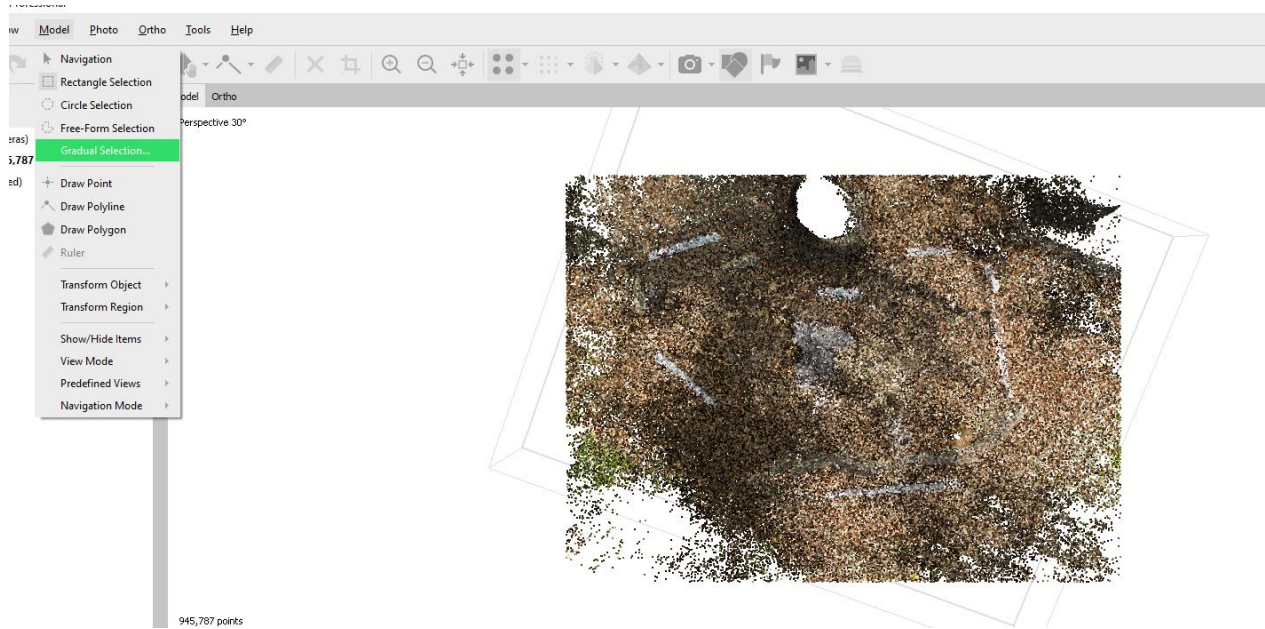


Figure 16. For further optimization, select the "Model" drop-down menu and click the "Gradual Selection" command.

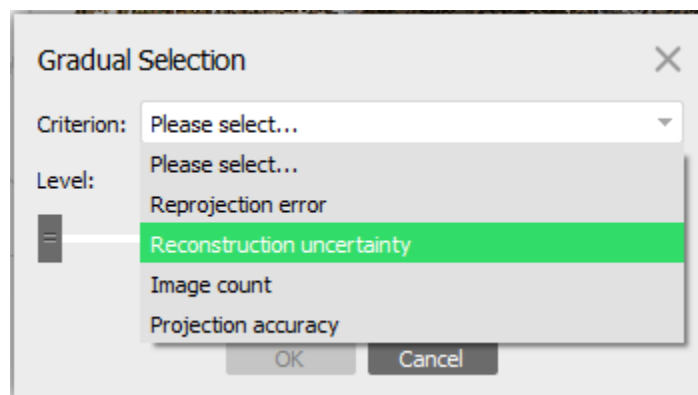


Figure 17. First use the "Reconstruction Uncertainty" command, then the "Projection Accuracy" and finally, the "Reprojection error" optimization commands, repeating the previous step and this one each time.

r (°)	Error (°)	Projections	Error (pix)
		8	2.137
		16	1.294
		261	1.188
		1173	0.995
		24	1.096
		35	0.831
		4997	0.944
		772	0.847
		2184	0.862
		5731	0.844

Figure 18. Reference window of Agisoft Metashape Professional software. During the entire optimization process, the goal is to get the error value (red box) below 1. Photographs that have fewer than 100 projections (blue box) should be removed from the software.

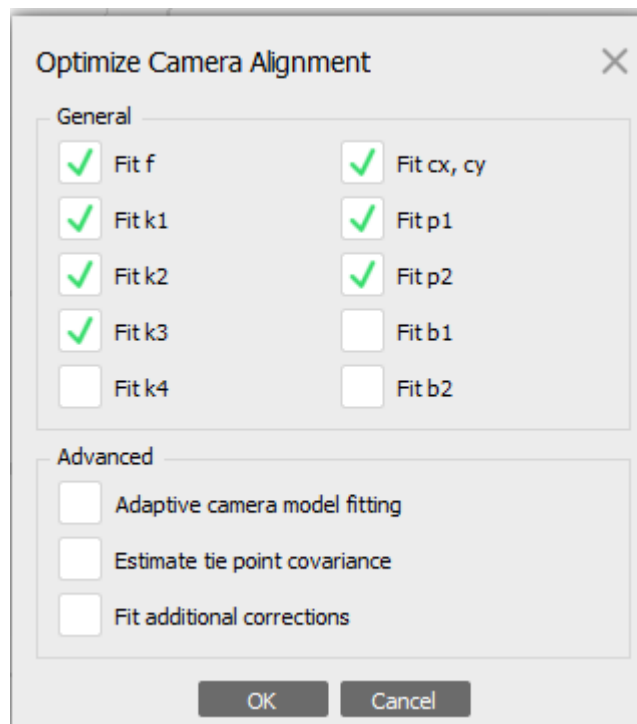


Figure 19. After each optimization step, the cameras should be optimized. In the “Tools” drop-down menu, select the “Optimize camera alignment” command. Accept all the default fits and press “OK” to optimize the camera alignment.

After the SPC was optimized, a batch process was set up to create the rest of the 3D model (Agisoft, 2019: Figures 20,21). First, the dense point cloud (DPC) is set up to generate in a high setting, and all other default generation parameters kept (Figure 22). Next, the mesh is set to generate on high from the DPC with all the default generation parameters kept (Figure 23). After that, the texture is set to generate from the mesh. The texture size is changed to 8192, with all the other default parameters kept (Figure 24). Enlarging the default texture size creates a larger texture with more pixels and, therefore, a higher resolution for the texture layer. Finally, an orthomosaic is set to generate based on all the photos used to create the model in the software (Figure 25). Before the processing starts, the box should be checked to save the last step generated in case the batch process is interrupted for any reason, the last step to be generated will still be saved (Figure 26).

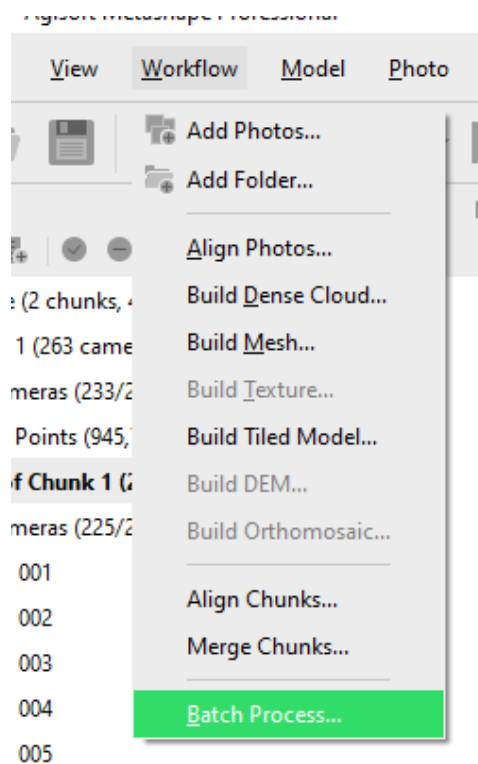


Figure 20. To set up the batch process, click on the "Workflow" drop-down menu and select "Batch process".

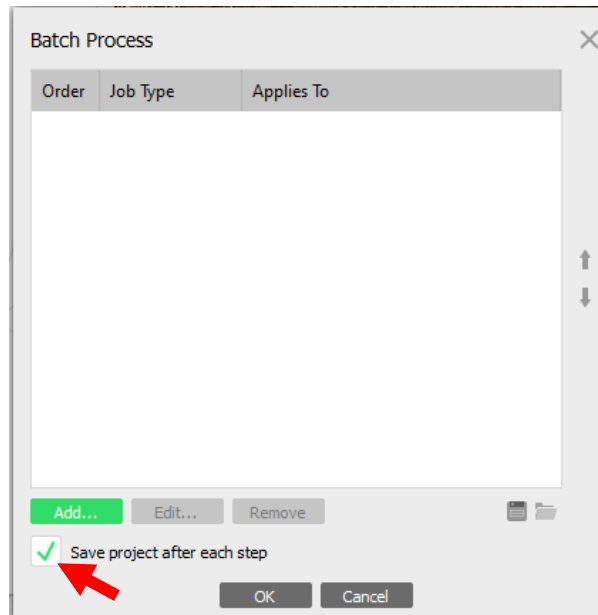


Figure 21. Setting up the batch process to create the 3D model in Agisoft Metashape Professional. Make sure the box is checked to save the project after each step (red arrow). Click on the “Add...” button.

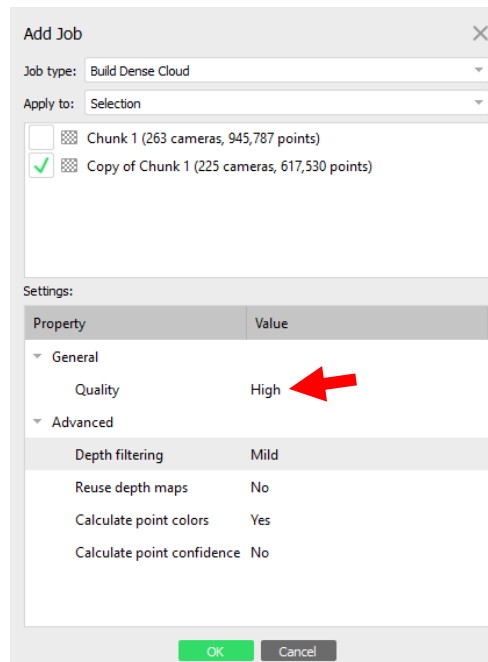


Figure 22. First, the dense point cloud must be generated. On the “Job type” drop-down, choose “Build Dense Cloud”, on the “Apply to” drop-down, choose “Selection” to only choose the optimized SPC that was created. In the next section down, under Quality, make sure the value is set to “High” (red arrow). Click “OK”, accepting all other default values.

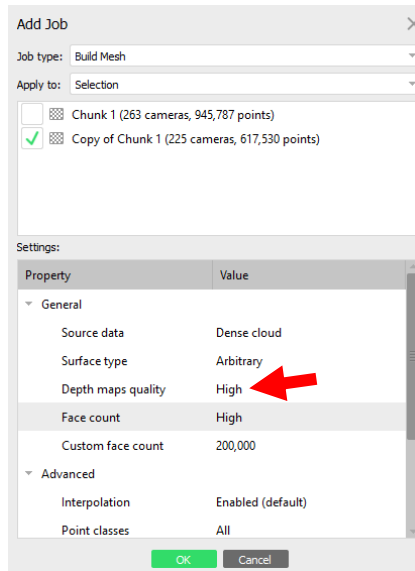


Figure 23. Next, the mesh should be generated. On the “Job type” drop-down menu, choose “Build Mesh”, on the “Apply to” drop-down menu, choose “Selection” then make sure only the optimized chunk is selected. On the “Depth maps quality” property, make sure the value is set to “High” (red arrow). Click “OK” and accept all other default values.

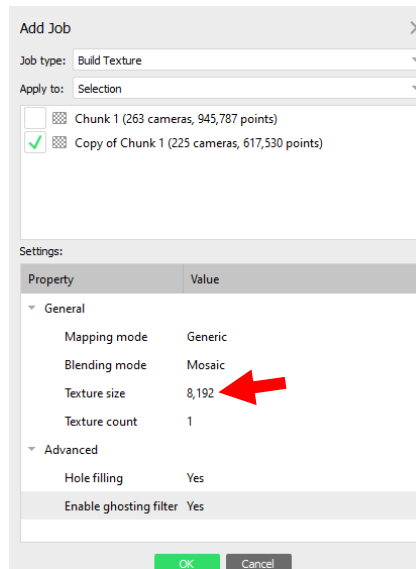


Figure 24. Next, the texture should be generated. On the “Job type” drop-down menu, choose “Build Texture”, on the “Apply to” drop-down menu, choose “Selection” then make sure only the optimized chunk is selected. On the “Texture size” property, change the value to “8192” (red arrow). Click “OK” and accept all other default values.

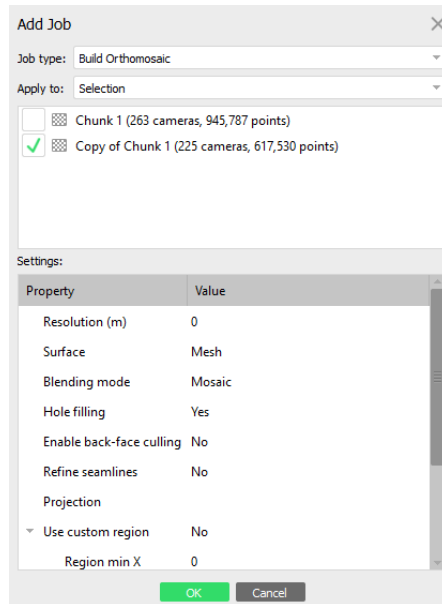


Figure 25. Finally, the orthomosaic should be generated. On the “Job type” drop-down menu, choose “Build Orthomosaic”, on the “Apply to” drop-down menu, choose “Selection” then make sure only the optimized chunk is selected. Click “OK” and accept all default values.

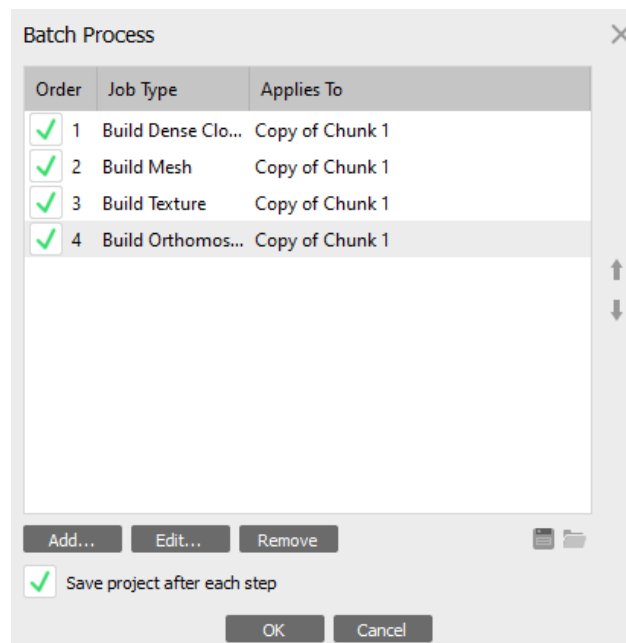


Figure 26. Final screen for the batch process set-up. Make sure the box to “Save project after each step” is checked. Click "OK"

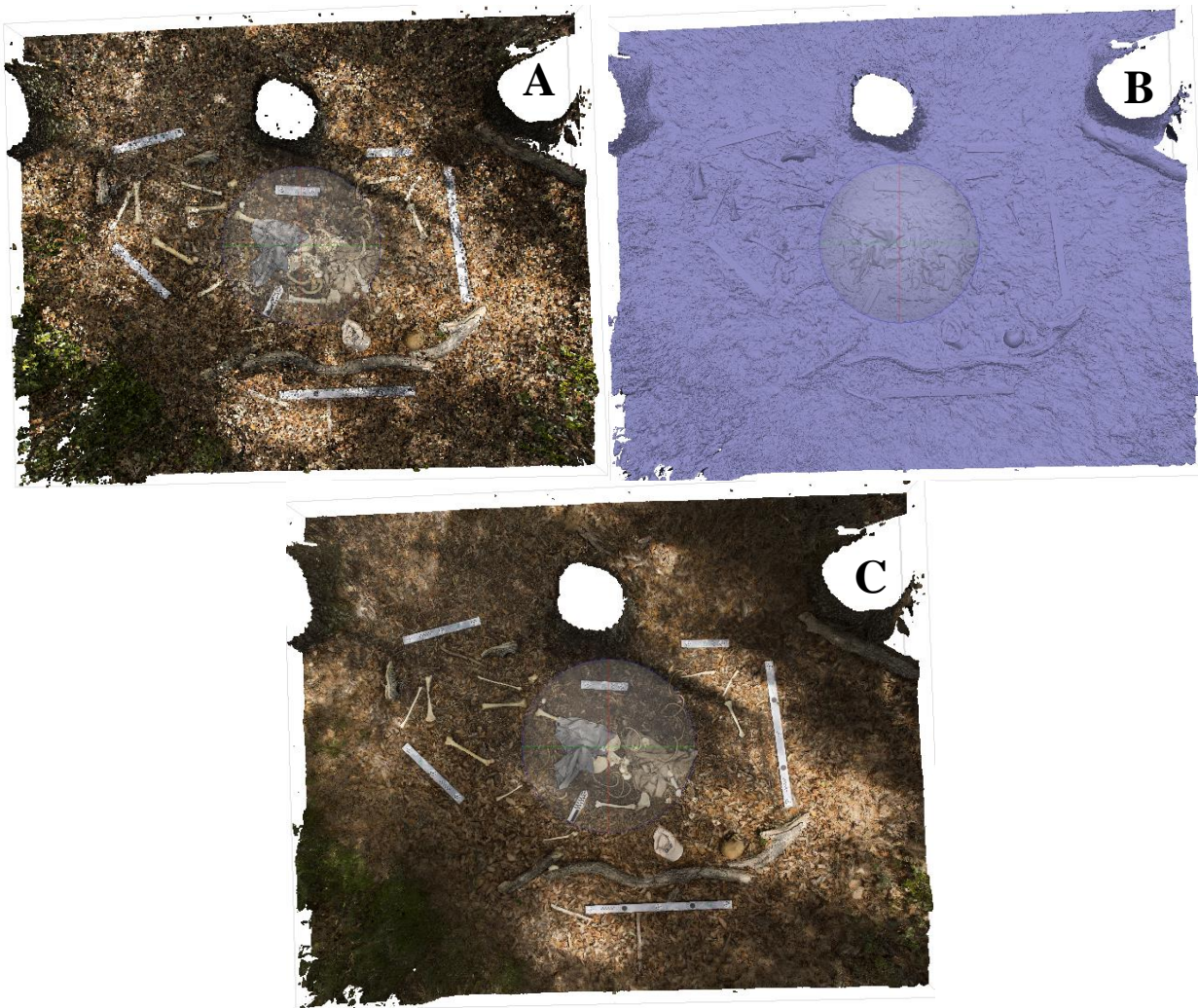


Figure 27. Results of the batch process. A) Dense point cloud, B) Mesh, and C) Textured model.

Determining accuracy and assessing visual error

The assessment of the accuracy of 3D models relies on the comparison between what is seen in the real world and the 3D virtual representation seen in the created model. For this assessment, the root mean square error (RMSE) that is present in the final report will be used as well as the scale bar error also present in the final report. In general, a 3D model is considered accurate if the RMSE is less than one (Mayer et al., 2018). For determining the accuracy of measurements taken in Agisoft Metashape Professional, the scale error present in the final

processing report will be used. If the error is less than 1/10th of a millimeter (the maximum error the photogrammetry scales were calibrated for by CHI [2019]), the scales will be determined to be accurate.

For the visual comparison and assessment of accuracy, there are multiple output options available. For this research, the photographs displayed in the following sections that discuss qualitative visual error will be screenshots of the models taken directly from the Agisoft Metashape Professional. A visual comparison between the geometry of the model and the textured model will be used to discover exactly where the error was introduced into the model.

While conducting this visual analysis, four areas of interest will be discussed. 1) the visual representation of the geometry of skeletal elements compared to the appearance of the real-life bone; 2) the visual representation of the geometry of the clothing in the model; 3) the visual interface between the ground surface and the subject material (whether it be bone, clothing, or scales); and 4) the visual interface between the subject materials (between bone and bone, between bone and clothing, or between clothing and clothing). There is also a terminology distinction that must be discussed. In further sections, misrendered geometry will refer to sections of bones that appear to be missing in the geometry layer of the 3D model causing subsequent problems in the texture. Visual distortion will refer to areas of bones that are present in the geometry but appear different than they do in real life because of the texture layer (e.g., they appear wavy on the outline). These visual errors will be assessed in three standardized sections of the model, including overhead screenshots of the area involving the head, the second overhead involving the torso region, and the third of an overhead involving the lower legs region.

Results

Model 1

Data collection for Model 1 proceeded as described above. In total, 281 photographs were captured for this model taking 30 minutes to complete. Out of the 281 photographs taken, 223 were used to complete the model. In total, it took 35.28 hours for this model to finish processing in Agisoft Metashape Professional (see Table 1 for processing information).

Of the 58 photos that were not incorporated into the final model, six photographs were excluded by the estimation of image quality tool. These excluded photographs included all the photographs that were too blurry to be utilized before the sparse point cloud is even run. Of these photographs, two were removed from the Close-Up Photographs, three were removed from Look Angle 1, and one was removed from a higher look angle. Most of these photographs were taken from areas that were heavily shaded around the scene. Next, 36 photographs were unaligned during the creation of the SPC and were removed from the program. Of these photographs, 25 were taken from the Close-Up Photographs, and 11 were taken from Look Angle 1. During the optimization process, all the cameras that had less than 100 tie point projections (16 images) were also removed from the program. Most of these photographs that were removed were taken from Look Angle 1 and the remaining Close-Up Photographs because these photos tend to lack reference data for tie points to be found (See Table 2 for more details).



Figure 28. Overhead screenshot of Model 1 showing little visual error except on the left tibia (white arrow).

The resulting 3D model had an RMSE score of .528 pix while the total scale error is .000436, indicating that the model has been accurately scaled to represent the real-world scene. Overall, this textured model shows an accurate representation of the relative position of all the elements present (Figure 28). The screenshot shows the location and orientation of identifiable bones, the contours in clothing, the interface between clothing and bones, the interface between bones and other bones, the interface between the subjects and the surface of the ground, and the representation of the scales around the perimeter of the scene. When reviewing the overall overhead view of the 3D model, there appear to be very few areas where the qualitative visual

errors are present. The only area that is immediately apparent is the distal shaft of the left tibia that appears not to have been modeled correctly.

Visual errors only become apparent when zoomed into the model. Figure 29 shows a slightly zoomed-in screenshot of the region involving the cranium, mandible, five cervical vertebrae (including the atlas and axis), sternum (both manubrium and corpus sterni), five right ribs, the right scapula, humerus, radius, and ulna, the hat, and part of the shirt. Even slightly zoomed in, there are a few visual errors present. In the area of the ribs, there are some interfacing issues between the ground surface and the ribs in the geometry, as well as the texture layer. While the texture layer shows the location and shape of the vertebrae and sternal bones, there are issues with the interface between the bones and the ground surface, so in the geometry, they do not appear distinct. In cases like these, the color differences in the textured models can hide underlying issues in the geometry. On the scale bar that is in the upper left corner of the screenshots, there is some visual distortion, possibly caused by the appearance of leaf litter covering part of the scale (Figure 29).

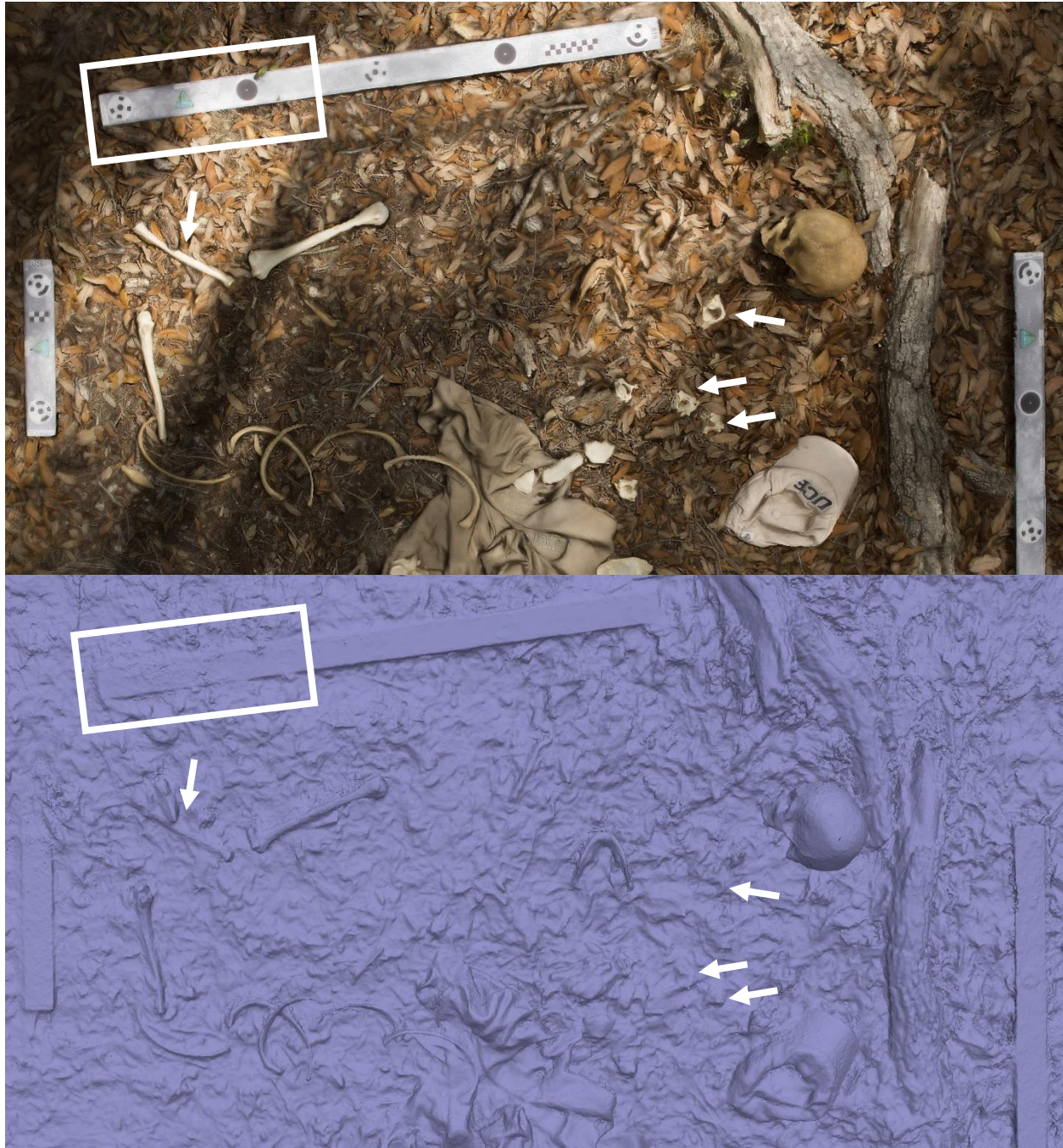


Figure 29. Zoomed in screenshots showing the textured (top) and geometry (bottom) of the head region of Model 1. White arrows indicate areas with poor ground surface-subject interface and the white box indicates an area of scale distortion.

Figure 30 shows a zoomed-in screenshot of the torso region, including the left scapula and humerus, five unserriated lower vertebrae, four unserriated ribs, the os coxae, and the sacrum. The textured screenshot of this region shows slightly more distortion, specifically in areas where two bones are directly adjacent to each other. The areas where this is most prominent is the interface between the lumbar vertebrae in the direct center of the screenshot, the interface between the shirt, the vertebra, and the rib to the left, and on the interface between the head of the humerus and the scapula. These problems appear to stem from the geometry where there is poor subject-subject interface making many of the bones appear to be fused together and fused to the ground.

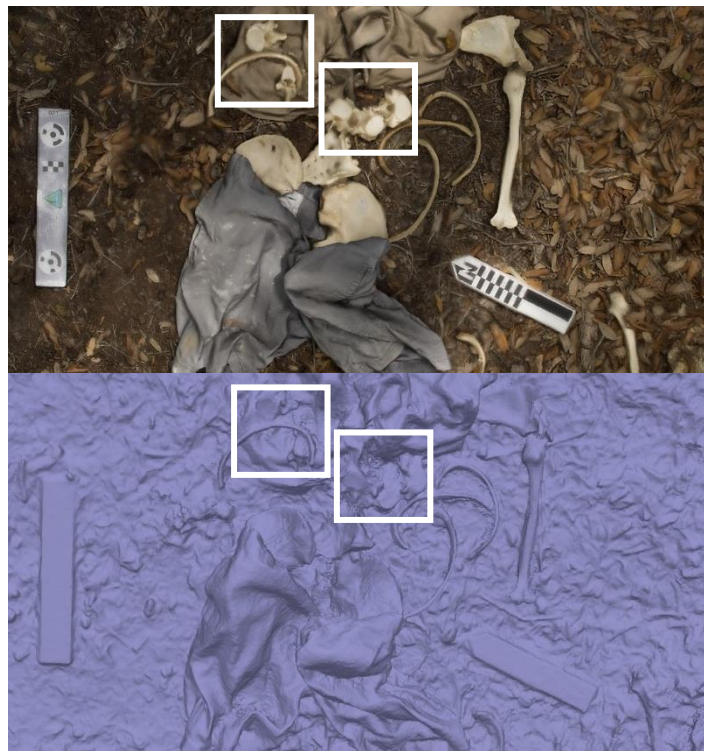


Figure 30. Zoomed in screenshot of the textured (top) and geometry (bottom) area of the torso for Model 1. White boxes indicate the most obvious areas of subject-subject interfacing errors. The one on the left is pointing at the interface between the shirt, vertebrae, and rib. The one on the right indicates the lumbar vertebrae, the shirt and the ground surface. The arrow is pointing to the poor interface between the head of the left humerus and the left scapula.

Figure 31 shows screenshots of the area of the lower legs, including the right and left femur, the right patella, both fibulae and tibiae, the right calcaneus, and the left radius and ulna. The left ulna in the upper right corner shows significant distortion around the edges as well as a missing section in the upper shaft area. This distortion seems to be due to poor ground surface-subject interface in the geometry as well as loose leaf litter that appears to be covering part of this bone. Following a general pattern, many of the thin bones (ribs, fibulae, etc.) appear to have ground surface-subject interfacing errors. The most significant visual distortion in these screenshots is the misrendered geometry of the left tibia. There is misrendered geometry along the distal end of the tibia, beginning in the midshaft of the bone, which makes the bone appear warped and as if there were missing pieces.



Figure 31. Zoomed in screenshot of the texture (left) and geometry (right) of the lower leg portion of Model 1. The arrows show poor ground surface-subject interface in the areas of the left ulna (top right) and the unserialised ribs (left). The white box is showing the misrendered geometry of the left tibia.

Table 1. Processing time in Agisoft Metashape Professional for the creation of a 3D model (in hours)

Model #	Photograph Collection Time	Camera Align Time	Dense Point Cloud Generation	Mesh Generation	Texture Generation	Orthomosaic Generation	Total Time
1	.5	.38	32.9	.6	.65	.25	35.28
2	.35	.62	37.28	.73	.67	.25	39.9
3	.88	.92	99.8	.68	.23	.05	102.56

Model 2

Data collection for Model 2 was conducted following the guidelines set above. In total, 279 images were captured for this model taking 21 minutes to complete. Out of the 279 images that were taken, 250 were used to complete the model. In total, it took 39.9 hours for this model to finish processing in Agisoft Metashape Professional (see Table 1 for processing information).

Of the 29 photos that were not used in the final model, four photographs were taken out by the estimation of image quality tool. This image quality estimation tool removed all the images that were too blurry to be of use before the sparse point cloud is even run. Three of these blurry photographs were removed from Look Angle 1, and one was removed from a higher look angle. Most of these photographs were taken from areas that were heavily shaded around the scene. For this model, all the remaining photographs were aligned in the sparse point cloud generation. During the optimization process, all the cameras that had less than 100 tie point projections (25 images) were also removed from the program. Twenty of these photographs were taken from the Close-Up Photographs; five were taken out from Look Angle 1 because of the lack of reference data from these two look angles. See Table 2 for a summary.



Figure 32. Overall screenshot of Model 2 showing an accurate representation of all the skeletal elements, clothing, and scales.

The resulting 3D model had an RMSE score of .421 pix, and the total scale error is .000268, indicating that the model is an accurate, scaled representation of the real-world scene. Overall, this textured model shows an overview of the relative position of all the elements present (Figure 32). This overall accuracy includes the location and orientation of identifiable bones, the contours in clothing, the interface between clothing and bones, the interface between bones and other bones, the interface between the subjects and the surface of the ground, and the representation of the scales around the perimeter of the scene. There appear to be very few areas

where the qualitative visual errors are present, looking at the overall overhead view of the 3D model.

Some slight visual errors become apparent from slightly zoomed-in screenshots. Figure 33 shows a slightly zoomed-in screenshot of the textured model and the geometry taken from the area involving the cranium, the mandible, five unserriated cervical vertebrae, the sternum (including the manubrium and sternal body), the right scapula, right humerus, radius, and ulna, five unserriated right ribs, and the hat. In this view, the visual distortions appear similar to the distortions present in the previous model. These visual distortions include ground surface-subject interface errors between the ground and some of the thin bones, including the ribs and vertebrae. However, despite these similarities, the scale bar in the upper left side does not appear to have any of the visual distortions present in the previous model.

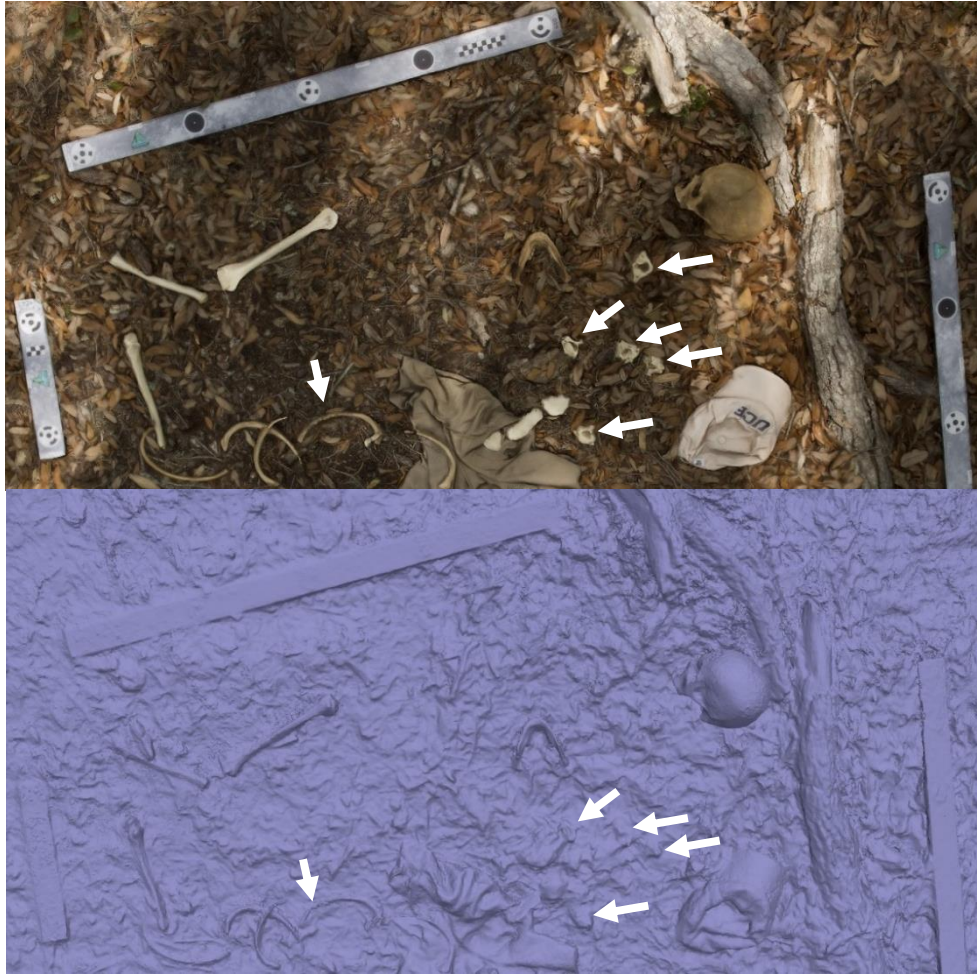


Figure 33. Zoomed-in screenshot of the texture (top) and geometry (bottom) of Model 2 showing most of the same visual error as the previous model. White arrows show areas with poor ground surface-subject interface on the ribs (left arrow) and on the cervical vertebrae.

Figure 34 shows screenshots of the texture and geometry of the torso region of Model 2 including the lower portion of the shirt, the left scapula and humerus, five unserriated lower vertebrae, one unserriated right rib, three unserriated left ribs, the sacrum, both os coxae, and the upper portion of the shorts. As with the previous model, there are subject-subject interfacing errors between the material of the shirt and one of the unserriated vertebrae, and there are both subject-subject and ground surface-subject interfacing errors between the vertebrae that are close together that seem to form one large mass in the geometry layer.



Figure 34. Screenshots of the texture (top) and geometry (bottom) of the torso region of Model 2. White arrows show areas of poor subject-subject interface and ground surface-subject interface in the areas of the vertebrae.

Figure 35 shows the textured and geometry screenshots of the lower leg region, including both left and right femora, tibiae, and fibulae, the right patella and calcaneus, three unserriated left ribs, and the left ulna and radius as well as both left and right shoes. In these screenshots, there is some slight visual distortion along the shaft of the left femur. There is also some poor ground surface-subject interface between the ground and a few of the unserriated left ribs and the left radius.



Figure 35. Screenshots of the texture (left) and geometry (right) of the lower leg portion of Model 2. White arrows are pointing out the misrendered geometry on the shafts of the left femur and tibia (on the left) and the ground surface-subject interfacing error on the ribs and the left radius (right).

Model 3

Data collection for Model 3 was conducted in the same manner as the previous two models. In total, 387 images were captured for this model taking 53 minutes to complete. Out of the 387 images that were taken, 358 were used to complete the model. In total, it took 102.56 hours for this model to finish processing in Agisoft Metashape Professional (see Table 1 for processing information).

Of the 29 photos that were not used in the final model, six were taken out by the estimation of image quality tool. This image quality estimation tool removed all the images that were too blurry to be of use before the sparse point cloud is even run. Four of these photographs were removed from the Close-Up Photographs, one was removed from Look Angle 1, and one was removed from a higher look angle. Most of these photographs were taken from areas that were heavily shaded around the scene. Next, five photographs were unaligned during the creation of the SPC and were removed from the program. Of these photographs, one was taken from the Close-Up Photographs, and four were taken from Look Angle 1. During the optimization process, all the cameras that had less than 100 tie point projections (18 photographs) were also removed from the program. All these photographs were from the Close-Up Photographs that consisted of a small area with little locational reference data to determine tie points. See Table 2 for a summary. During the modeling process, Agisoft Metashape Professional had a difficult time processing this model due to the number of dappled shadows present.

The resulting 3D model had an RMSE score of .393 pix, and the total scale error is .000294, indicating that the model has been accurately scaled to represent the real-world scene. Overall, this textured model shows an overview of the relative position of all the elements present (Figure 36). These relative positions include the location and orientation of identifiable bones, the contours in clothing, the interface between clothing and bones, the interface between bones and other bones, the interface between the subjects and the surface of the ground, and the representation of the scales around the perimeter of the scene. There appear to be very few areas where the qualitative visual error is present, looking at the overall overhead view of the 3D model.



Figure 36. Overall screenshot of Model 3 showing an accurate representation of all the skeletal elements, clothing, and scales.

As in the other models from this chapter, qualitative visual errors only become present in the zoomed-in screenshots of the model. Figure 37 shows a slightly zoomed-in screenshot of the head area, including the cranium, the mandible, five unserriated cervical vertebrae, the sternum (including the manubrium and sternal body), the right humerus, and the right radius. In the textured screenshot, it is apparent that there was a lighting change, and the photographs in this section tended to be overexposed. In this textured model, when shadows appear over the scene, these areas tend to appear fuzzy and indistinct. Despite this visual problem in the texture layer,

the underlying geometry does not appear to be affected by the shadows. The visual errors present in the geometry of Model 3 are similar to those present in the geometry of Models 1 and 2, including ground surface-subject interfacing errors present with the cervical vertebrae (Figure 37). There is also another area of ground surface-subject interfacing error between the ground surface and the right radius.



Figure 37. Screenshots of the textured (top) and geometry (bottom) of the head section of Model 3. White arrows are pointing out the ground surface-subject interfacing error in the right humerus (left) and the unserialized cervical vertebrae (right).

Figure 38 shows a slightly zoomed-in screenshot of the textured and geometry layers of the torso region of Model 3. This area includes the right ulna, six unserriated right ribs, the left scapula, humerus, and ulna, four unserriated left ribs, five unserriated lower vertebrae, the sacrum, and both os coxae as well as the shirt and the shorts. There are many instances of subject-subject interfacing error between the clothing and bones as well as between two bones. In this model, there are also a few instances of ground surface-subject interfacing error between the ribs and the ground surface, as well as some instances of misrendered geometry in the ribs where they appear to be missing sections in the geometry but appear complete in the model. The scale in the upper left of the screenshot shows some ground surface-subject interfacing error, possibly due to being covered by leaf litter.

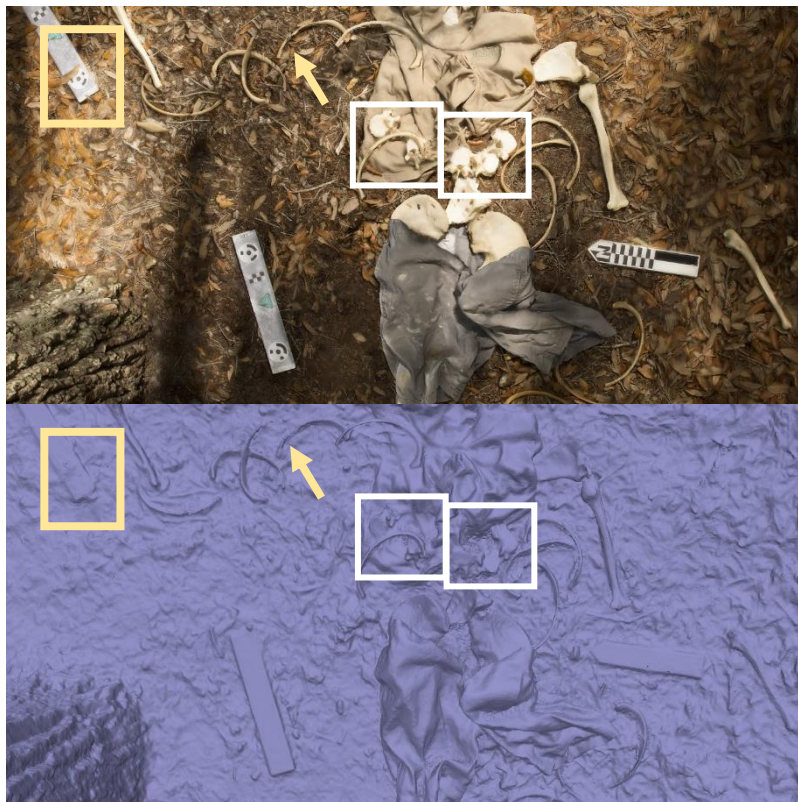


Figure 38. Screenshots of the texture (top) and geometry (bottom) of the torso region of Model 3. Ground surface-subject interfacing with the scale (Yellow box). The ground surface-subject interface error and misrendered geometry in the ribs (Yellow arrow). Subject-subject and ground surface-subject interfacing errors present in the lower unserriated vertebrae (White boxes).

Figure 39 shows the slightly zoomed in screenshots of the textured and geometry layers of the lower leg portions of model 3, including three unserriated left ribs, both femora, tibiae, and fibulae, the right patella and calcaneus, the lower portion of the shorts, and the right shoe. This area of the model shows very little visual error. The only apparent errors are the misrendered geometry on the shaft of the left tibia and the ground surface-subject interfacing error present in the scale, possibly due to the leaf debris covering it.



Figure 39. Screenshots of the texture (left) and geometry (right) layers of the lower leg portion of Model 3. White arrow showing the misrendered geometry on the left tibia, and the white box showing the ground surface-subject interfacing error on the scale bar due to leaf litter covering.

Table 2. Summary of the number of photographs excluded from each model.

Model	Total #	Excl. Close-up			Excl. 1 st Angle			Excl. 2 nd Angle			Excl. Higher Angle			Excl. Overhead			# In Model
		EQ	NA/SPC	<100 proj.	EQ	NA/SPC	<100 proj.	EQ	NA/SPC	<100 proj.	EQ	NA/SPC	<100 proj.	EQ	NA/SPC	<100 proj.	
1	281	2	25	12	3	11	4				1						223
2	279			20	3		5				1						250
3	387	4	1	18	1	4					1						358

*EQ = Estimation of Image Quality Step; NA/SPC = Not Aligned in the Sparse Point Cloud step; <100 proj. = Removed due to less than 100 projections after optimization

Table 3. Summary of qualitative visual errors

Model	Bone Geometry	Clothing Geometry	Scale Geometry	Ground Surface-Subject Interface	Subject-Subject Interface
1	Small bones tend to be misrendered (e.g., ribs, vertebrae); Left tibial shaft misrendered	Overall good	Leaf litter covering one scale	Small bones show poor interfacing errors (e.g., cervical vertebrae, sternal bones, and ribs)	Lumbar vertebrae interfacing errors between other lumbar vertebrae and shirt material; Head of left humerus and scapula fused in geometry
2	Slight distortion on left tibial and femoral shafts	Overall good	Overall good	Small bones show poor interfacing error (e.g., ribs and vertebrae)	Lumbar vertebrae interfacing errors between other lumbar vertebrae and shirt material
3	Slight distortion on left tibial shaft	Overall good	Leaf litter covering one scale	Small bones show poor interfacing error (e.g., ribs and vertebrae)	Lumbar vertebrae interfacing errors between other lumbar vertebrae and shirt material

Discussion

In cases where forensic archaeologists are consulted (i.e., human remains are significantly decomposed or skeletonized and need to be located, documented, or exhumed), the documentation of the context of the scene is of vital importance to any further investigation (Dirkmaat and Adovasio, 1997; Schultz and Dupras, 2008). This contextual importance is because evidence located at the scene, and the evidence of the remains themselves are often the only evidence that can be used to build an investigation. When documenting the context of outdoor forensic crime scenes, many confounding variables must be considered. Outdoor crime scenes, as opposed to indoor crime scenes, are exposed to a much larger variety of natural

phenomena (e.g., temperature, rain, insects, scavengers, etc.) that can change the crime scene over time (Mann et al., 1990). Especially in cases where scavengers have changed the scene, or gravity has rolled some remains down a slope, the context can become very complex and requires a great deal of documentation in order to recreate the original scene (Mann et al., 1990; Dirkmaat, 2012). There is general agreement that within the field of forensic science, the best documentation methods for these kinds of scenes come from the field of archaeology (e.g., Crist, 2001; Dirkmaat, 2012; Dupras et al., 2012; Schultz and Dupras, 2008).

These traditional methods of forensic crime scene documentation (e.g., hand-drawn maps and photography) are techniques that were taken directly from the field of archaeology and have been employed to document outdoor crime scenes by forensic archaeologists for many years (Dirkmaat, 2012; Dupras et al., 2012). The most important and most often used of these documentation techniques are maps, or 2D representations of the complex 3D surface of the earth (Dupras et al., 2012). Professionally created maps (e.g., topography maps and orthographic maps) are often useful for searching for forensic scenes when their location is previously unknown. During the documentation process, however, the most common types of maps used are hand-drawn maps to illustrate the exact location of all the features in relation to a fixed reference point and each other (Dupras et al., 2012; 162). There are a few methods that are commonly used for this, the two most common types of hand-drawn maps are baseline (an arbitrary line from which a more substantial area is mapped) and the azimuth system (a form of mapping with a central azimuth and measurements are taken from the center out using degrees to locate them on the map). In general, two levels of these maps are created. Before any recovery or detailed documentation of the scene is undertaken, a rough sketch map or site plan showing the general location of where the entire scene is situated should be drawn (Dupras et al., 2012). After

this is completed, documentation of the remains is completed using more detailed mapping techniques. When constructing these maps, all the maps of one scene must reference a single datum (a permanent point that is used to reference the map in location to other maps), so the location of the scene can be relocated after the evidence has been removed (Dupras et al., 2012).

During these processes, care should be taken not to move or disturb the crime scene in any way, as once the evidence at the scene has been disturbed, it can never be reconstructed precisely the way it was before being disturbed (Dupras et al., 2012). This also means that the forensic documentation process is a destructive one. Like in archaeology, once the evidence has been collected, the original provenience and context are entirely lost, so thorough documentation is imperative the first time (Dupras et al., 2012). Because of this, in recent years, there has been a call for the development and refinement of less destructive, more scientific forensic science methods (NAS 2009) and Dirkmaat (2012) has explicitly stated that there need to be more detailed and accepted methods of outdoor forensic crime scene documentation.

The use of CRP has been proven in cases of archaeological excavation to provide a cost-effective and detailed 3D documentation of the context of outdoor scenes (e.g., Douglass et al., 2015; Forte, 2014; Garstki et al., 2018; Novotny, 2019). Further advantages of this technique are the use of equipment already employed in the documentation of forensic scenes (digital cameras) and short initial scene processing time, resulting in fast data collection to ensure little contextual evidence is lost. This documentation process also does not require interaction with the forensic scene whatsoever so that the original context is preserved in its entirety. Because of fast technological advancement, software needed for processing 3D photogrammetry models has become more affordable in recent years (Forte, 2014) as opposed to laser scanning technology, which remains an expensive alternative. The next sections will discuss some of the limitations of

CRP, including time, uncontrollable weather conditions, and lighting conditions. Next, the number of photographs needed to complete a 3D model will be discussed. Finally, guidelines will be given for integrating these data collection methods into established forensic archaeological methods.

Time and weather complications

As with more traditional methods of forensic documentation, one of the most challenging complications with using close-range photogrammetry to document outdoor scenes is the short amount of time researchers have in the field as well as interference with the natural elements. Close-range photogrammetry has the potential to help mitigate the time constraints under which forensic scientists frequently find themselves working. As opposed to hand-drawn maps that require painstaking measurements and may take hours to complete, data collection for close-range photogrammetry models takes significantly less time. In the case of this research, the longest amount of time for data collection was 53 minutes to collect 387 images. CRP methodology also does not require researchers to interfere with the scene at all. While hand-drawn maps require measurements of the objects of interest, possibly causing interference with the original context of the scene, photogrammetry only requires the researcher to interact with the outskirts of the scene. Using this methodology, the researcher can mitigate their influence on the contextual information documented, and accurate measurements can be taken from the resulting final model.

Weather conditions, including wind, rain, and sunlight, are the most complicated factors to consider when using CRP, as they are with the traditional documentation methods. The wind has the potential to disturb the ground materials and smaller bones, moving these elements around the scene. Because photogrammetry relies on the identification of convergent points in a

series of photographs, items in the photographs moving around can cause misalignment of the photographs or artifacts in the final model that were not present in the original scene. This problem often happened when the wind blew leaves over the top of scales and resulted in the photographs being taken out of the final model because the image could not align. This interference with leaves on top of scales also resulted in many cases of ground surface-subject interfacing errors between the ground surface and the scales (see Table 3 for a summary). Rain is a huge complicating factor with CRP, mainly because the primary documentation method is a digital camera. There is also the same problem faced with the wind, as rain can cause objects to move around the scene. Fortunately, this was the weather condition that was faced the least for this research.

For this research, the main issue faced was the sunlight, which caused shadows over the scene. Especially in wooded areas, dappled sunlight over the scene frequently caused issues during the modeling process. Many of the photographs that were taken out of the final model were out of focus, underexposed, or overexposed, causing issues with modeling bones and clothing. When a photograph was taken from an area of the scene dominated by shadows but pointed towards a bright area, the photograph tended to be overexposed and unfocused. The reverse was also true; if the camera was positioned in the sunlight and focused on a shaded area, the resulting photograph was underexposed and unfocused. All of these under and overexposed photographs were removed from the program before the model was created. This is an issue that might be resolved by using different camera settings such as the aperture priority setting where the field of focus is chosen by the researcher, but other settings are fluid based on the lighting conditions.

Dappled shadows also caused some modeling problems in the photographs that were still used in the model. For Model 3, a visual inspection of all the photographs was conducted, and the photographs that contained overly dark shadows were disabled from the texture layer. These photographs were still used to create the geometry of the model but were disabled for the generation of the texture to clean up the visual presentation of the final model. In cases like this, the visual representation of the texture was improved while keeping the same underlying geometry. If there are enough photos to create a complete texture of the scene, eliminating photographs from the texture layer does not compromise the integrity of this layer. In fact, as in this case, removing some visually distorted photographs can remove the issues seen in the texture of the model.

Number of photographs needed

According to the guidelines in Agisoft Metashape Professional user manual, the number of photographs required to complete a model is stated as “more than required is better than not enough” (Agisoft, 2019; 9). The only other guidelines provided for determining a sufficient number of photographs have been suggested for aerial photogrammetry. This suggestion is that a 60% side overlap and an 80% forward overlap should be utilized (Agisoft, 2019; 9). Other than this, there is no clear guideline on how many photographs should be taken, how many look angles should be used, or even how much overlap should be present between photographs for CRP projects. However, other authors have suggested that a general rule of 2/3 overlap is suggested for CRP projects (CHI, 2019; Douglass et al., 2015). In general, it is acknowledged that the more overlapping points the photographs have in common, the better the final model (Gidusko, 2018; 22). While using at least three look angles is advised (Douglass et al., 2015), using only three look angles can result in a higher number of visual errors than expected.

As in every project, the number of photographs will fluctuate based on the situation at hand. If the scene is large and complex, a greater number of photographs will be needed to capture the convergent angles of the entire scene. It is also essential to capture photographs from multiple look angles in order to be able to manipulate the scene and see it from all angles. It was discovered during a preliminary trial of research that overhead shots of the scene are necessary to create an orthophoto of the scene from the overhead view. The more look angles that are present, the more complex geometry the computer can render because the photographs will capture more nuanced details such as the folds of clothing or the overlay of leaves on top of each other. However, the number of photographs may also be limited by time, file storage availability, and processing time. More photographs will always mean more time taken, larger files to store on computers, and significantly longer processing times. According to guidelines provided by the Agisoft Metashape Professional user manual (Agisoft, 2019), the researcher should always take more photographs than they think they will need. This is especially true in the case of forensic investigation, where the scene is destroyed shortly after being documented. Because of all the different variables involved, there is no single magic number of photographs that is right for use in photogrammetry, but there does need to be enough to record all the information needed to complete a 3D model as well as enough to document the context of the entire scene. In general, the research confirms that the 3D models with the greatest number of photographs are those that appear to have the fewest qualitative visual errors (see Table 3 for more details).

Guidelines for integrating CRP

Integrating this technology into the traditional scene documentation protocol will not be a significant expense because many law enforcement agencies already own the majority of the field equipment that is required when adapting this data collection methodology. This includes

equipment like digital cameras and extension poles for the cameras. However, there may still be some small investments involved. These include the software needed to create 3D models, and Cultural Heritage Imaging (CHI) photogrammetric scale bars. When deciding on which software to use for 3D models, there are many options available, including free, open-source photogrammetry software. Before purchasing or using one software program over another, some research should be undertaken when determining the resulting 3D model quality, hardware requirements, and level of control the researcher has on the final product. Many of the software options that produce detailed, accurate, and scientific-quality 3D models (e.g., Agisoft Metashape Professional), will require a small investment that will be significantly less than any other 3D documentation technology available (e.g., laser scanning). Using CHI scale bars is also optional. Any form of scale can be used to scale the model; however, for the most accurate measurements to be taken from the 3D model, CHI scales are recommended. These scales integrate coded targets that are registered by the photogrammetry software as tie points and have been calibrated, so the distance present on the scale bar is accurate to within one-tenth of a millimeter. If CHI scales are not used, another form of tie point should be used, such as coded targets provided within the Agisoft Metashape Professional software.

The second step, once at the scene, is to define the boundaries of the scene. This boundary definition should utilize traditional forensic archaeology survey techniques (see Dupras et al., 2012, for more details). As mentioned above, this step can become complicated when working in outdoor scenes where remains may have been exposed to confounding variables such as animal scavengers or slope of the ground. However, this is a crucial step to make sure the entire context of the scene is documented, so researchers should make sure all the remains have been found before proceeding to the next steps. Once the boundaries have been determined, a

rough sketch map showing the boundaries of the scene in relation to a fixed point should be drawn. This map just serves the purpose of providing a broader overall context of the location of the entire scene that is not included in the 3D model.

The third step will be to decide how many photographs and possibly how many models will be necessary to document the entire scene. As discussed in length above, the number of photographs needed to create a 3D model is a complicated process that requires many variables to be considered (e.g., size of the scene, the complexity of the ground surface, etc.). However, before data collection begins, there should be a rough goal of how many photographs will be taken either in total or per look angle. This set goal of photographs should most likely be a minimum, as more photographs than needed will always be better than not enough photographs. In instances where the remains are distinctly separated (e.g., the cranium rolled down a hill, but other remains are still in situ at the top of the hill), or the scene is so large the number of photographs needed may be too large to run on a computer, it may be beneficial to use multiple models to document two different sections of the scene instead of documenting the entire scene. These decisions will be up to the researcher; however, they should be decided before data collection begins because they will affect the precision of the final methodology.

Step number four will be to clear the vegetation around the scene. This clearing of vegetation is a common practice in forensic archaeology, so tools (e.g., handsaw, hand clippers) should already be readily available for forensic archaeologists (Dupras et al., 2012). The goal of this step is to clear out as much undergrowth as possible from inside the scene and a buffer area around it so the entire scene can be documented clearly from all angles. The buffer area around the scene is essential for the documentation of the scale bars around the scene, and for the researcher to be able to move around the scene without disturbing the remains.

For step number five, the perimeter of the scene should be defined using the scale bars. For this research and most archaeological research, calibrated photogrammetric scale bars are used for this step; however, as stated above, this is recommended, though not strictly necessary. If CHI scales are not used, other forms of accurately scaled scale bars can be used if the error is known. If other forms of scale bars are used, it may be necessary to incorporate coded targets throughout the scene to be used as tie points. These targets can be placed inside the scene, making sure they are in areas where they are not obstructing any subject material. If using Agisoft Metashape Professional, these coded targets can be found under the “tools” drop-down menu and can be printed from there.

Step six is to document the crime scene using the steps described in the methods section of this chapter. According to the Agisoft Metashape Professional user manual (Agisoft, 2019), there should be at least three look angles used. Through preliminary research, it has been determined that more than three look angles should be used, and one of these look angles should include one that is taken from directly over the scene. These look angles maximize coverage for the entire scene and guarantee enough photographs to document the scene in its entirety. If hand-drawn maps are still wanted to be sure traditional forensic archaeological documentation processes are followed, or to ensure back-up of the digital data, hand-drawn maps should be made after photogrammetry data collection has taken place. This sequence of events is to ensure little context is lost due to human involvement of the scene, as CRP requires little interaction with the scene itself. Because this is a relatively new technique to the application of outdoor forensic scene documentation, hand-drawn maps may be needed at first; however, it is possible that in the future, CRP may replace the hand-drawn map documentation method.

Conclusions

This research shows that with enough photographs (which depend on the size of the scene, time constraints, weather conditions, etc.) taken at multiple look angles, CRP can be used to produce accurately scaled 3D models that are virtual representations of the outdoor forensic crime scenes. There are many advantages of this methodology, including the fact that it is cost-effective, it uses equipment such as digital cameras that are already used at crime scenes, there is no interaction with the scene, so context is preserved, and the 3D models can be virtually manipulated and used to reconstruct events.

CHAPTER THREE: APPLICATION OF PHOTOGRAMMETRY ON DIFFERENT GROUND SURFACES USING DIFFERENT IMAGE COLLECTION TECHNIQUES

Introduction

Photogrammetry is the science of making reliable measurements of physical objects using photography (Barazzetti et al., 2012; Hoogeboom et al., 2015). The basic idea behind photogrammetry is that points represented in multiple photographs taken of the same object or scene at convergent angles can be triangulated on three planes (x, y, and z) to reconstruct the three-dimensional object based on perspective and projection geometry (Barazzetti et al., 2012; Hoogeboom et al., 2015). In the current age of digital photogrammetry (Linder, 2003), advancements in camera technology, as well as computer hardware and software, have made the process of photogrammetry significantly more accessible and affordable to different fields of study (Forte, 2014).

This technique has been used extensively within the field of archaeology and has been explicitly used for the preservation of the three-dimensional (3D) context of the scene being excavated (Forte, 2014). Three-dimensional (3D) documentation provides advantages over two-dimensional (2D) photographic documentation because it allows for the visualization of the entire scene in x, y, and z planes and the relative position of all components on these planes (Hoogeboom et al., 2015). Digital 3D photogrammetry data collection also allows for digital manipulation of the scene in virtual space, unlike single 2D images of the scene. This feature could be useful for reconstruction of events without destruction of the scene, reconstruction of the scene after it has been disturbed by the investigation, and preservation of the entire context of the scene that was documented. Despite these valuable applications, this technique has been underutilized in the related field of forensic archaeology, where the collection and preservation of the context of forensic scenes are the main goals. However, the painstaking process of

drawing maps by hand is still the primary method of documentation (Dirkmaat, 2012; Dupras et al., 2012).

The purpose of this chapter is to assess the capability of photogrammetry in the documentation of skeletal scatters on different ground surfaces commonly seen in forensic cases in central Florida. This will be completed by first creating six mock forensic crime scene scenarios of areas where clandestine body disposals have resulted in slightly scattered human skeletal remains. Next, data collection techniques that were used to photograph the scene, and the best data processing parameters used to create accurate 3D models will be described. Finally, a discussion of the comparative accuracy of the 3D models will be followed with a conclusion of the best practices for the documentation of this type of outdoor scene.

Background

In the field of archaeology, photogrammetry has been used to document a great deal of information. This technique has been used as a non-invasive way to document and inform the preservation of sites (e.g., Al-Ruzouq and Dabous, 2017; Douglass et al., 2015; Howland et al., 2018; Jalandoni et al., 2018). It has also been used to document and reconstruct ongoing excavation projects (e.g., Forte, 2014; Garstki et al., 2018; Haukaas and Hoodgetts, 2016) and small-scale artifacts (e.g., Forte, 2014; Samaan et al., 2013). In many cases, close-range aerial photogrammetry has been used to survey, map, and discover new archaeological sites (e.g., Casana et al., 2014; Chiabrande et al., 2018; Pierdicca, 2018). Researchers have also used CRP to document biological archaeology cases involving human skeletal remains (e.g., Forte, 2014; Novotny, 2019).

In the field of forensic science, the primary use for photogrammetry thus far has been for the reconstruction of events at the crime scenes (Bollinger et al., 2012; Buck et al., 2007; Buck et al., 2013; Constantino et al., 2016; Maksymowicz et al., 2014; Villa et al., 2018). In these cases, the photogrammetry software is used in conjunction with other 3D reconstruction software such as computer aid design (CAD) software in the reconstruction (Bollinger et al., 2012; Buck et al., 2007; Buck et al., 2013; Constantino et al., 2016; Maksymowicz et al., 2014; Villa et al., 2018). Photogrammetry by itself has been used to document specific lines of evidence at crime scenes (Agosto et al., 2008; Andalo et al., 2011). These studies have included the documentation of blood spatter evidence (Agosto et al., 2008), and the study of footprint impressions on different surfaces (Andalo et al., 2011). However, in both these studies, photogrammetry is not the only documentation method with Agosto and colleagues (2008) providing walk path analysis on the footprints using a geographic information system (GIS) program, and Andalo and colleagues (2011) comparing the results of laser scanning technology, traditional casting methods, and photogrammetry methods.

Photogrammetry has also been used in a limited capacity to document the entire context of mock forensic crime scenes (Barazzetti et al., 2012; Behring et al., 2001; Gidusko, 2018; Grip et al., 2000; Urbanova et al., 2017; Villa et al., 2018; Zancajo-Blazques et al., 2015). While forms of photogrammetry were used in all these studies, many of them also involved the same limitations as above. Barazzetti and colleagues (2012) use photogrammetry as one method in conjunction with laser scanning technology to document the crime scene. Both Behring et al. (2001) and Villa et al. (2017) use 3D CAD technologies to reconstruct the events of the scenes instead of relying only on photogrammetry to show the context of the scene. Grip et al. (2000) and Urbanova et al. (2017) show the applications of aerial photography to the field of forensic

science. Aerial photogrammetry utilizes aerial photographs taken from over 1,000 feet in the air by either a plane or a satellite (Mathews, 2008). In the case of Grip and colleagues (2000), aerial photogrammetry was used to document outdoor environmental forensic scenes through the process of orthorectification. Urbanova and colleagues (2017) show the applications of close-range aerial photogrammetry (less than 1,000 feet) taken using an unmanned aerial vehicle (UAV). Despite these studies that use photogrammetry to document crime scenes, there is still a lack of studies conducted on the use of close-range photogrammetry (CRP) to document the entire context of human skeletal material in situ at the scene.

While there has been some use of this technique in archaeology to document ancient burials and skeletal material (see Forte 2014), this remains a neglected area when it comes to modern forensic cases. Three studies to date have used human remains in their documentation of outdoor forensic crime scenes. In 2012, Barazzetti and colleagues created two mock forensic crime scenes involving a limited number of scattered human bones (including a single cranium and a few long bones) and used multiple-ranged laser scanners integrated with close-range photogrammetry to create overall 3D models of large-scale scenes. In 2017, Urbanova and colleagues demonstrated the capabilities of small cameras mounted on commercial drones to produce high-resolution models of an entire crime scene and used a limited number of real human bones for their second experimental scenario. Finally, in 2018, a pilot study by Kevin Gidusko used faux skeletal material to create mock forensic scenes involving burial scenarios as well as large and small scattered remains scenarios. The documentation of the scene by Gidusko (2018) showed that photogrammetry has the potential to be used in this context, however, the use of faux skeletal material provided unforeseen complications to the 3D modeling process. There is also a need for continued research in this field to determine the exact parameters needed to

document scenes involving scattered human remains on complex ground surfaces and to determine the best documentation methods in these settings. The research presented here is a continuation of the research published by Gidusko (2018) that uses a real composite human skeleton and focuses on small scattered human remains on a variety of ground surfaces commonly found in the state of Florida.

Overall, as shown by the previous research on the subject, photogrammetry is only recently becoming integrated into the field of forensic archaeology for crime scene documentation. Gidusko's (2018) thesis provides a complete analysis of photogrammetry used for data collection from outdoor scenes. However, this was a pilot study and still requires data collection development and further discussion of 3D processing methods to further decrease visual errors in both the bone geometry and in the interface between the ground surface and the bones. Most specifically, data collection needs to involve real human bone in order to apply to real forensic crime scenes. Gidusko's (2018) research did illustrate that photogrammetry is a viable method of context documentation that can be applied in the field of forensic archaeology. Photogrammetry is also uniquely applicable because the equipment used for data collection, any standard digital camera, is already equipment used by crime scene investigators (CSI) to document crime scenes. Given these facts, it is surprising that photogrammetry has not been studied or used more often for crime scene documentation.

Materials and Methods

Equipment and Scene Preparation

For this research, the materials used in the initial photographic documentation process include a Nikon D7200 camera, a tripod, an extension pole, and a remote shutter release. The

skeletal material that was used was a composite skeleton created from the osteological collection held by the Anthropology department at the University of Central Florida. All material was chosen based on relative size, morphology, and color consistency with other skeletal material. The complete inventory included one cranium, one mandible, both left, and right scapulae, humeri, radii, and ulnae, two unserriated and unsided metacarpals, five unserriated cervical vertebrae (including the atlas and the axis), three unserriated lumbar vertebrae, fifteen unserriated and unsided ribs, one sternum (manubrium and body) one sacrum, both left, and right os coxae, femora, tibiae, and fibulae, one left patella, one right calcaneus, both left and right tali, one left navicular, and three unserriated and unsided metatarsals. Clothing (including one shirt, one hat, one pair of shorts, and one pair of sneakers) was added to create the mock scenes and was incorporated into the scene interacting with the bone material (i.e., some bones were inside the clothing) in order to create more realistic circumstances for a forensic crime scene.

This research was conducted at the University of Central Florida natural lands at multiple locations that were predetermined based on the contents of the ground surface. Once the location was determined, the skeletal material and clothing were laid out in relatively the same position at each scene. Next, the limits of the scene were determined, and Cultural Heritage Imaging (CHI) calibrated photogrammetric scale bars were set around the boundary of the scene. These scales are specially designed for photogrammetry and are professionally calibrated to 1/10th of a millimeter (.001 meter) or better accuracy (CHI, 2020). The coded targets present on the scale bars were used in later processing of the model as tie points, and the distance between the targets was used to scale the models and to help determine accuracy during analysis. When the scene was set up, the vegetation around the bones and scales was cleared in order to see the entire scene in the photographs. A buffer area on the perimeter of the scales was also cleared to make

sure the scales were not obstructed while moving around the perimeter of the scene to take photographs. Next, the camera settings were chosen based on the variables present at the scene (lighting, size of the scatter, shadows, etc.) as well as prior research conducted by Gidusko (2018) and some guidelines provided by the Agisoft Metashape (2019) processing manual. Finally, the method of photography (handheld, tripod, etc.) was determined in order to compare these three data collection techniques to each other. Each scene was documented using only one data collection technique. These steps can be better visualized in Figure 40.

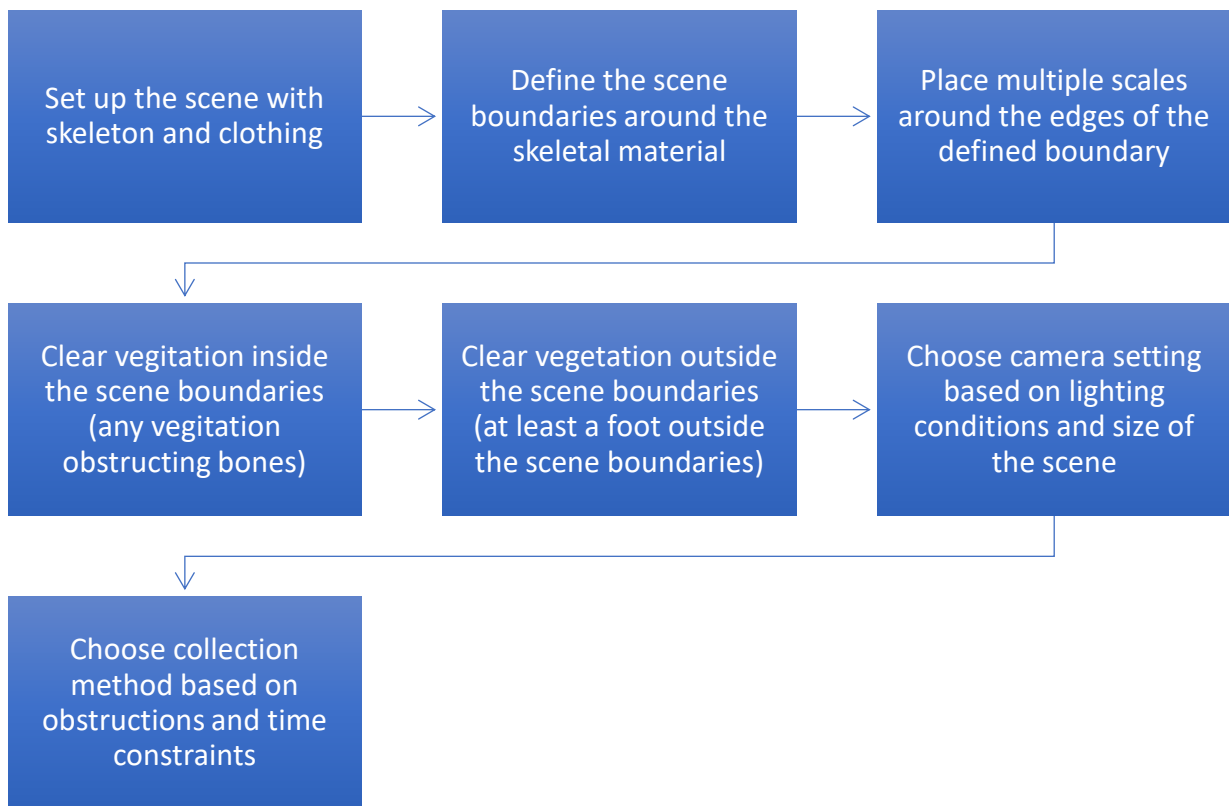


Figure 40. Steps taken during set-up and preprocessing of the scene.

Data Collection Methods

The NIKON D7200 camera was used for data collection of the scenes. Photographs were collected in RAW format and were then pre-processed into TIFF files using Adobe Bridge before

they could be uploaded into the photogrammetry software. Data was collected using a variety of photography techniques including a tripod, a handheld extension pole (monopod), and using handheld photography.

Following data collection guidelines present in the Agisoft Metashape Professional (2019) user manual, photographs were taken from at least three look angles around the perimeter of the scene. This is done to ensure that there is at least a 2/3 overlap between consecutive photographs and that all areas of the scene are present in at least two photographs (CHI, 2020). For this research, it was determined that at least five look angles were required to create a complete and accurate 3D model (Figure 41). These look angles included one close to the ground and moving slightly higher at each look angle until finally taking photographs from directly over the scene with a handheld extension pole. It was found in a small pilot study that these overhead photographs were required to create more accurate orthomosaic photographs of the overall scene.

All the scenes were photographed using different techniques to create comparison models of the scene (See Table 4). Each scene was photographed using only one photography technique; a tripod (Model 4), a monopod (Model 5), or handheld (Model 6). With the tripod and extension pole, the heights were gained by beginning on the lowest level possible using the tool, and each level after that consisted of extending the legs to the next segment until the last angle was collected and the legs were fully extended. For the handheld technique, the photographer started on their knees with the camera as low to the ground as possible and at each level began to stand up until they were standing with their arm extended overhead. In general, this consisted of kneeling with the camera close to the ground for the first angle, kneeling with the camera held at about mid-torso level, kneeling with the camera held at the eye-level, standing up and holding the camera at chest-level, standing and holding the camera at eye-level, and using the overhead

extension pole to collect the overhead photographs. The look angles used for the handheld techniques were less standardized than the tripod or extension pole techniques because they relied on a human’s estimation of standard heights. However, this method also allowed for more flexibility for photographing from different angles at a single position by simply turning and angling the camera in that direction. After all the look angles had been completed, photographs were taken of the scene overhead using the handheld extension pole with one person holding the pole overhead and another person operating a remote shutter release.

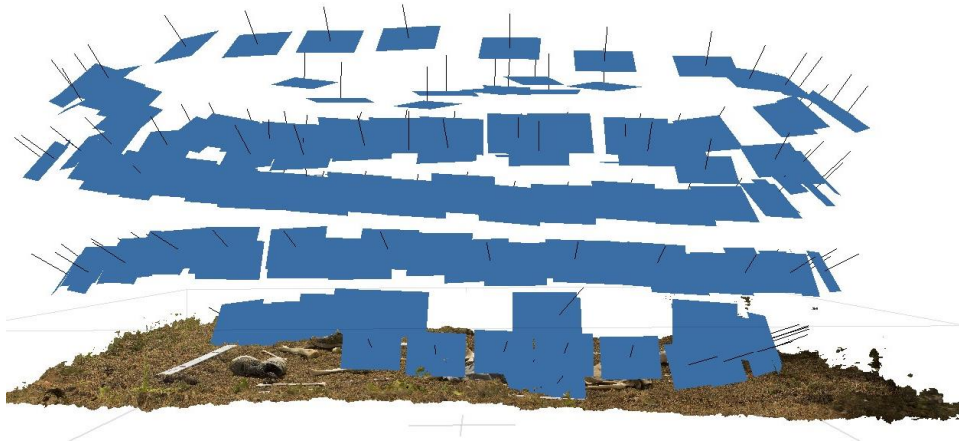


Figure 41. Screenshot from Agisoft Metashape illustrating the look angles.

Table 4. Summary of the information for models used in Chapter 3.

Model	Ground Surface	Photo Collection	# Look angles	Camera Setting	Focus	Total Photo	Photos used	Image Collection Time	Processing Time
4	Grass/Dirt	Tripod/Pole Over/Freehand Close	6/Close-up	AP ISO800 f/11	A	379	343	58M	160.04 H
5	Pine Needles	Monopod/Pole Over/Freehand Close	5/Close-up	AP ISO400 f/11	A	222	148	29M	23.08 H
6	Leaves/Dirt	Handheld/Pole Over	6/Close-up	AP ISO800 f/18	A	397	360	34M	145.54 H

Model 4

This scene consisted of a small scatter (approximately 3.5 by 2 meters) of human skeletal material on a surface of mixed grass, soil, and pine needles with a canopy of trees overhead. The complete inventory of skeletal remains consists of one cranium, one mandible, two cervical vertebrae (the atlas and the axis), one sternum (manubrium and body), left and right scapulae, left and right humeri, radii, and ulnae, three right ribs, six left ribs, four lumbar vertebrae, one sacrum, left and right os coxae and femora, a right patella, left and right tibiae and fibulae, and one right calcaneus. Clothing consisting of a shirt, shorts, hat, and two shoes were also set out to help simulate a crime scene.

Data collection for this model took approximately 58 minutes. The camera was set to automatic focus, and aperture priority setting with the focal length stabilized at 18mm, the f-stop at F/11, and ISO800. The tripod was used to take the first five look angles, starting from as close to the ground surface as possible and moving up. Once that was completed, the extension pole was used to take overhead photographs of the scene. Using this technique, two people were needed to operate the camera, one person to hold the pole and another to operate the remote shutter release that was necessary. Finally, close-up images were taken of areas of interest around the scene, particularly of areas that had complex geometry or areas where there was concern about the coverage from the overall photographs. Altogether, 379 photographs were taken for Model 4.

Model 5

This scene consisted of a small scatter (approximately 3 by 2 meters) of human skeletal material on a surface dominated by pine needles with a canopy of coniferous trees overhead. The

complete inventory of skeletal remains consists of one cranium, one mandible, three cervical vertebrae (the atlas, axis, and an unserriated vertebra), one sternum (manubrium and body), left and right scapulae, left and right humeri, radii, and ulnae, two right ribs, six left ribs, four lumbar vertebrae, one sacrum, left and right os coxae, femora, tibiae and fibulae, and one right calcaneus.

Data collection for this model took approximately 29 minutes. The camera was set to automatic focus, and aperture priority setting with the focal length stabilized at 18mm, the f-stop at F/11, and ISO400. Model 5 was photographed using a monopod to standardize the look angles. The bottom level was taken using the handheld method because of the limiting lowest height of the monopod. After this, four look angle levels were completed using the monopod for semi-standardized heights. Finally, overhead photographs and close-up photographs of the interior of the scene were taken in the same way as described above. Altogether, 221 photographs were taken for Model 5.

Model 6

This scene consisted of a small scatter (approximately 3.5 by 2 meters) of human skeletal material on a surface of mixed leaves and dirt with a canopy of trees overhead. The complete inventory of skeletal remains consists of one cranium, one mandible, four cervical vertebrae (the atlas, axis, and two unserriated vertebrae), one sternum (manubrium and body), left and right scapulae, left and right humeri, radii, and ulnae, six right ribs, six left ribs, five lumbar vertebrae, one sacrum, left and right os coxae and femora, one right patella, left and right tibiae and fibulae, and one right calcaneus.

Data collection for this model took approximately 34 minutes. The camera was set to automatic focus, and aperture priority setting with the focal length stabilized at 18mm, the f-stop at F/18, and ISO800. For Model 6, the handheld method was used to take photographs from the first four look angles around the scene. Overhead photographs using the handheld extension pole and the close-up photographs were taken as described above. Altogether, 397 photographs were taken for Model 6.

Pre-processing Photographs

All photographs were pre-processed before they could be loaded into the photogrammetry software. An established file system was used to help keep the data organized. Photographs for this project were taken in both RAW and JPG formats simultaneously. The Agisoft Metashape Professional (2019) user manual suggests taking photographs in RAW format and converting them into TIFF files because the compression of JPG images can cause unwanted noise in the 3D model. This conversion from RAW to TIFF format was done using Adobe Bridge software. The TIFF files were then uploaded into Agisoft Metashape for photogrammetry processing.

Processing in Agisoft Metashape

Once the file format had been changed to TIFF files, the images could be uploaded into the Agisoft Metashape software to be processed into 3D models. When the images had been uploaded, a marker registration program was used to detect the markers on the scales. The rest of the processing procedures were completed following the guidelines present in Agisoft (2019) Metashape Professional user manual and using the processing procedures present in USGS (2016) and Mayer et al. (2018).

The processing of the 3D models in Agisoft Metashape Professional followed the same guidelines and settings described in Chapter 2. This process involved three general steps: 1) creating the sparse point cloud (SPC), 2) optimization of camera positions from the SPC, and 3) creating a batch process to generate the dense point cloud, the mesh, the texture, and the orthophoto of the 3D model (Figure 42). First, the position of the photographs taken around the scene was calculated by creating a sparse point cloud (Agisoft, 2019). Next, the SPC was optimized based on the general guidelines present in the Agisoft Metashape Professional (2019) user manual and summarized by Mayer and colleagues (2018). Finally, in the interest of time, a batch process was set up to generate the dense point cloud (DPC), the mesh, the texture, and the orthophoto. After everything has been processed, a report was created that shows all the processing parameters as well as the time it took to complete the steps and survey statistics of the resulting model (Agisoft, 2019). Figure 43 presents an overview of the workflow used for this photogrammetry project.

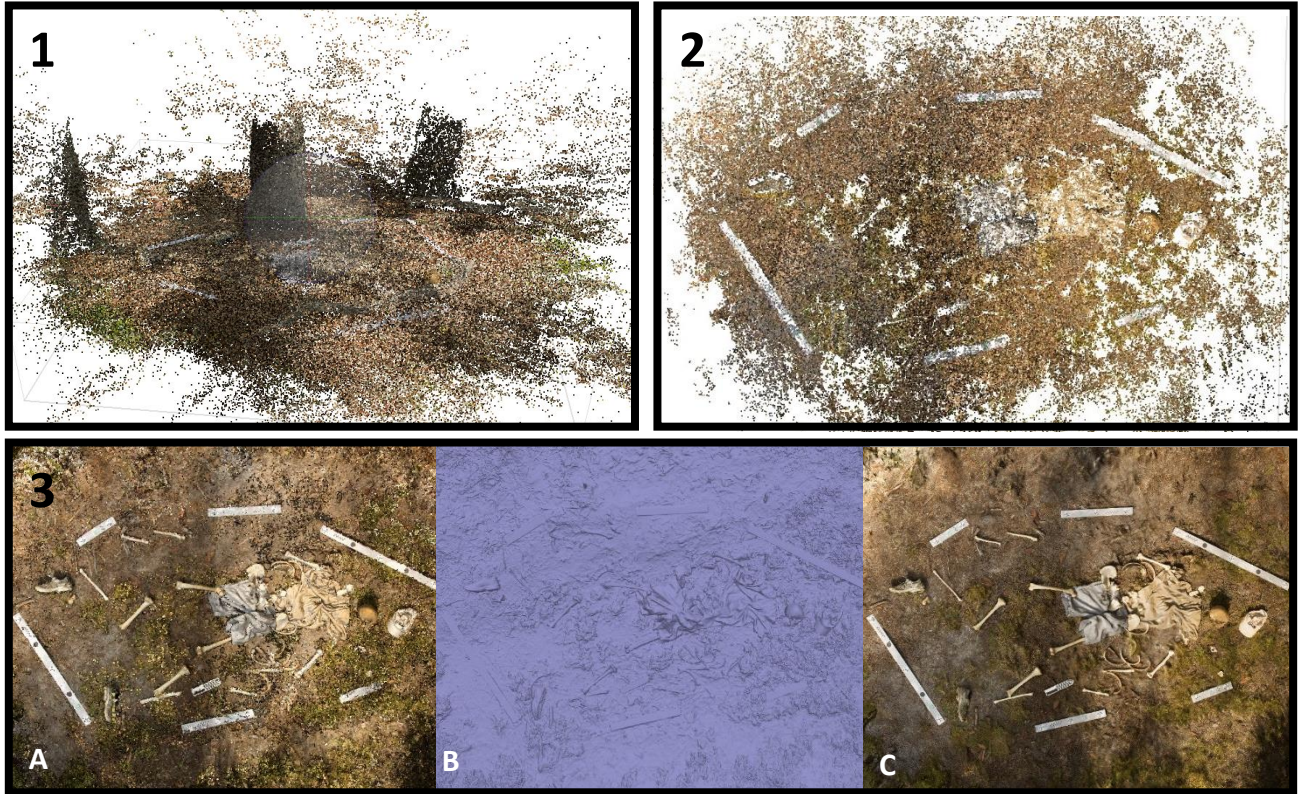


Figure 42. Screenshots from the Agisoft Metashape Professional software program showing 1) the sparse point cloud, 2) the optimized sparse point cloud, 3) the batch process which consists of 3A) the dense point cloud, 3B) the mesh layer, and 3C) the textured 3D model.

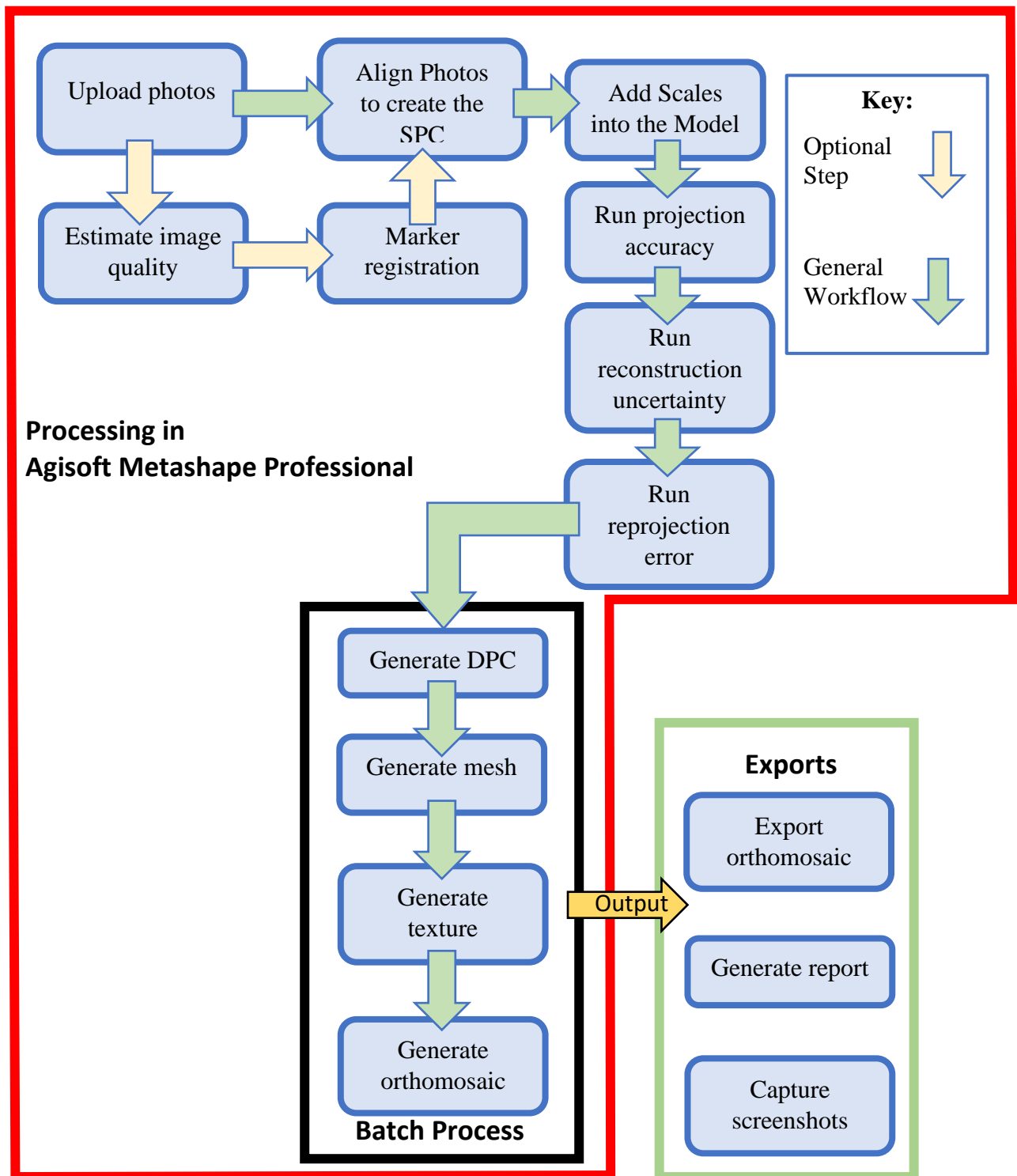


Figure 43. Workflow for processing a 3D model in Agisoft Metashape Professional software.

Post-Processing – measures of error and accuracy

Despite photogrammetry existing for a great deal of time, there is no universally acknowledged method for the evaluation of the accuracy of digitally created 3D models. The most commonly used description of accuracy has been a comparison of real-world measurements to the measurements taken of the digital 3D model within the computer program (Caroti et al., 2014, De Reu et al., 2014, Doneus et al., 2011, Douglass et al., 2015:145, Gidusko, 2018; Rieke-Zapp et al., 2009). In cases involving human remains, measuring skeletal material based on the 3D model is not helpful as the remains will be removed and measured according to osteometric standards. Adding scales into 3D models is more important for showing the relative positions of subjects within the scene. For this research, no measurements of the remains were compared to the real osteometric measurements. Instead, the estimation of error was used to show the model has been accurately scaled. Because the CHI coded scale bars are accurate within .001 (CHI, 2020), if the estimated error is less than .001, the model was determined to be accurately scaled. This error estimation only addresses the error present when the scale bars are added, it does not address error that is inherent in the model itself. In order to better assess error that is present in the final model, other quantitative and qualitative indications of error must also be evaluated.

The error of a 3D model is described as the difference between the point given in a photogrammetry model and the known position of that point in the real world (Jennings and Black, 2012). One measurement of error that is most commonly reported and is given by the photogrammetry software is the root mean square error (RMSE), which is a statistically determined standard deviation of error seen in the model per pixel (CHI, 2020). In general, an RMSE value of less than one is recommended (Mayer et al., 2018). However, this indicator can

also be problematic because it is an indication of the average, but there are still outliers present (Jennings and Black, 2012). This number also does not show the exact areas where the error is within the model. While both these error indications will be reported, much of the discussion of error will focus on a qualitative visual comparison of 3D models to each other and to the real-world scene (as done by Gidusko, 2018).

These qualitative visual errors include: assessment of the visual representation of the bones; assessment of the visual representation of scales and clothing; assessment of the interface between the ground surface and the subjects (bones, clothing, or scales); and assessment of the interface between two or more subjects. Assessing the visual representation of bones includes looking at areas of misrendered geometry in the model (or areas in the model where sections of the subject appear missing in the geometry layer). This should be distinguished from visual distortion on an object of interest (or areas where there is error in the texture layer while the object is present in the geometry layer). In order to assess the qualitative visual errors present, standardized screenshots will be used to show key areas of the scenes. These will include an overall screenshot of the final model, a comparison of the screenshots of geometry and texture models for three key areas including the cranium and mandible, the axial skeleton, and the lower long bones.

Results

Overall, the average RMSE score of every model (see Table 3), as shown in the reports (Appendix A), was less than 1, indicating an accurate 3D point reconstruction was completed (Mayer et al., 2018). The overview screenshot of each model shows the accurate context of the location of skeletal remains in relation to other objects of interest in the scene with relatively little visual distortion errors. It is only when the model is zoomed in that small visual errors

become visible. These errors fall under the categories discussed in the section above. The following sections will detail these errors for each model.

Model 4 – Mixed surface dominated by grass

Model 4 generation parameters

For this model, 379 photographs of the scene were taken. During the camera alignment process, 343 photographs were aligned and used to create the model. Of the 36 photographs that were not used in the model, three of them were removed during the estimation of image quality step. In this case, all four images were removed because of inconsistent lighting where half the image was underexposed in shadow, and half the image was overexposed in bright sunlight. This also caused these images to be unfocused. Eight of the unaligned photographs were taken from the lowest standardized level on the tripod. These eight photographs had consistently irregular shading with half the scene dark and half in light. In most of the photographs, the foreground is also unfocused, which is where the scales and reference data were, and in one of the photographs, there is visible debris on top of the scaled target. The rest of the unaligned photographs (26 photos) are ones that were taken close to the subject material with the handheld method. These photographs tend to be overexposed with next to no reference scales or targets in them because they are so close to the subject material. When a scale or target is visible, they appear blurry or overexposed. Because many of these photographs were taken at acute angles, there also tends to be grass obstructing the smaller bones.

The total field photograph collection time for this model was 58 minutes. The processing of the 3D model in Agisoft Metashape took the bulk of the time for this research, with the total processing time of 160.04 hours (see Table 5 for more details). The resulting model had an

RMSE value of .315 pix and a total scale error of .000312, both values that shows this is an accurate, scaled model. The final processing report (Appendix A) shows much more detail about the resulting 3D model, including the survey statistics and processing parameters used.

Visual Analysis of Model 4

An overview screenshot of the model (Figure 44) shows an accurate rendering of the scene. Model 4 shows the shape, size, and element of the bones, including the smaller bones that were laid out, such as the manubrium, the patella, and the calcaneus. The exact location and contour of the clothing can be seen, including areas where the clothing interacts and interferes with the bone surface. The bottom surface of grass can be seen throughout the scene, and in areas where they are present, individual leaves and twigs can be distinguished as well as individual tufts of grass. There is excellent contrast between the ground surface and the subject material, but in a few places, there are areas where the interface of the ground surface and the object is slightly blurred but still distinguishable. All the scales are visible, show no visual distortions, and clearly mark the boundaries of the scene.

While there are few visual errors seen in the overall view, there are some errors that become visible when the model is zoomed in. Side-by-side comparison of the textured model and the geometry show errors in the geometry of the objects. Most specifically, these distortions appear in areas where the object being modeled is thin and around the edges of larger objects.



Figure 44. Overall screenshot of Model 4

Figure 45 shows zoomed-in screenshots of both the texture and the geometry of the model in an area that involves the cranium, the mandible, the sternum (manubrium and body), and a hat. The most obvious errors present in these screenshots is the misrendered geometry on the right ascending ramus of the mandible. This thin protrusion of bone appears to have been partially present in the geometry screenshot, however, in the texture screenshot, little of this section is present. There are also subject-subject interfacing errors in the area of the sternum. While viewing the screenshot of the texture, the manubrium and the body of the sternum are two distinct bones that are also distinct from the ground surface and shirt; however, the geometry has

melled all these aspects together. There are interfacing issues between the ground surface and the shirt, between the ground-shirt surface and the bones, and between the two bones themselves.



Figure 45. Zoomed in screenshots of Model 4 showing both the textured (top) and mesh (bottom) models. The oval shows the subject-subject interface issue connecting the manubrium and the body of the sternum, and the arrow shows the misrendered geometry on the right ascending ramus of the mandible.

Figure 46 shows a slightly zoomed-in overhead shot of the torso area. The left ribs have areas of visual distortion along the shaft while the right ribs show poor subject-subject interface. There are more areas of subject-subject interface between the right scapula, humeral head, and the material of the shirt, as well as in the area of the lower thoracic vertebrae and the shirt

material. An oblique view of this same area shows the misrendered geometry in the area of the ischiopubic ramus of the right os coxa (Figure 47).



Figure 46. Overhead screenshot of Model 4 in both the textured (top) and mesh (bottom) models. The left arrow shows an area of poor subject-subject interface between two right ribs, and the right arrow shows an area with visual distortion of the texture in the area of the left ribs. The ovals show areas of poor subject-subject interface.



Figure 47. Oblique screenshot of the pelvis region of Model 4 showing both the textured (top) and mesh (bottom) models. The arrow is pointing at the misrendered geometry on the ischiopubic ramus of the right os coxa.

Figure 48 shows a slightly zoomed-in region of the lower limbs, including the femora, tibiae, fibulae, the right radius and ulna, and the right calcaneus, the lower portion of the shorts and both left and right shoes. In this view, there are a few areas of visual distortion, including on the right femur, and the subject-subject interface between the distal left tibia and fibula. On the right femur, the shaft appears to have been slightly misrendered. This error is based on a comparison between the object in the real world and the recreation in the model. In both the geometry and textured screenshots of the model, the circumference of the shaft appears much thinner relative to the ends of the long bone than the bone appears in real life. The shaft of the

right femur can also be compared to that of the left femur (which are relatively equal in real life), and the right femur is significantly thinner than the left in the model. These visual distortions in the screenshots are summarized and can be compared with those of other models in Table 6.

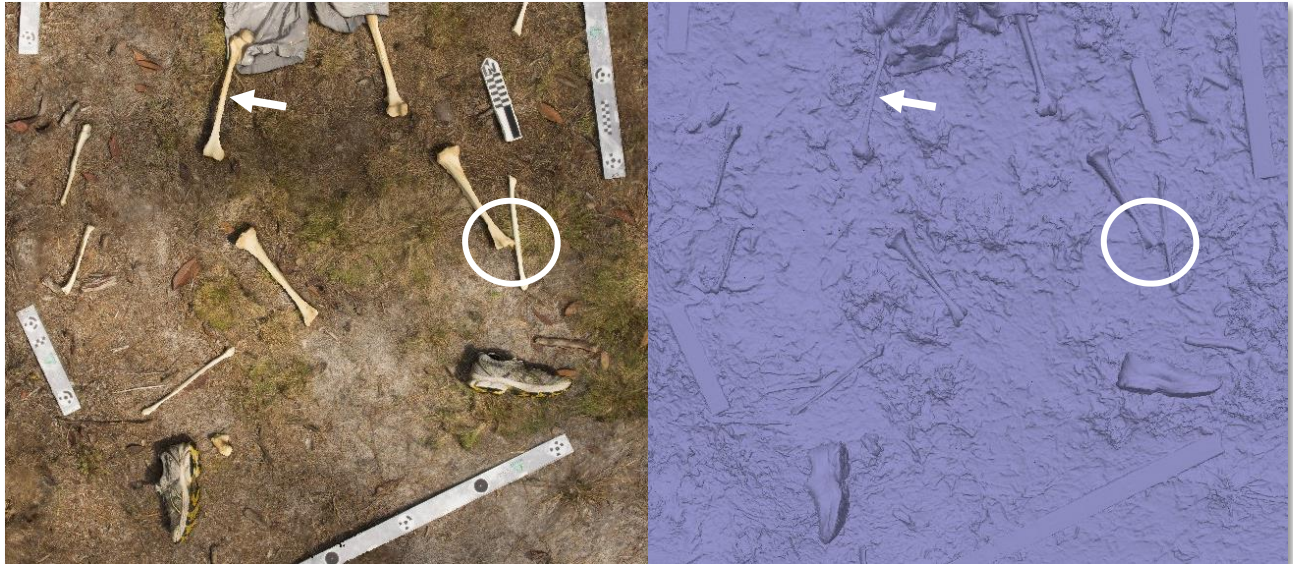


Figure 48. Slightly zoomed in overhead screenshot of the lower legs of Model 4 showing both the textured (left) and mesh (right) models. The arrow shows the misrendered geometry in the right femoral shaft and the oval shows the subject-subject interface error between the distal left tibia and the left fibula shaft.

Viewing the orthomosaic (Figure 49) of the model fills in some holes that are discussed above, but also adds different problems. While the screenshot overview (Figure 44) shows some issues with dappled shadows, this issue is made more evident in the orthophoto, where many of the shadows seen around the edges of the model were made by the researcher taking the photographs around the scene. Also present in the orthophoto are the feet of the researchers taking the photos in the upper left corner of the picture. In this same area, there is also a scale that is entirely present in the model and screenshots but is half missing in the orthophoto. After creating this orthophoto, the photographs were re-examined, and those photographs that showed the researcher's feet, and significant shadow errors were removed. The remaining photographs

were used to create a much better orthophoto (Figure 50) for this model. This new orthophoto also fixed the remaining problems with the scale distortion and much of the blurriness around the edges of the scene that was present in the first orthophoto. From this photograph, the hole filling function of the orthophoto appears to have filled in almost all the issues created in the geometry, especially in the areas of the ribs. The interfacing between the ground surface and the subject matter is also much improved from the screenshots, and all areas can be delineated from each other.



Figure 49. First overall orthophoto of Model 4 showing issues in the orthorectification process in the feet in the upper left corner and the distorted scales in the same area.



Figure 50. Second orthophoto generated for Model 4 by manually inspecting and removing photographs from the program. This orthophoto shows improvement in the shadows over the scene as well as the removal of the scale distortion and the feet of the researchers.

Model 5 – Mixed surface dominated with pine needles

Model 5 generation parameters

For this model, 222 photographs of the scene were taken. During the entire process of model creation, 73 photographs were removed, and the final model was created using 148 photographs. Twenty-eight photographs were removed during the sparse point cloud generation step. Twenty-four of these images were removed from the bottom look angle level and the close-up handheld images by not aligning in the photograph alignment procedure. The remaining four photographs were then removed during the estimation of the image quality process. In this case,

all four images were removed because they were out of focus in general. Fourteen of the remaining photographs were removed during the optimization of the sparse point cloud because they had less than 100 projections. The remaining thirty-one photographs were removed to create the texture and orthomosaic models. These photographs were removed because of lighting inconsistencies as well as moving shadows that were created from the researchers moving around the scene during data collection.

The total time it took to collect the photographs for this model was 29 minutes. The processing of the 3D model in Agisoft Metashape took the bulk of the time for this research, with the total processing time taking 23.08 hours (see Table 5 for more details). The resulting model had an RMSE value of .661 pix and a total scale bar error of .000268, both values that shows this is an accurate, scaled model. The final processing report (Appendix A) shows much more detail about the resulting 3D model, including the survey statistics and processing parameters used.

Visual Analysis of Model 5

An overview screenshot of the model (Figure 51) shows an accurate rendering of the scene. As with the last model, Model 5 shows the shape, size, and element of the bones, including the smaller bones that were laid out, such as the manubrium, the patella, and the calcaneus. The exact location and contour of the clothing can be seen, including areas where the clothing interacts and interferes with the bone surface. The bottom surface of grass can be seen throughout the scene, and in areas where they are present, individual leaves and twigs can be distinguished as well as individual tufts of grass. There is excellent contrast between the ground surface and the subject material, but in a few places, there are areas where the interface of the ground surface and the object is slightly blurred but still distinguishable. All the scales are clearly visible, show no visual distortions, and clearly mark the boundaries of the scene.



Figure 51. Overall screenshot of Model 5 showing accurate visual representation of the scene with little visual distortion.

Few visual errors are seen in the overall view. However, some errors become visible when the model is zoomed in. Side-by-side comparison of the textured model and the geometry show errors in the geometry of the objects.

Figure 52 shows slightly zoomed-in screenshots of both the texture and the mesh of the model in an area that involves the cranium, the mandible, the sternum (manubrium and body), some unserialiated cervical vertebrae, and a hat. The most obvious errors present in these screenshots is the misrendered geometry on the right ascending ramus of the mandible. This thin protrusion of bone appears to have been partially present in the geometry; however, in the texture, little of this section is present. There are also subject-subject interfacing errors between the manubrium and the sternal body and an area of poor ground surface-subject interface between the axis vertebra (cervical vertebra 2) and the ground surface.



Figure 52. Zoomed in screenshots of Model 5 showing both the textured (top) and mesh (bottom) models. The left arrow shows an area of misrendered geometry on the right ascending ramus of the mandible. The oval shows a subject-subject interfacing error between the manubrium and sternal body, and the right arrow shows ground surface-subject interface error between the axis and the ground surface.

Figure 53 shows a slightly zoomed-in overhead screenshot of the torso area. The superior angle of the right scapula shows an area of misrendered geometry where an artificial hole has been created. In the center of the screenshots, the area involving the unserriated lower vertebrae, the sacrum, left os coxa, and the pants shows poor subject-subject interface between all these objects of interest, as well as poor ground surface-subject interface. Also in this area, the geometry of the pants appears misrendered on top of the left os coxa. There is also another area

of poor subject-subject interface between the scale on the right of the screenshots and a left rib. In the oblique view (Figure 54), it is possible to see that some of the issues previously present are partially due to perspective. For example, from this angle, the ascending rami of the mandible are both present in the textured model as well as the geometry where in the overhead model, they appear to be misrendered. It is also possible to see other errors more clearly; for example, the ground surface-subject interface error between the cranium and the ground surface. From this angle, the aforementioned misrendered geometry is more apparent in the shorts over the left os coxa.

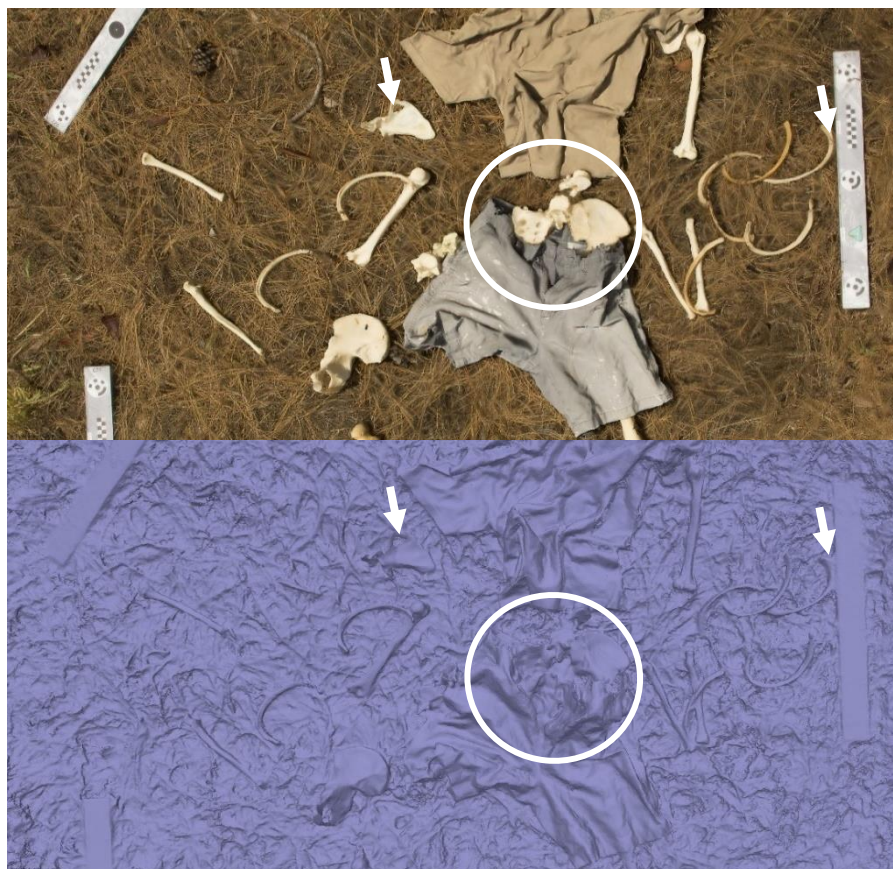


Figure 53. Overhead screenshot of Model 5 in both the textured (top) and mesh (bottom) models. The left arrow shows an area of misrendered geometry on the right scapula, the left arrow shows an area of poor subject-subject interface between a left rib and the scale, and the circle shows an area with poor subject-subject interface, poor ground surface-subject interface, and misrendered geometry.

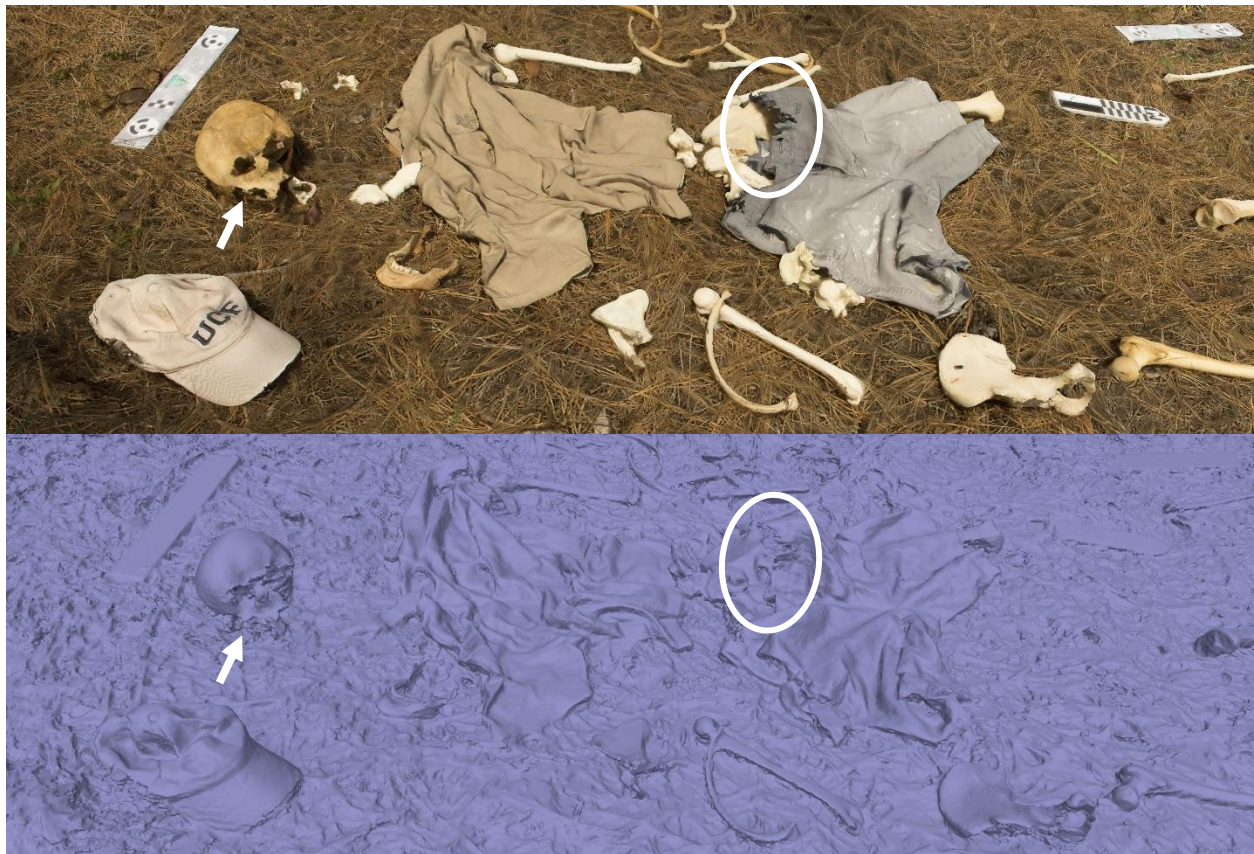


Figure 54. Oblique screenshots of Model 5 showing both the textured (top) and geometry (bottom) models. The oval indicates an area of misrendered geometry on the shorts on top of the left os coxa and the arrow is showing the poor ground surface-subject interface errors between the cranium and the ground surface.

Figure 55 shows a slightly zoomed-in region of the lower limbs, including the femora, tibiae, fibulae, and the right calcaneus, the lower portion of the shorts, and both left and right shoes. In this view, there are a few areas of misrendered geometry on the area of the left and right tibiae. These errors appear on the anterior crest of the left tibia, where the contour has been added on the midshaft of the anterior crest. On the right tibia, the bone appears compressed mediolaterally in the geometry of the model, and the texture appears distorted around the edges. There are also areas of interfacing error in the model. Specifically, in the area of the left femur,

there are errors in the geometry between the interface of the short leg. These visual distortions in the screenshots are summarized and can be compared with those of other models in Table 6.



Figure 55. Slightly zoomed in overhead screenshot of the lower legs of Model 5 showing both the textured (left) and mesh (right) models. The arrows show areas of slight misrendered geometry on the left and right tibiae and the oval indicates an area of subject-subject interfacing error between the left femur and pant leg.

As opposed to the previous model, there do not appear to be any major differences between the screenshot of the model (Figure 51) and the orthomosaic (Figure 56). This could be because extra photographs were removed before the texture and orthomosaic were created for this model. This model and orthophoto also had fewer issues with shadows present after removing photographs with significant shadows before processing the texture and the geometry.



Figure 56. Orthophoto of Model 5 showing little differences between the orthophoto and the screenshot of the model.

Model 6 – Mixed leaves and dirt

Model 6 generation parameters

For this model, 397 photographs of the scene were taken. During the creation of the final 3D model, 360 photographs were used. Of the 37 photographs that were not used in the model, 5 of the images were taken out during the image quality estimation, fifteen of the images were unaligned during the camera alignment phase of the process. These sixteen images were from the lowest look angle and from the additional close-up images that were taken. The remaining sixteen images were removed during the optimization of the sparse point cloud process due to less than 100 projections present in the photographs.

The total time it took to collect the photographs for this model was 34 minutes. The processing of the 3D model in Agisoft Metashape took the bulk of the time for this research, with the total processing time taking a little over six days (see Table 5 for more details). The resulting

model had an RMSE value of .864 pix and a total scale bar error of .000362, both values that shows this is an accurate, scaled model. The final processing report (Appendix A) shows much more detail about the resulting 3D model, including the survey statistics and processing parameters used.

Visual Analysis of the Model

An overview screenshot of the model (Figure 57) shows an accurate rendering of the scene. As with the last model, Model 6 shows the shape, size, and element of the bones, including the smaller bones that were laid out, such as the manubrium, the patella, and the calcaneus. The exact location and contour of the clothing can be seen, including areas where the clothing interacts and interferes with the bone surface. The bottom surface of leaves can be seen throughout the scene. There is excellent contrast between the ground surface and the subject material. All the scales are clearly visible, show no visual distortions, and clearly mark the boundaries of the scene.



Figure 57. Overall screenshot of Model 6 showing accurate visual representation of the scene with little visual distortion.

Figure 58 shows slightly zoomed-in screenshots of both the texture and the mesh of the model in an area that involves the cranium, the manubrium, and sternal body, the atlas and axis (cervical vertebrae 1 and 2 respectively), three unserriated cervical vertebrae, one unserriated thoracic vertebra, part of the shirt, and a hat. There are not many visual errors present in this area of the model. The hat, cranium, manubrium, and sternal body appear distinct in both the textured and geometry layers. Even the contour of the shirt and the interface between the shirt and the ground surface appears distinct in the geometry model. The only slight errors can be seen with the ground surface-subject interface between some of the cervical vertebrae.



Figure 58. Zoomed in screenshots of Model 6 showing both the textured (left) and mesh (right) models. The arrows show the ground surface-subject interfacing errors between the cervical vertebrae and the ground surface.

Figure 59 shows a slightly zoomed-in overhead shot of the torso area including both scapulae, both humeri, the right radius and ulna, three unserriated left ribs, five unserriated right ribs, three unserriated thoracic vertebrae, one unserriated lumbar vertebra, the sacrum, both os coxae, and the mandible. In this section of the model, there are a few areas of subject-subject interfacing errors between the right humerus, the right sleeve of the shirt, and two right ribs. There is another area with poor subject-subject interface where a right rib is sitting on top of the ilium of the left os coxa. Finally, there is another area of poor subject-subject interface between the ilium of the right os coxa and the short leg. There is one area with ground surface-subject interface between the right scale and the ground surface.



Figure 59. Overhead screenshot of Model 6 in both the textured (left) and mesh (right) models. The ovals show areas of poor subject-subject interface between the right shirt sleeve, the right humerus, and a right rib (top), between a right rib and the left os coxa (center), and between the right os coxa and the short leg (bottom). The arrow shows an area of poor ground surface-subject interface between the scale and the ground surface.

Figure 60 shows an oblique view of the two previous sections of the model that were discussed. In this figure, some of the previous visual errors can still be seen, such as the errors around the right humerus and right rib and the shirt, as well as the right os coxa and the short leg.

However, some new errors can be seen from this oblique angle, such as the interfacing between the right scapula and the shirt where the glenoid fossa and acromial process of the scapula appear fused with the material of the shirt. There is an area of misrendered geometry on the ischiopubic ramus of the left os coxa. Despite these errors, areas that were not appropriately modeled in previous models, such as the facial area of the cranium and many of the ribs, appear to be accurate representations of the real-life scenario.

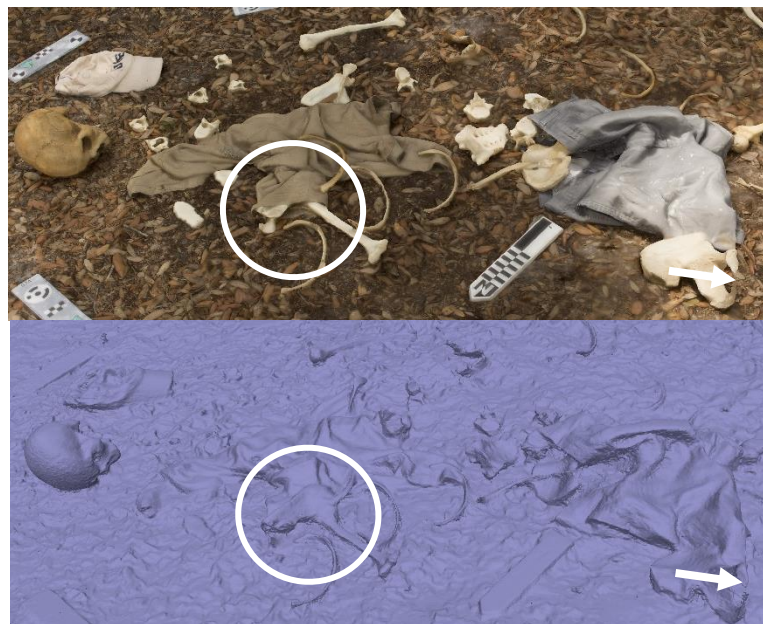


Figure 60. Slightly zoomed in oblique screenshots of the head and torso regions of Model 6 shown in both the textured (top) and geometry (bottom) models. The oval shows the area around the right humerus and scapula that show poor subject-subject interface. The arrow shows the misrendered geometry on the ischiopubic ramus of the right os coxa.

Figure 61 shows a slightly zoomed-in region of the lower limbs, including the femora, tibiae, fibulae, two unserriated left ribs, the left radius and ulna, and the right calcaneus, and both left and right shoes. In this area of the model, there are a few areas of ground surface-interface errors on the scale on the left and the scale on the top right of the screenshots. In the textured models on both scales, leaves are covering the scales, which causes an issue in the ground

surface interface with the scale bars in these areas. The main reason this is an issue is that when the scales were first placed, they were cleaned, so nothing was on top of them. This means that during the data collection process, the leaves were disturbed and were moved on top of the scale bars. There are areas of slightly misrendered geometry on the shafts of both left and right femora where the bones appear much thinner in diameter relative to what they look like in real life. These visual distortions in the screenshots are summarized and can be compared with those of other models in Table 6.



Figure 61. Slightly zoomed in overhead screenshot of the lower legs of Model 6 showing both the textured (left) and mesh (right) models. The arrows show areas of misrendered geometry on the left and right femora. The white boxes indicate areas where leaves have been moved to cover the scales during data collection, causing ground surface-interfacing errors around the scale bars.

Unlike viewing the orthomosaic (Figure 62) of the previous models, the orthomosaic of Model 6 provides more problems in the visualization of the model. While the screenshot overview above (Figure 58) shows some issues with dappled shadows, this issue is made more evident in the orthophoto, where inconsistent lighting is a prominent problem throughout the entire scene. Another problem present is the distortion of the scale bars. On the top left scale, the entire center of the scale appears displaced from the ends. There are also less obvious issues in

the scales, such as in the bottom center scale, where the edges do not appear straight but slightly wavy. This distortion is most likely due to the leaves moving in this area. In this orthophoto, it is also apparent that there are still problems with linear banding creating a double effect on some of the bones, mostly both radii and ulnae.

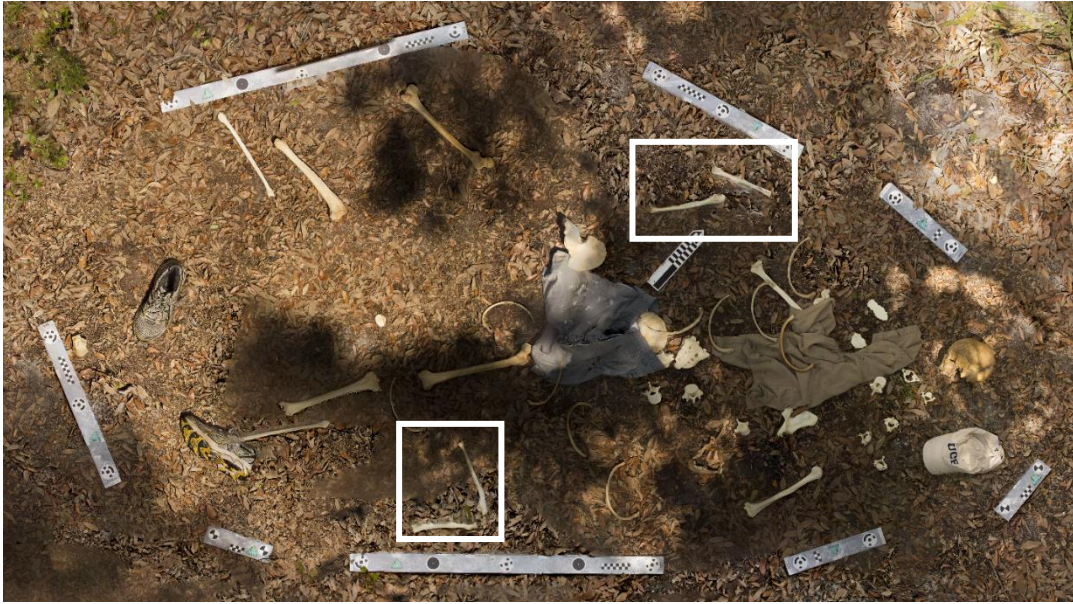


Figure 62. Overall orthophoto of Model 6 showing issues in the orthorectification process in the form of dappled shadows from inconsistent lighting, the distortion of scales on the upper left and bottom center scales, and bones that show linear banding causing a double image of the bones (boxes).

Table 5. Model generation times for chapter 3 models processed in Agisoft Metashape Professional (in hours)

Model #	Photograph Collection Time	Camera Align Time	Dense Point Cloud Generation	Mesh Generation	Texture Generation	Orthomosaic Generation	Total Time
4	.97	.38	157.02	.67	.7	.3	160.04
5	.48	.4	21.02	.48	.53	.17	23.08
6	.56	.8	142.33	.7	.82	.33	145.54

Table 6. Visual analysis from the screenshots – summary and comparison table.

Model	Bone Geometry	Clothing Geometry	Scale Geometry	Ground Surface-Subject Interface	Subject-Subject Interface
4	Thin bones (rami, ribs, etc.) tend to be rendered poorly	Generally good, some interfacing errors	Very slight modeling issues around the edges in some scales	Smaller bones (vertebrae, sternum, etc.) tend to blend into the geometry Some issues around the edge of clothing (bill of the hat)	Bones that are close to each other (sternal bones, fibula, and tibia, etc.) appear fused in geometry Bones interacting with clothing (scapula, vertebrae, etc.) are not differentiated in geometry
5	Thin bones (rami especially) are rendered poorly Ribs show better geometry than Model 4	Area on the shorts that were misrendered	Overall good, interfacing error with 1 rib close to the scale	Ground surface tends to fuse with the geometry around the edges of larger bones and fuse altogether with smaller bones	Bones close together tend to become connected in their geometry Bones interacting with shorts tend to be indistinguishable from them in the geometry
6	Thin areas (rami of os coxa and ribs) do not fuse all the way Right femur is compressed mediolaterally	Overall good, some interfacing errors	Some slight distortion around the edges (from leaves covering the scales)	Vertebrae indistinct from the ground surface	Small bones tend to fuse with the clothing geometry Larger bones that interact with the clothing tend to fuse to the geometry Two bones close to each other tend to fuse geometry together

Discussion

In the field of forensic science, the ability to document the context of outdoor scenes efficiently and with as little contamination as possible is of the utmost importance (Dirkmaat, 2012). The current methods of field documentation include tediously hand-drawn maps, written descriptions of locations, and reductive 2-dimensional photography, all of which do not capture the entire context of the complex 3D scene. In addition to this, hand-drawn maps require measurements to be taken, which can move objects within the crime scene and change the contextual position, no matter how careful the documenter is being. Close-range 3D digital photogrammetry offers a fast, low-cost alternative that uses photography equipment already owned by local law enforcement departments and does not require any interaction with the scene to complete the 3D model so the context will be preserved.

This method of context documentation has already been used for years to document many aspects of archaeological excavations. However, in the field of forensics, the applications have been limited. The following sections will discuss the issues faced, as well as detailing the best practices found during this research with regards to data collection methods, the scene size and ground surface, and the efforts taken to reduce visual error in the resulting 3D models.

Data collection methods

Based on the analysis of these three models, there does not appear to be any significant visual advantage to using one technique over another. This lack of significance may be due to the difficulty of attributing the visible results to one of two different manipulated variables (ground surface or the data collection technique). However, there was a major difference between the techniques in the maneuverability of the camera and the time it takes to collect the images.

Three different photographic methods were used to collect the field data for this research. Data for Model 4 was collected using a tripod, data for Model 5 was collected using a monopod, and data for Model 6 was collected using the handheld technique. Each of these methods provided both advantages as well as disadvantages for the data collection process. The tripod created the most standardized and stable look angles around the scene but did not provide much flexibility when it comes to taking photographs at different angles from a single spot. It was also discovered that a tripod could be cumbersome to move, especially in an area with obstructions such as hills or vegetation around the perimeter of the scene. The monopod also provided relatively standardized look angles but was able to provide more flexibility to capture different angles from a single position. However, using this method can still be somewhat difficult to capture photographs around obstacles and to maneuver the pole around and through thick vegetation. Finally, the handheld technique provides less standardization of the look angles because it relies on the subjective estimation of standardized levels, but it does provide much more flexibility. With this flexibility comes the ability to capture images from different angles and to move around objects with relative ease.

With the tripod, 380 images were collected, taking 58 minutes to complete, while with the handheld technique, 397 images were collected, taking 34 minutes to complete. The combination of the maneuverability and the data collection time would be the factors to consider when choosing a data collection technique. If the terrain and time constraints are limiting, as with most forensic scene investigations, the handheld technique would most likely be the best option. With all the techniques, there is the possibility of moving the ground material, and in some cases, the scales were obscured by leaf and pine needle material that had been moved. This movement of the ground surface tended to happen more when the tripod was used and being

dragged over the ground surface. It also happened when the handheld technique was used, and the researcher was not paying careful attention.

Camera Settings, Scene Lighting, and Number of Images

For all three models, the images were taken in aperture priority setting, which is a semi-automatic setting that allows the researcher to select the depth of field for the photographs while the camera controls all other aspects. This setting was chosen because it is important to make sure the foreground and the background of the photographs are in focus. This setting is also supposed to be useful in situations where there is a large amount of light or a small amount of light so that the aperture will stay stable and the other settings are adjusted. However, it was found that in photographs that had dappled and inconsistent shadows around the scene, the photographs still appeared inconsistently lit. If the image was taken from the shadows, the lighted areas appeared overexposed and unfocused, and when taken from the bright side, the shaded area was underexposed and unfocused. The fact that the shutter speed was adjusted based on the lighting conditions also appears to have caused some issues with camera shake when the photographs were taken from the shaded side of the scene using the handheld technique in Model 6. This caused some problems in the textures and the orthophotos that made it appear like the areas covered in shadow were out of focus. These photographs had to be manually removed from the program to create shaded areas that were in focus.

Some of these photography problems are difficult to solve without choosing an overcast day or a time of day to document the scene when there is consistent lighting. One other option that has been used is setting up a tent or other structure to block the sun over the scene. Realistically though, in the field of forensics, there is rarely time to wait for the lighting to be perfect or to construct a structure to block the light. Even using the fully automatic settings on

the camera (see the models in Chapter 2), these problems still occur. However, by manually inspecting and removing images that have these lighting inconsistency issues before the texture and orthophoto are created, these visual errors can be mitigated in the final model reconstruction of the scene.

In cases such as these, where it is expected that images will be removed, it is important to collect more images than what is strictly necessary to ensure that the final model will be complete. This is also a suggestion given in the Agisoft Metashape Professional user manual (2019). When comparing the three models used in this chapter, there does not appear to be a major difference between the visual analysis of Models 4 and 6, that started with well over three hundred images each, and Model 5 that started with a little over two hundred photographs. According to previous research (Agisoft, 2019; Douglass et al., 2015; Gidusko, 2018), the photographs should be from at least three different look angles with at least a 2/3 overlap of the photographs. In general, it is also acknowledged that the more points the photographs have in common, the better the final model will turn out (Gidusko, 2018). For this research, the use of five or more look angles with overhead and photographs and close-up photographs of areas of interest were used to help maximize coverage of the scenes. Because of this coverage, multiple images from each model were able to be removed without affecting the overall quality of the 3D model. Even though the close-up photographs were the photographs most likely to be excluded from the model during the camera alignment process, they are still useful for photographic documentation of the crime scene. It was also determined in preliminary research that overhead photography will always be necessary to create an accurate orthophoto of the scene because it needs the overhead view to create an overhead orthomosaic. This type of coverage during data

collection is highly recommended for any documentation of forensic scenes using photogrammetry.

Scene Size and Ground Surface

The size of the scene will always be positively correlated with the data collection time, the number of photographs needed to maintain photographic coverage, and the time it takes to process the models in the Agisoft Metashape software. The scenes used in this research were limited in size because of this fact and were not large enough to significantly affect the data collection or processing time.

The complexity of the ground surface has been cited as being one variable that can influence the final model generation times and final model quality (Gidusko, 2018). In Gidusko's (2018) research, the complexity of a ground surface dominated by leaves and a ground surface dominated by grass was compared with the clean ground surface of a mock forensic excavation. In this case, the model generation time was significantly increased when processing the complex (grass and leaves) ground surface as opposed to the simple ground surface (excavation).

For the current research, all the scenes were chosen because of the complicated geometry present on the different ground surface. The ground surface geometry of Model 4 was dominated by grass, the ground surface of Model 5 was dominated by pine needles, and the ground surface of Model 6 was dominated by leaves. For this analysis, Model 5 was removed because the number of photographs used in the final model (n=148) was not comparable to the number of photographs used in Models 4 and 6 (n=343 and 360, respectively). Both of these scenes were constructed in roughly the same manner and were approximately the same size (3.5m by 2m). Model 4 had a total processing time of 160.04 hours, and Model 6 took a total of 145.54 hours to

complete. Neither of these data shows major differences, and in both cases, the model produced was accurate and accurately scaled. Between two different models with complex ground surfaces, there does not appear to be a significant impact on the final model processing time .

Reducing visual errors

As shown in the results section above, the overall screenshots of the 3D models tend to accurately represent the spatial layout and context of the scene with little visual distortion present. It is only when the image is zoomed in that significant visual distortions are revealed in both the textured model and in the underlying geometry of the model. The main factor that introduces error into the texture has already been discussed in the above section discussing lighting and shadows. However, most of the errors seen in the results section; the interfacing errors between the ground surface and the bones, interfacing errors between bones and other objects of interest (i.e., other bones or clothing), and issues in the rendering of the geometry of objects; come from the mesh layer of the model, or the geometry itself. In many of these cases, the error present is covered up or masked by the texture layer. In cases like this, the color changes in the texture can make the model appear cleaner than just looking at the uniformly colored geometry of the model. Therefore, both textured and geometry screenshots were analyzed to see where the problem in the model originated.

The added step of visually inspecting and manually removing images with visual errors due to shadows and other lighting issues resolved most of the problems present that came from the texture of the model. Removing the photographs that were out of focus also resolved many interfacing errors between objects as well. This is because the more in focus an image is, the less noise and visual error it will produce in the 3D model (Agisoft, 2019). The remaining small amount of errors may be due to any number of factors including a slightly too high ISO and a

slightly too slow shutter speed that make the photograph just the tiniest bit out of focus, the fact that bone tends to be uniformly colored with flat, smooth-looking surfaces, and also moving objects around the scene (Agisoft, 2019).

In most cases, imperceptibly unfocused images and the general nature of bones to be flat and smooth cannot be helped; however, measures can be taken to reduce the movement of objects around the scene. Before the photograph collection begins, the scene should be cleaned of any extra vegetation around the area to be photographed. This clearing of vegetation serves to create a surface that is easier to get photographs from the ground level but also reduces the chances of this vegetation moving due to factors like wind and rain. During this process, a buffer area around the defined limits of the scene should also be cleared. The exact size of this area can depend on the data collection method being used. For example, if using a tripod, more room will be needed to move around the scene than if using the handheld technique. This buffer area serves multiple purposes, to allow for easy access to all areas around the scene, to be able to capture the scales in all look angle levels, and to reduce the amount of debris that is placed on the scale by the researcher moving around the scene. After this area has been cleared and the data collection has begun, it is important to take care not to push debris on top of the scales. If the coded targets present on the scales become covered by debris (e.g., pine needles or leaves), it is possible that the target will not be registered in the program and could affect the alignment of the photograph, or it could just cause more ground surface-scale interfacing error as was the case in Model 6 where leaves were pushed on top of the scales in multiple places.

Because of all the factors that can never be controlled for, especially at an outdoor scene, it is essential to keep in mind that no photogrammetry model will ever be completely perfect. However, using the techniques and guidelines present in previous research and building upon

previous research with trial-and-error processing techniques, it is possible to limit and reduce the errors seen in the final 3D models. It is also important to acknowledge that zooming in close to a 3D model to find these minuscule flaws in the geometry is an entirely unrealistic venture that provides no real valuable information about the 3D model. Just like zooming too far into a photograph makes the image pixilated and useless, zooming too far into a 3D model can significantly distort what the model is meant to represent. In this case, the purpose was to assess the applicability of using photogrammetry to create 3D models of outdoor mock forensic crime scenes involving the limited scattering of real human remains that accurately shows the spatial layout and context of the scene. This research has determined that photogrammetry can be a useful and powerful addition to the traditional techniques of forensic crime scene documentation and should be used to document forensic crime scenes.

Conclusion

Three mock forensic crime scenes with complex ground surface geometry and limited scatter of human skeletal material were created to test the capability of terrestrial CRP for the documentation of outdoor forensic crime scenes. The results of this research demonstrate that CRP can be used to document the 3D context of these scenes accurately and can be easily integrated into the data collection protocol at outdoor crime scenes. There are some limitations to this technique, as with all methods used to survey. These include the cost of computers, the cost of the software, and the time needed to run these complex 3D models. However, if less time is taken at the scene to measure and hand draw maps, time in the field can be minimized, and processing of the scene can commence without destruction of evidence.

Future research should be focused on increasing the complexity of the scenes documented to better represent and eventually document real forensic crime scenes. The

situations present in real forensic crime scenes are much more complex and varied than the scenarios present in controlled mock environments, so further data collection and processing parameters should be explored. Along with this, exploring better processing procedures in Agisoft Metashape Profession should be another area of focus. This should include processing models multiple times to refine processing methods. Processing models multiple times can also help obtain a more accurate data processing time by averaging the time of multiple iterations. Other processing tools should also be tested. These include those that have the potential to eliminate or reduce the effects of shadows and other blending and color correction programs to reduce error and create a more accurate visualization of the scenes that are documented (Agisoft, 2019). These programs and applications should be explored in the context of forensic scene documentation.

CRP has already been and continues to be used extensively in multiple fields of study, including the documentation of outdoor archaeological scenes. As the technology required to create accurate and complex 3D models becomes more advanced and inexpensive, it seems reasonable to conclude the use of the technology will become more accessible to the field of forensic science. This data collection process of taking photographs is much faster and potentially more reliable than traditional mapping techniques of forensic crime scenes and uses digital camera technology that is already accessible in every crime scene investigation department nationwide. This research builds on previous research to show the applicability of CRP and to further refine the methodology of applying CRP to forensic crime scenes accurately and with scientific replicability.

CHAPTER FOUR: DISCUSSION AND CONCLUSION

Close-range photogrammetry (CRP) has already been and continues to be used extensively in multiple fields of study, including the documentation of archaeological scenes (e.g., Garstki et al., 2018; Howland et al., 2018; Jalandoni et al., 2018; Jones and Church, 2020; Novotny, 2019; Pierdicca, 2018). As the technology required to create accurate and complex 3D models becomes more advanced and inexpensive, it seems reasonable to conclude the use of the technology will become more accessible to the field of forensic science. This data collection process of taking photographs and creating a 3D model is much faster and potentially more reliable than traditional mapping techniques of forensic crime scenes. Photogrammetry uses simple digital camera technology that is already accessible in every crime scene investigation department nationwide (Connor, 2007:32; Dupras et al., 2012:7; Robinson, 2012). Furthermore, data collection for CRP need not be handled by the forensic archaeologist, as any law enforcement official may be trained to collect photographs correctly.

Documentation of a forensic scene using these methods would only minimally impact the time needed for data collection, and the photographs can be archived and processed at a later date if a 3D model is needed. While this research is still preliminary and further research will be needed to set a precedence for its inclusion into the forensic archaeological methodology, CRP has the potential to expand traditional crime scene documentation methods, and possibly even replace them in the future.

There are still confounding variables that need to be considered, such as weather conditions, software cost, and data processing time, however, these variables do not entirely prohibit the use of CRP in the field. Weather conditions can be mitigated by commonplace equipment such as a tent overhead. This use of a tent is a technique commonly used in archaeology to protect the archaeological sites (e.g., Forte, 2014). Much experimental 3D

documentation of forensic crime scenes to date (e.g., Holowoko et al., 2016; Komar et al., 2012) used laser scanning technology to document the scene. This laser scanning technology is significantly more expensive than photogrammetry software and requires more equipment and data collection training than CRP does (Table 7). Data processing time presents less of an issue than the other two variables. It may take many hours to complete a 3D model based on the hardware processing capabilities, but setting up a batch process in Agisoft Metashape Professional allows the ability to begin processing and then leave the computer to process the model. This automation gives the researcher time to complete other tasks while the model is completed.

Table 7. Summary of some laser scanning and photogrammetry technologies and their cost.

3D modeler/software	Laser scanner/photogrammetry	Cost	Resource
Leica ScanStation P40	Laser Scanner	\$123,945	FLT Geosystems, 2020
Leica ScanStation P50	Laser Scanner	\$120,000	FLT Geosystems, 2020
Leica RTC360	Laser Scanner	\$78,036	FLT Geosystems, 2020
Agisoft Metashape Pro.	Photogrammetry	\$3499	Von Ubel, 2020
Agisoft Metashape Standard	Photogrammetry	\$179	Von Ubel, 2020
3DF Zephyr	Photogrammetry	€149	Von Ubel, 2020
Autodesk ReCap	Photogrammetry	\$40/month	Von Ubel, 2020

Building upon research that has been recently undertaken (Urbanova, 2017; Gidusko, 2018), this research limited the parameters of what was being tested (outdoor scatter scenes documented with CRP techniques) and used real human skeletal material to create the 3D models. The models created during this research showed high accuracy (RMSE scores of <1, scale bar error <.001) with some small qualitative visual errors seen when the model is zoomed-

in. In general, this research found that the more photographs collected, the least amount of qualitative visual error was present in the resulting 3D model. Also, the more complex the ground surface of the scene is, the more photographs are needed, and the 3D model will take longer to process.

Further research should focus on expanding the application of CRP to document scenes with complicated contexts and scenarios and testing the capability of CRP to document these scenarios. These should include several other environmental settings, more extensive scatter scenarios, and scenarios where the remains are not as readily accessible for documentation (i.e., obstructed scenes). Attempts should be made to isolate and control for variables that introduce qualitative visual error into the resulting 3D model. Refining data processing procedures and exploring the more advanced features in Agisoft Metashape Professional should also be undertaken. Refining data processing procedures would involve processing models multiple times to reduce the quantitative and qualitative errors that are presented in this thesis. For future applications in the field of forensic science, reduction of the quantitative errors may be more important than small qualitative errors seen. Extra advanced features that should be explored include shadow correcting algorithms, blending and color-correcting programs, and other advanced applications that can help create a more accurate visualization of the 3D model and to reduce the qualitative visual errors seen (Agisoft, 2019). Finally, future research should always seek to further refine data collection practices in order to create the most accurate and efficient methodology for the use of CRP in forensic archaeology.

APPENDIX A: PROCESSING REPORTS

MODEL 1 PROCESSING REPORT

Agisoft Metashape

**Processing Report
11 October 2019**



Survey Data

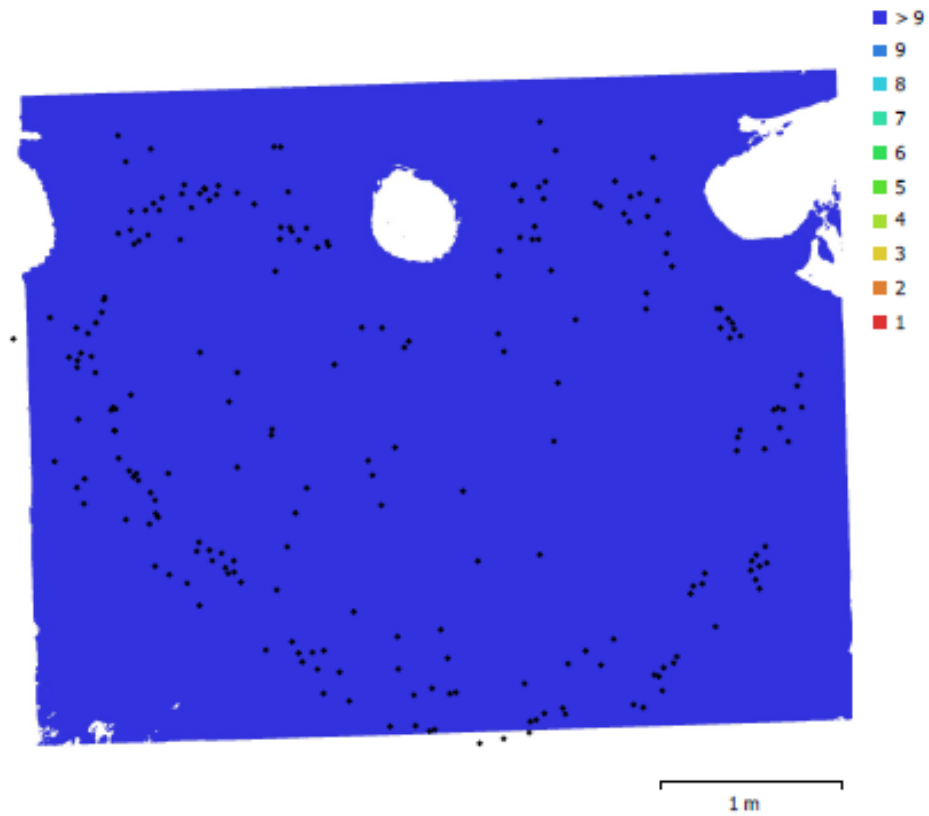


Fig. 1. Camera locations and image overlap.

Number of images:	223	Camera stations:	223
Flying altitude:	1.78 m	Tie points:	313,178
Ground resolution:	0.387 mm/pix	Projections:	824,541
Coverage area:	15.7 m ²	Reprojection error:	0.528 pix

Camera Model	Resolution	Focal Length	Pixel Size	Precalibrated
NIKON D7200 (18mm)	6000 x 4000	18 mm	3.91 x 3.91 μ m	No

Table 1. Cameras.

Camera Calibration

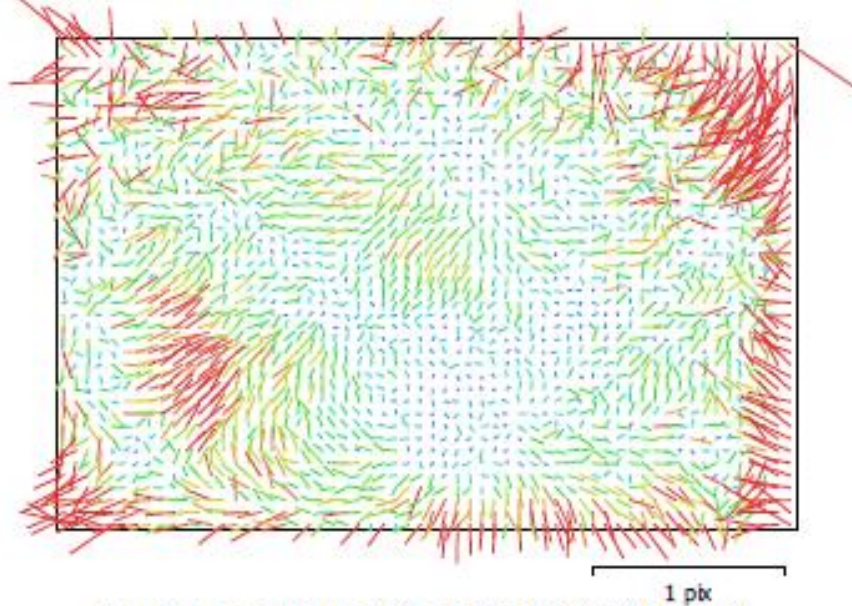


Fig. 2. Image residuals for NIKON D7200 (18mm).

NIKON D7200 (18mm)

223 images

Type	Resolution	Focal Length	Pixel Size
Frame	6000 x 4000	18 mm	3.91 x 3.91 μm
F:	4703.03		
Cx:	-0.504484	B1:	0
Cy:	-10.1795	B2:	0
K1:	-0.151596	P1:	0.000543549
K2:	0.110131	P2:	0.000392242
K3:	-0.00371101	P3:	0
K4:	0	P4:	0

Scale Bars

Label	Distance (m)	Error (m)
target 49_target 50	0.500047	0.000157041
target 50_target 51	0.50002	0.000920333
target 55_target 56	0.249955	-4.53909e-005
target 57_target 58	0.499577	-0.000492853
target 58_target 59	0.499618	-0.000411973
target 60_target 61	0.249828	-0.000161644
target 61_target 62	0.249931	-0.000139386
Total		0.000436204

Table 2. Control scale bars.

Digital Elevation Model

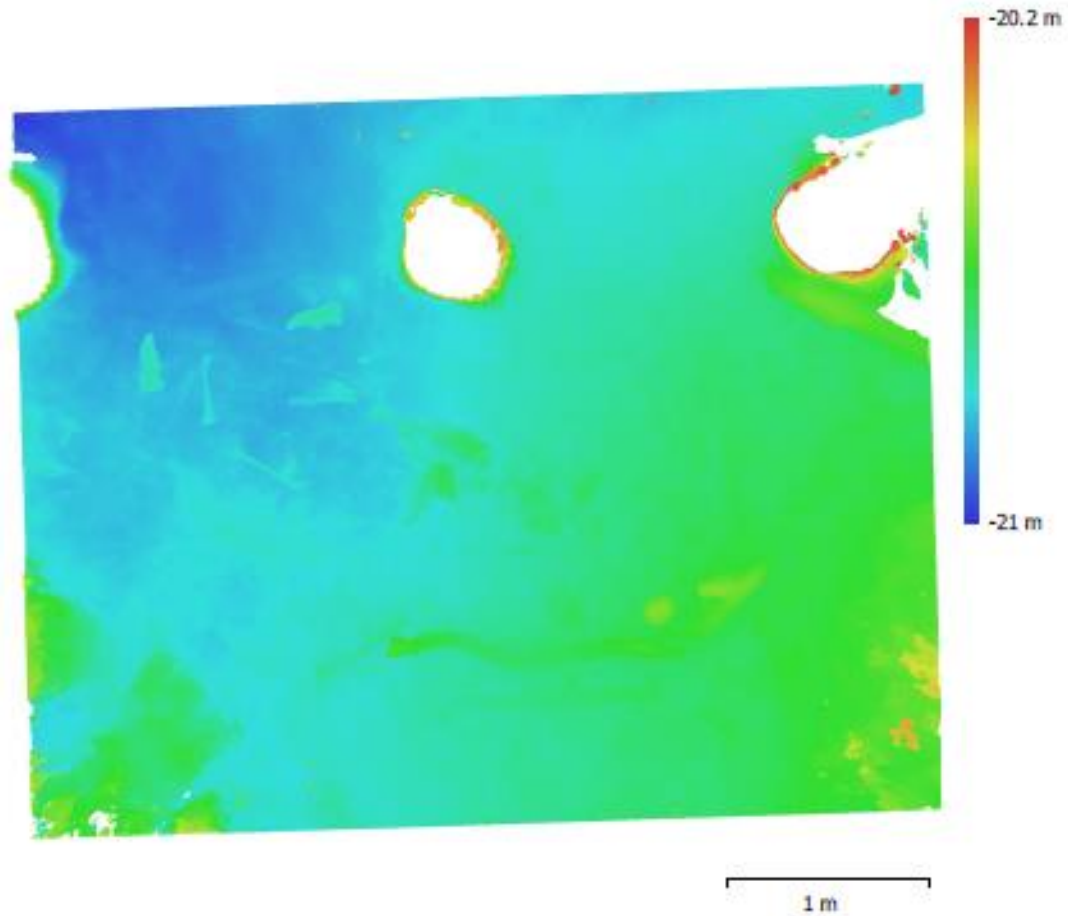


Fig. 3. Reconstructed digital elevation model.

Resolution: 0.773 mm/pix
Point density: 1.67 points/mm²

Processing Parameters

General

Cameras	223
Aligned cameras	223
Markers	16
Scale bars	9
Coordinate system	Local Coordinates (m)
Rotation angles	Yaw, Pitch, Roll

Point Cloud

Points	313,178 of 1,109,082
RMS reprojection error	0.19787 (0.52761 pix)
Max reprojection error	5.90384 (20.9696 pix)
Mean key point size	2.60699 pix
Point colors	3 bands, uint8
Key points	No
Average tie point multiplicity	2.68117

Alignment parameters

Accuracy	High
Generic preselection	Yes
Key point limit	60,000
Tie point limit	0
Adaptive camera model fitting	No
Matching time	13 minutes 37 seconds
Alignment time	9 minutes 37 seconds

Optimization parameters

Parameters	f, cx, cy, k1-k3, p1, p2
Adaptive camera model fitting	No
Optimization time	10 seconds

Depth Maps

Count	223
Reconstruction parameters	
Quality	High
Filtering mode	Mild
Processing time	2 hours 54 minutes

Dense Point Cloud

Points	42,826,065
Point colors	3 bands, uint8
Reconstruction parameters	
Quality	High
Depth filtering	Mild
Depth maps generation time	2 hours 54 minutes
Dense cloud generation time	1 days 6 hours

Model

Faces	8,565,008
Vertices	4,298,336
Vertex colors	3 bands, uint8
Texture	8,192 x 8,192, 4 bands, uint8
Reconstruction parameters	
Surface type	Arbitrary
Source data	Dense
Interpolation	Enabled

General	
Quality	High
Depth filtering	Mild
Face count	8,565,008
Processing time	35 minutes 50 seconds
Texturing parameters	
Mapping mode	Generic
Blending mode	Mosaic
Texture size	8,192 x 8,192
Enable hole filling	Yes
Enable ghosting filter	Yes
UV mapping time	3 minutes 41 seconds
Blending time	35 minutes 24 seconds
Orthomosaic	
Size	11,899 x 9,643
Coordinate system	Local Coordinates (m)
Colors	3 bands, uint8
Reconstruction parameters	
Blending mode	Mosaic
Surface	Mesh
Enable hole filling	Yes
Processing time	15 minutes 15 seconds
Software	
Version	1.5.1 build 7618
Platform	Windows 64

MODEL 2 PROCESSING REPORT

Agisoft Metashape

**Processing Report
11 October 2019**



Survey Data



Fig. 1. Camera locations and image overlap.

Number of images:	250	Camera stations:	250
Flying altitude:	1.57 m	Tie points:	329,164
Ground resolution:	0.346 mm/pix	Projections:	821,142
Coverage area:	13.9 m ²	Reprojection error:	0.421 pix

Camera Model	Resolution	Focal Length	Pixel Size	Precalibrated
NIKON D7200 (18mm)	6000 x 4000	18 mm	3.91 x 3.91 μm	No

Table 1. Cameras.

Camera Calibration

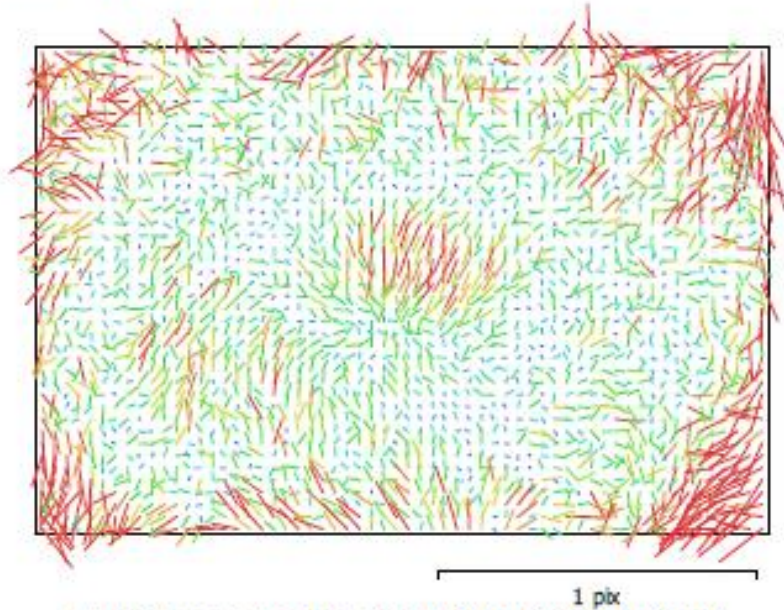


Fig. 2. Image residuals for NIKON D7200 (18mm).

NIKON D7200 (18mm)

250 images

Type Frame	Resolution 6000 x 4000	Focal Length 18 mm	Pixel Size 3.91 x 3.91 μm
F:	4699.27		
Cx:	-0.411667	B1:	-0.0287471
Cy:	-0.6936	B2:	0.178411
K1:	-0.149564	P1:	0.000464687
K2:	0.0982753	P2:	0.000632154
K3:	0.0174817	P3:	0.173092
K4:	-0.0147606	P4:	0.146438

Scale Bars

Label	Distance (m)	Error (m)
target 49_target 50	0.499733	-0.00015735
target 50_target 51	0.499797	0.000696616
target 52_target 53	0.24989	-6.01867e-005
target 53_target 54	0.250011	4.0768e-005
target 55_target 56	0.249798	-0.00020231
target 57_target 58	0.499933	-0.000136838
target 58_target 59	0.499767	-0.000263046
target 60_target 61	0.24998	-9.92389e-006
target 61_target 62	0.250023	-4.72718e-005
Total		0.000268017

Table 2. Control scale bars.

Digital Elevation Model

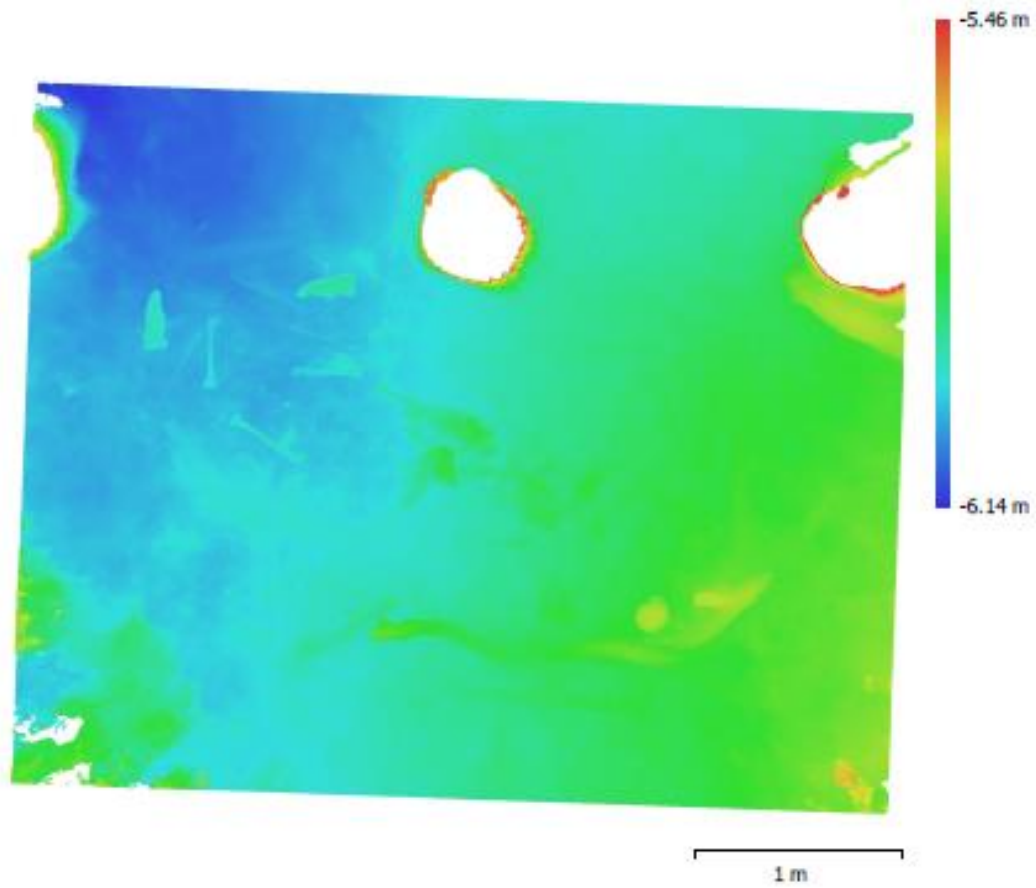


Fig. 3. Reconstructed digital elevation model.

Resolution: 0.692 mm/pix
Point density: 2.09 points/mm²

Processing Parameters

General

Cameras	250
Aligned cameras	250
Markers	16
Scale bars	9
Coordinate system	Local Coordinates (m)
Rotation angles	Yaw, Pitch, Roll

Point Cloud

Points	329,164 of 1,250,371
RMS reprojection error	0.142057 (0.421443 pix)
Max reprojection error	1.29386 (4.66589 pix)
Mean key point size	2.90285 pix
Point colors	3 bands, uint8
Key points	No
Average tie point multiplicity	2.76525

Alignment parameters

Accuracy	High
Generic preselection	Yes
Key point limit	60,000
Tie point limit	0
Adaptive camera model fitting	No
Matching time	26 minutes 44 seconds
Alignment time	9 minutes 54 seconds

Optimization parameters

Parameters	f, b1, b2, cx, cy, k1-k4, p1-p4
Adaptive camera model fitting	No
Optimization time	31 seconds

Depth Maps

Count	250
-------	-----

Reconstruction parameters

Quality	High
Filtering mode	Moderate
Processing time	2 hours 17 minutes

Dense Point Cloud

Points	48,858,514
Point colors	3 bands, uint8

Reconstruction parameters

Quality	High
Depth filtering	Moderate
Depth maps generation time	2 hours 17 minutes
Dense cloud generation time	1 days 11 hours

Model

Faces	9,771,555
Vertices	4,901,184
Vertex colors	3 bands, uint8
Texture	8,192 x 8,192, 4 bands, uint8

Reconstruction parameters

Surface type	Arbitrary
Source data	Dense
Interpolation	Enabled

General	
Quality	High
Depth filtering	Moderate
Face count	9,771,555
Processing time	43 minutes 51 seconds
Texturing parameters	
Mapping mode	Generic
Blending mode	Mosaic
Texture size	8,192 x 8,192
Enable hole filling	Yes
Enable ghosting filter	Yes
UV mapping time	3 minutes 49 seconds
Blending time	36 minutes 21 seconds
Orthomosaic	
Size	12,687 x 10,272
Coordinate system	Local Coordinates (m)
Colors	3 bands, uint8
Reconstruction parameters	
Blending mode	Mosaic
Surface	Mesh
Enable hole filling	Yes
Processing time	15 minutes 4 seconds
Software	
Version	1.5.1 build 7618
Platform	Windows 64

MODEL 3 PROCESSING REPORT

Agisoft Metashape

Processing Report

11 October 2019



Survey Data

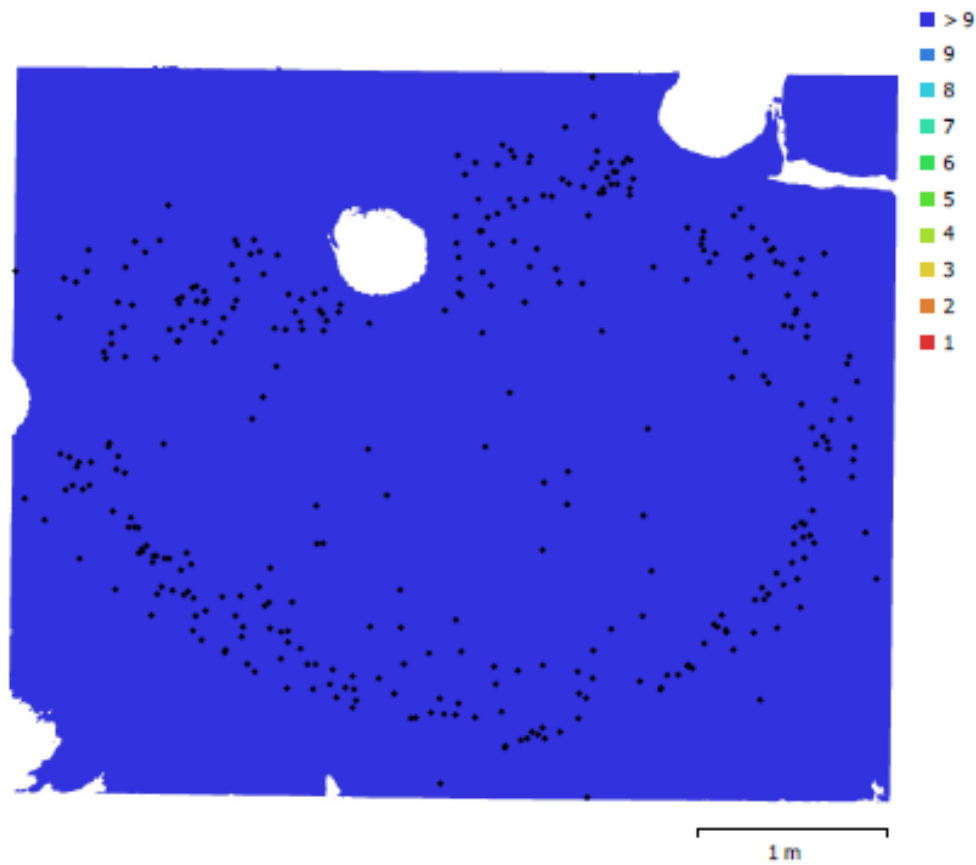


Fig. 1. Camera locations and image overlap.

Number of images:	363	Camera stations:	357
Flying altitude:	1.76 m	Tie points:	609,349
Ground resolution:	0.398 mm/pix	Projections:	1,578,307
Coverage area:	17.5 m ²	Reprojection error:	0.393 pix

Camera Model	Resolution	Focal Length	Pixel Size	Precalibrated
NIKON D7200 (18mm)	6000 x 4000	18 mm	3.91 x 3.91 μ m	No

Table 1. Cameras.

Camera Calibration

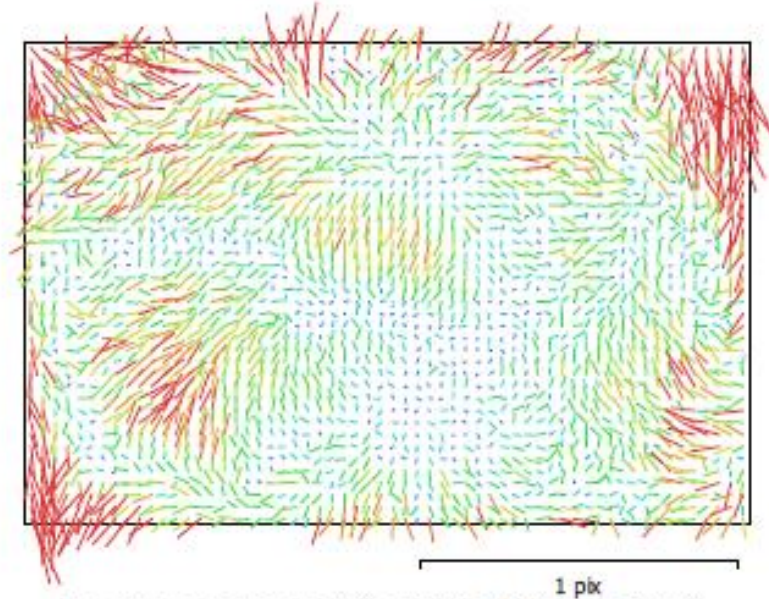


Fig. 2. Image residuals for NIKON D7200 (18mm).

NIKON D7200 (18mm)

363 images

Type	Resolution	Focal Length	Pixel Size
Frame	6000 x 4000	18 mm	3.91 x 3.91 μm
F:	4695.1		
Cx:	5.35093	B1:	-0.255264
Cy:	-3.45795	B2:	-0.376577
K1:	-0.150727	P1:	0.00051244
K2:	0.10443	P2:	0.000377627
K3:	0.00587342	P3:	-0.260169
K4:	-0.00404212	P4:	1.0389

Scale Bars

Label	Distance (m)	Error (m)
target 49_target 50	0.49959	-0.000300226
target 50_target 51	0.499841	0.000741175
target 52_target 53	0.250089	0.000139031
target 53_target 54	0.249828	-0.000142482
target 55_target 56	0.249909	-9.14251e-005
target 57_target 58	0.500007	-6.31859e-005
target 58_target 59	0.499738	-0.000292177
target 60_target 61	0.249922	-6.83958e-005
target 61_target 62	0.250061	-8.92944e-006
Total		0.000294691

Table 2. Control scale bars.

Digital Elevation Model

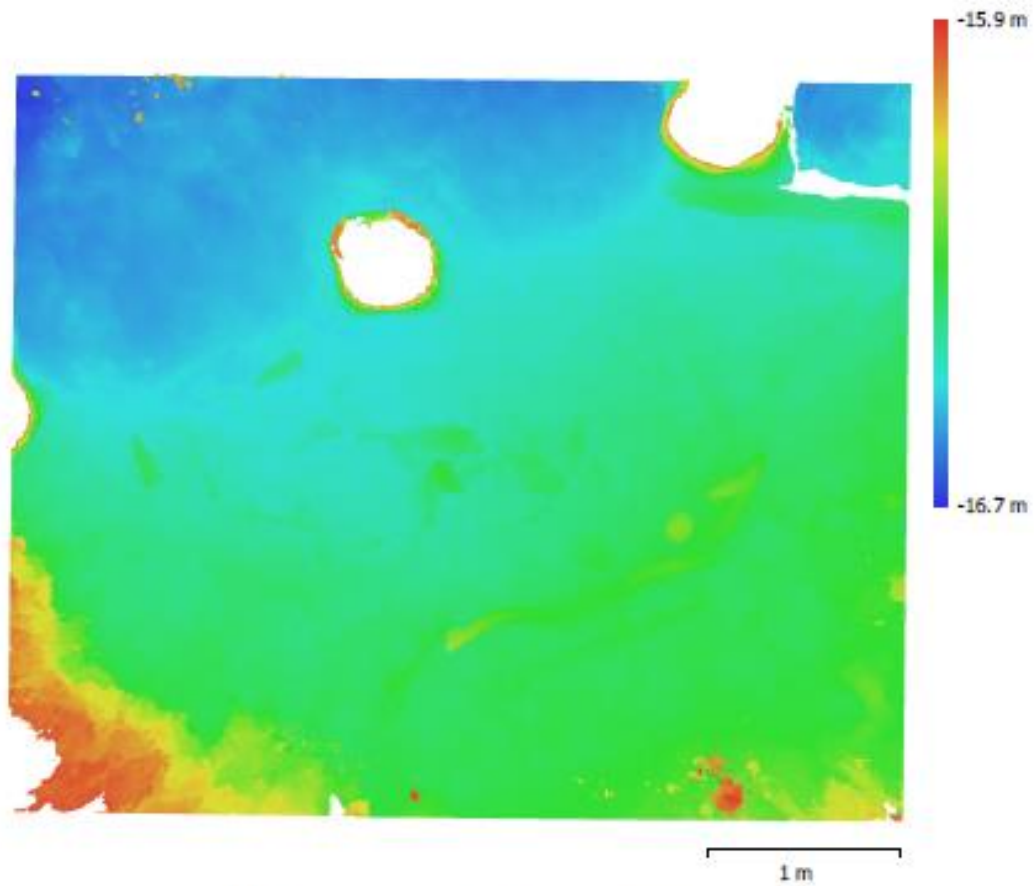


Fig. 3. Reconstructed digital elevation model.

Resolution: 0.795 mm/pix
Point density: 1.58 points/mm²

Processing Parameters

General

Cameras	363
Aligned cameras	357
Markers	16
Scale bars	9
Coordinate system	Local Coordinates (m)
Rotation angles	Yaw, Pitch, Roll

Point Cloud

Points	609,349 of 1,563,993
RMS reprojection error	0.124814 (0.393408 pix)
Max reprojection error	1.05015 (5.48098 pix)
Mean key point size	3.07535 pix
Point colors	3 bands, uint8
Key points	No
Average tie point multiplicity	2.91757

Alignment parameters

Accuracy	High
Generic preselection	Yes
Key point limit	60,000
Tie point limit	0
Adaptive camera model fitting	No
Matching time	22 minutes 15 seconds
Alignment time	32 minutes 42 seconds

Optimization parameters

Parameters	f, b1, b2, cx, cy, k1-k4, p1-p4
Adaptive camera model fitting	No
Optimization time	59 seconds

Depth Maps

Count	334
-------	-----

Reconstruction parameters

Quality	High
Filtering mode	Mild
Processing time	4 hours 48 minutes

Dense Point Cloud

Points	44,156,363
Point colors	3 bands, uint8

Reconstruction parameters

Quality	High
Depth filtering	Mild
Depth maps generation time	4 hours 48 minutes
Dense cloud generation time	3 days 23 hours

Model

Faces	8,831,055
Vertices	4,434,529
Vertex colors	3 bands, uint8
Texture	8,192 x 8,192, 4 bands, uint8

Reconstruction parameters

Surface type	Arbitrary
Source data	Dense
Interpolation	Enabled

General

Quality	High
Depth filtering	Mid
Face count	8,831,055
Processing time	40 minutes 38 seconds

Texturing parameters

Mapping mode	Generic
Blending mode	Mosaic
Texture size	8,192 x 8,192
Enable hole filling	Yes
Enable ghosting filter	Yes
UV mapping time	3 minutes 10 seconds
Blending time	10 minutes 37 seconds

Orthomosaic

Size	11,865 x 9,844
Coordinate system	Local Coordinates (m)
Colors	3 bands, uint8

Reconstruction parameters

Blending mode	Mosaic
Surface	Mesh
Enable hole filling	Yes
Processing time	3 minutes 13 seconds

Software

Version	1.5.1 build 7618
Platform	Windows 64

MODEL 4 PROCESSING REPORT

Agisoft Metashape

**Processing Report
27 September 2019**



Survey Data

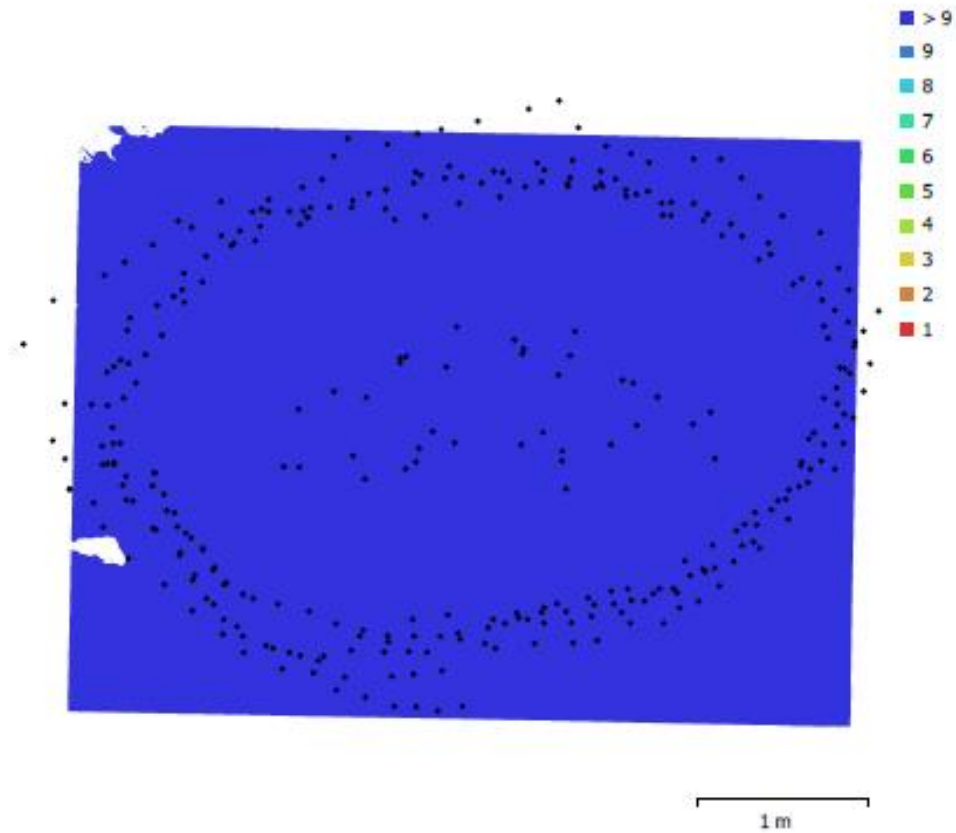


Fig. 1. Camera locations and image overlap.

Number of images:	327	Camera stations:	327
Flying altitude:	1.6 m	Tie points:	475,920
Ground resolution:	0.376 mm/pix	Projections:	1,343,208
Coverage area:	15.9 m ²	Reprojection error:	0.329 pix

Camera Model	Resolution	Focal Length	Pixel Size	Precalibrated
NIKON D7200 (18mm)	6000 x 4000	18 mm	3.91 x 3.91 μm	No

Table 1. Cameras.

Camera Calibration

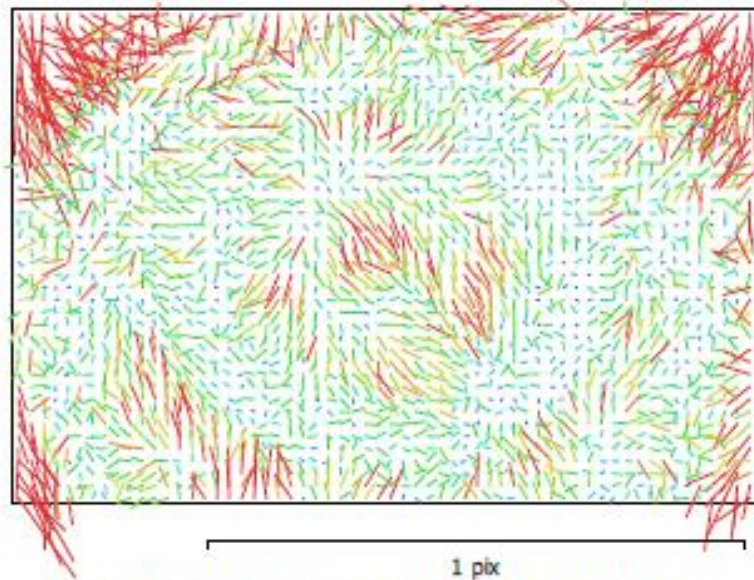


Fig. 2. Image residuals for NIKON D7200 (18mm).

NIKON D7200 (18mm)

327 images

Type	Resolution	Focal Length	Pixel Size
Frame	6000 x 4000	18 mm	3.91 x 3.91 μm
F:	4673.13		
Cx:	0.818771	B1:	-0.141987
Cy:	12.1206	B2:	0.248923
K1:	-0.156071	P1:	0.000405696
K2:	0.115205	P2:	0.000525757
K3:	-0.0147351	P3:	0.729496
K4:	0.00819415	P4:	0.0706281

Scale Bars

Label	Distance (m)	Error (m)
target 49_target 50	0.499596	-0.00029406
target 50_target 51	0.499857	0.000756759
target 52_target 53	0.24982	-0.00012989
target 53_target 54	0.249829	-0.000140523
target 55_target 56	0.249914	-8.60924e-005
target 57_target 58	0.499865	-0.000205242
target 58_target 59	0.500163	0.000133322
target 60_target 61	0.249877	-0.000113458
target 61_target 62	0.249758	-0.000312426
Total		0.000311549

Table 2. Control scale bars.

Digital Elevation Model

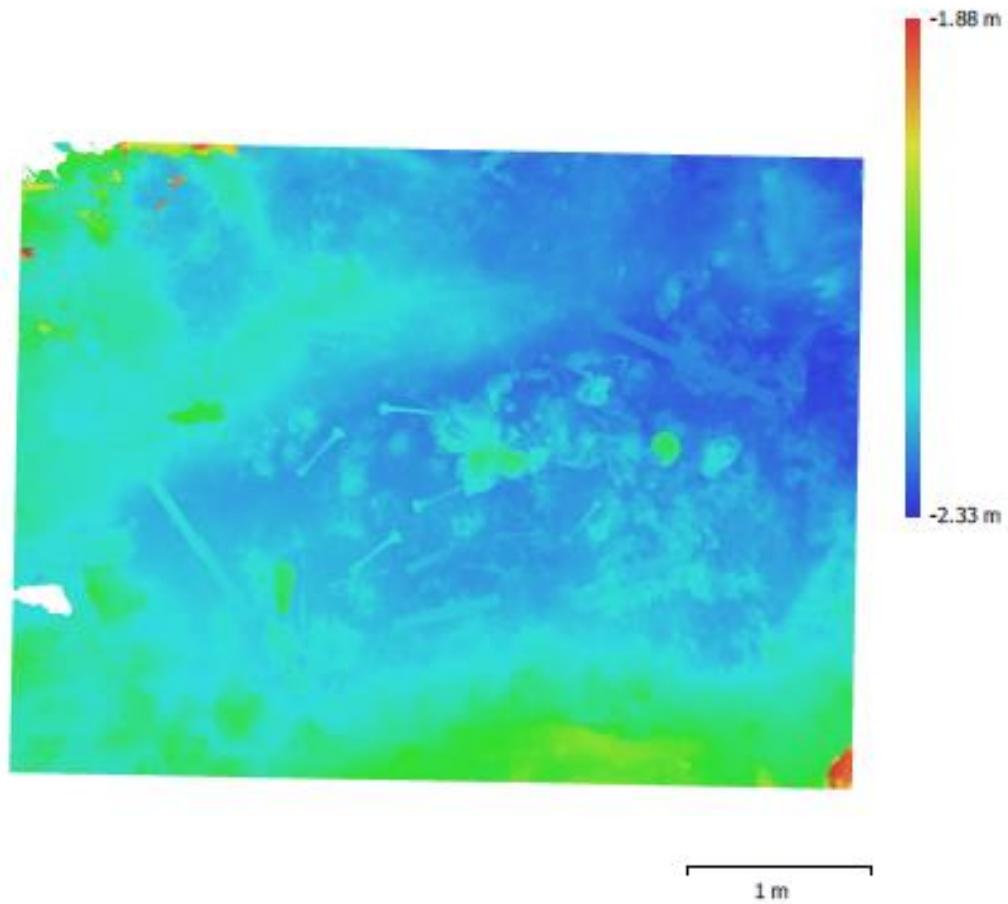


Fig. 3. Reconstructed digital elevation model.

Resolution: 0.752 mm/pix
Point density: 1.77 points/mm²

Processing Parameters

General

Cameras	327
Aligned cameras	327
Markers	17
Scale bars	9
Coordinate system	Local Coordinates (m)
Rotation angles	Yaw, Pitch, Roll

Point Cloud

Points	475,920 of 1,421,613
RMS reprojection error	0.131409 (0.329009 pix)
Max reprojection error	2.27389 (6.21281 pix)
Mean key point size	2.46522 pix
Point colors	3 bands, uint8
Key points	No
Average tie point multiplicity	3.09123

Alignment parameters

Accuracy	High
Generic preselection	Yes
Key point limit	60,000
Tie point limit	0
Adaptive camera model fitting	No
Matching time	50 minutes 12 seconds
Alignment time	9 minutes 58 seconds

Optimization parameters

Parameters	f, b1, b2, cx, cy, k1-k4, p1-p4
Adaptive camera model fitting	No
Optimization time	24 seconds

Depth Maps

Count	327
Reconstruction parameters	
Quality	High
Filtering mode	Mild
Processing time	2 days 1 hours

Dense Point Cloud

Points	39,557,340
Point colors	3 bands, uint8
Reconstruction parameters	
Quality	High
Depth filtering	Mild
Depth maps generation time	2 days 1 hours
Dense cloud generation time	4 days 13 hours

Model

Faces	7,911,352
Vertices	3,966,432
Vertex colors	3 bands, uint8
Texture	8,192 x 8,192, 4 bands, uint8
Reconstruction parameters	
Surface type	Arbitrary
Source data	Dense
Interpolation	Enabled

General

Quality	High
Depth filtering	Mild
Face count	7,911,352
Processing time	37 minutes 47 seconds

Texturing parameters

Mapping mode	Generic
Blending mode	Mosaic
Texture size	8,192 x 8,192
Enable hole filling	Yes
Enable ghosting filter	Yes
UV mapping time	3 minutes 37 seconds
Blending time	41 minutes 7 seconds

Orthomosaic

Size	12,627 x 9,656
Coordinate system	Local Coordinates (m)
Colors	3 bands, uint8

Reconstruction parameters

Blending mode	Mosaic
Surface	Mesh
Enable hole filling	Yes
Processing time	19 minutes 39 seconds

Software

Version	1.5.1 build 7618
Platform	Windows 64

MODEL 5 PROCESSING REPORT

Agisoft Metashape

Processing Report
28 September 2019



Survey Data

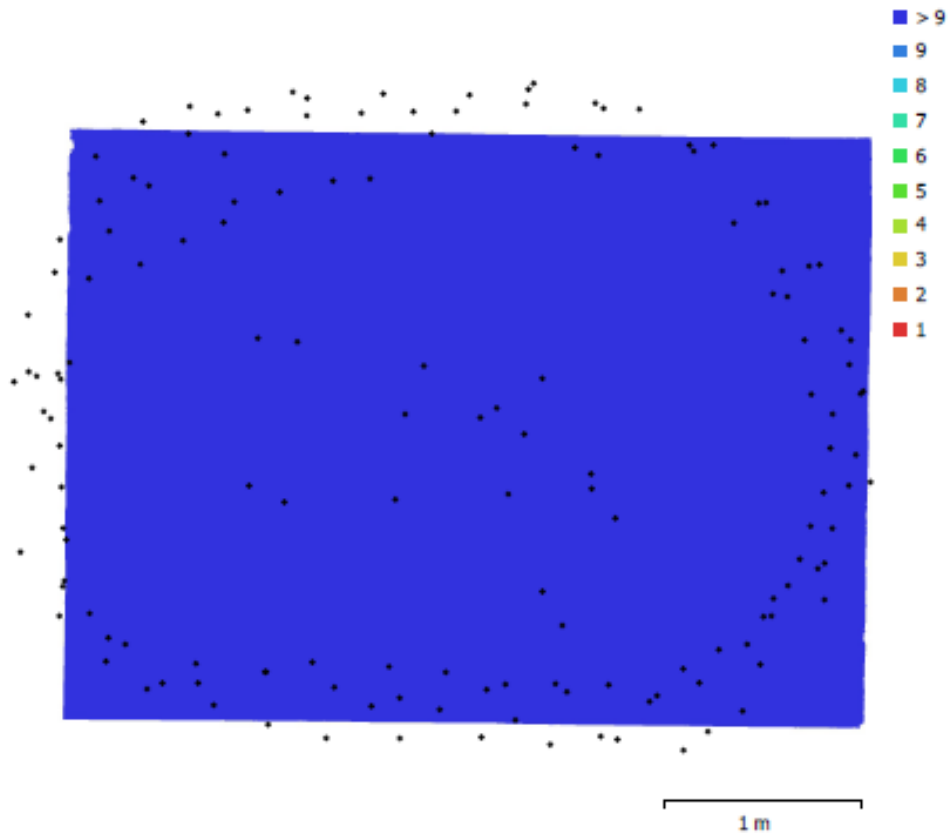


Fig. 1. Camera locations and image overlap.

Number of images:	148	Camera stations:	148
Flying altitude:	1.8 m	Tie points:	112,857
Ground resolution:	0.4 mm/pix	Projections:	257,165
Coverage area:	12.2 m ²	Reprojection error:	0.661 pix

Camera Model	Resolution	Focal Length	Pixel Size	Precalibrated
NIKON D7200 (18mm)	6000 x 4000	18 mm	3.91 x 3.91 μ m	No

Table 1. Cameras.

Camera Calibration

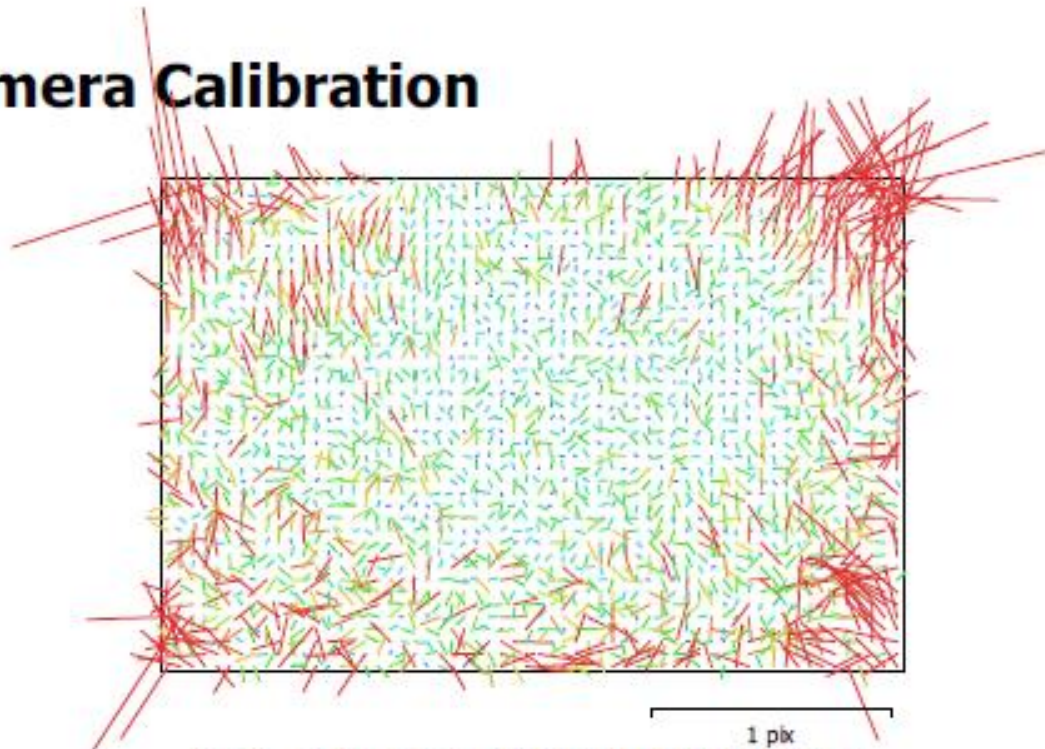


Fig. 2. Image residuals for NIKON D7200 (18mm).

NIKON D7200 (18mm)

148 images

Type	Resolution	Focal Length	Pixel Size
Frame	6000 x 4000	18 mm	3.91 x 3.91 μm
F:	4645.85		
Cx:	1.98343	B1:	-1.64848
Cy:	43.4566	B2:	-0.49315
K1:	-0.152829	P1:	0.000419588
K2:	0.106002	P2:	0.000304458
K3:	0	P3:	0
K4:	0	P4:	0

Scale Bars

Label	Distance (m)	Error (m)
target 49_target 50	0.499591	-0.000299134
target 50_target 51	0.499726	0.000625796
target 53_target 54	0.250111	0.000140657
target 55_target 56	0.249856	-0.000144342
target 57_target 58	0.500031	-3.93058e-005
target 58_target 59	0.499864	-0.000166095
target 60_target 61	0.249947	-4.34544e-005
target 61_target 62	0.249917	-0.00015265
Total		0.000268338

Table 2. Control scale bars.

Label	Distance (m)	Error (m)
target 63_target 64	0.249951	-1.93882e-005
Total		1.93882e-005

Table 3. Check scale bars.

Digital Elevation Model

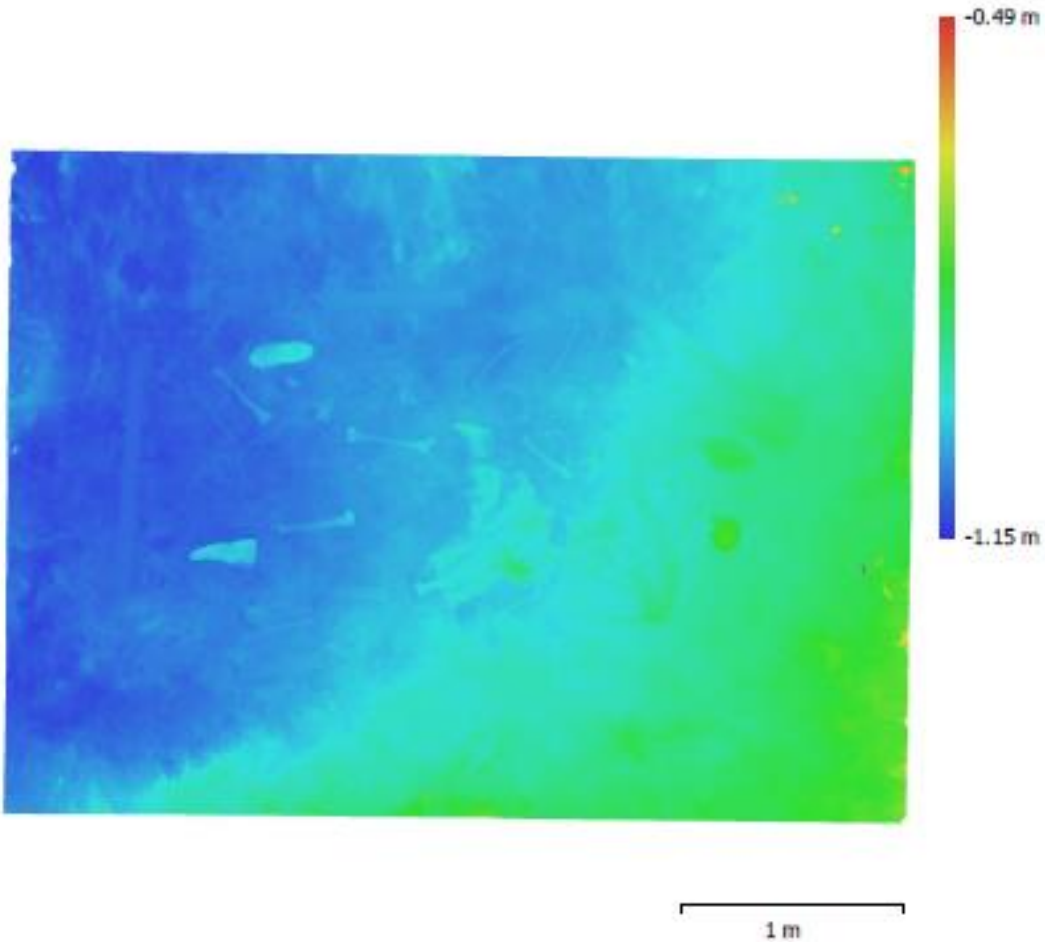


Fig. 3. Reconstructed digital elevation model.

Resolution: 0.799 mm/pix
Point density: 1.56 points/mm²

Processing Parameters

General

Cameras	148
Aligned cameras	148
Markers	15
Scale bars	9
Coordinate system	Local Coordinates (m)
Rotation angles	Yaw, Pitch, Roll

Point Cloud

Points	112,857 of 163,489
RMS reprojection error	0.136136 (0.660594 pix)
Max reprojection error	1.25806 (13.2405 pix)
Mean key point size	4.30124 pix
Point colors	3 bands, uint8
Key points	No
Average tie point multiplicity	2.64643

Alignment parameters

Accuracy	High
Generic preselection	Yes
Key point limit	60,000
Tie point limit	0
Adaptive camera model fitting	No
Matching time	19 minutes 47 seconds
Alignment time	3 minutes 54 seconds

Optimization parameters

Parameters	f, b1, b2, cx, cy, k1, k2, p1, p2
Adaptive camera model fitting	No
Optimization time	13 seconds

Depth Maps

Count	148
-------	-----

Reconstruction parameters

Quality	High
Filtering mode	Mild
Processing time	14 hours 4 minutes

Dense Point Cloud

Points	32,961,126
Point colors	3 bands, uint8

Reconstruction parameters

Quality	High
Depth filtering	Mild
Depth maps generation time	14 hours 4 minutes
Dense cloud generation time	6 hours 57 minutes

Model

Faces	6,592,100
Vertices	3,305,905
Vertex colors	3 bands, uint8
Texture	8,192 x 8,192, 4 bands, uint8

Reconstruction parameters

Surface type	Arbitrary
Source data	Dense
Interpolation	Enabled

General	
Quality	High
Depth filtering	Mild
Face count	6,592,101
Processing time	29 minutes 6 seconds
Texturing parameters	
Mapping mode	Generic
Blending mode	Mosaic
Texture size	8,192 x 8,192
Enable hole filling	Yes
Enable ghosting filter	Yes
UV mapping time	6 minutes 25 seconds
Blending time	26 minutes 12 seconds
Orthomosaic	
Size	10,266 x 7,597
Coordinate system	Local Coordinates (m)
Colors	3 bands, uint8
Reconstruction parameters	
Blending mode	Mosaic
Surface	Mesh
Enable hole filling	Yes
Processing time	10 minutes 22 seconds
Software	
Version	1.5.1 build 7618
Platform	Windows 64

MODEL 6 PROCESSING REPORT

Agisoft Metashape

**Processing Report
27 September 2019**



Survey Data

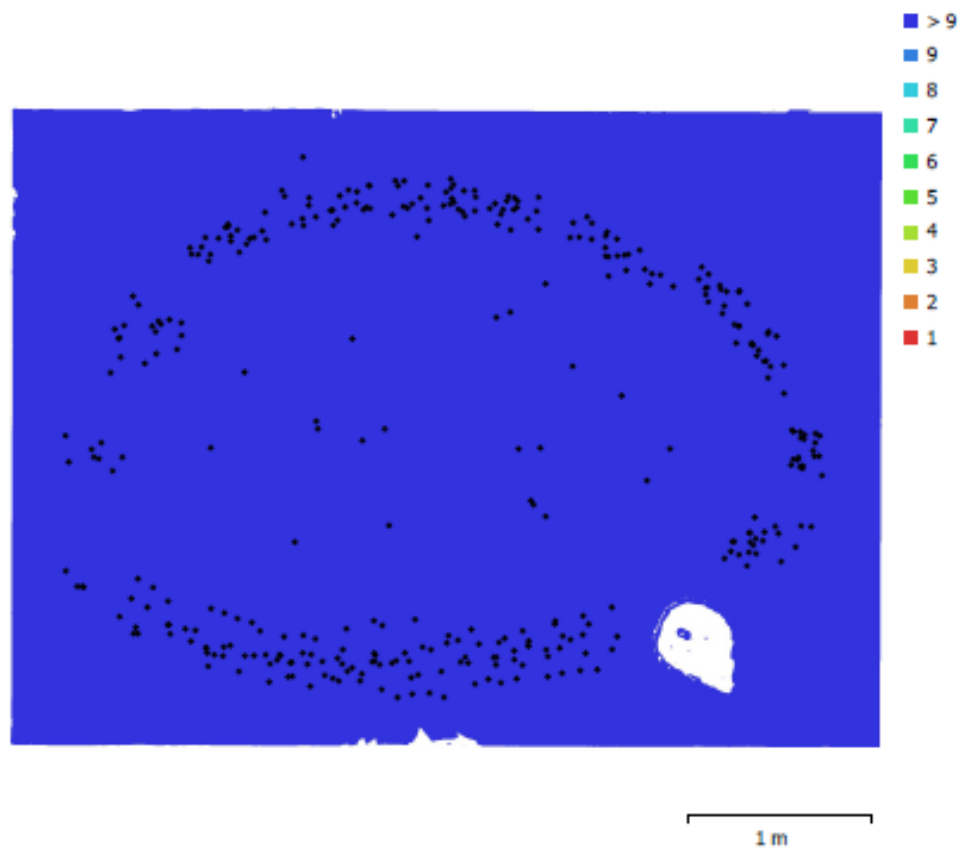


Fig. 1. Camera locations and image overlap.

Number of images:	360	Camera stations:	360
Flying altitude:	1.56 m	Tie points:	484,832
Ground resolution:	0.358 mm/pix	Projections:	1,315,521
Coverage area:	16.3 m ²	Reprojection error:	0.864 pix

Camera Model	Resolution	Focal Length	Pixel Size	Precalibrated
NIKON D7200 (18mm)	6000 x 4000	18 mm	3.91 x 3.91 μm	No

Table 1. Cameras.

Camera Calibration

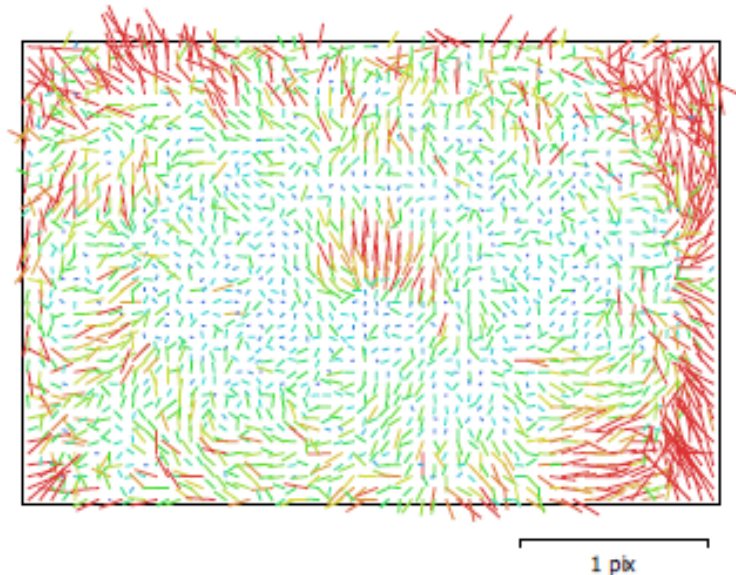


Fig. 2. Image residuals for NIKON D7200 (18mm).

NIKON D7200 (18mm)

360 images

Type	Resolution	Focal Length	Pixel Size
Frame	6000 x 4000	18 mm	3.91 x 3.91 μm

	Value	Error	F	Cx	Cy	B1	B2	K1	K2	K3	K4	P1	P2	P3	P4
F	4659.28	0.087	1.00	0.05	-0.59	-0.10	-0.09	-0.27	0.25	-0.22	0.21	0.10	0.20	-0.07	0.04
Cx	5.45299	0.088		1.00	0.04	-0.05	0.50	-0.00	-0.00	0.01	-0.01	0.53	0.09	-0.12	0.14
Cy	-2.94207	0.12			1.00	-0.51	0.05	-0.05	0.02	-0.02	0.02	0.04	0.12	-0.05	0.07
B1	-0.942425	0.031				1.00	-0.01	0.01	-0.02	0.02	-0.02	0.03	0.13	-0.04	0.01
B2	0.0307289	0.028					1.00	0.00	-0.00	-0.00	0.00	0.01	-0.08	0.06	-0.01
K1	-0.153986	0.00012						1.00	-0.97	0.93	-0.87	-0.06	-0.08	0.09	-0.09
K2	0.0981407	0.00075							1.00	-0.99	0.96	0.06	0.05	-0.09	0.10
K3	0.0181687	0.0019								1.00	-0.99	-0.05	-0.04	0.09	-0.10
K4	-0.0220221	0.0016									1.00	0.05	0.03	-0.08	0.09
P1	0.000605662	5.9e-006										1.00	0.63	-0.82	0.76
P2	0.000527757	5.9e-006											1.00	-0.71	0.64
P3	0.608017	0.043												1.00	-0.97
P4	-0.339513	0.055													1.00

Table 2. Calibration coefficients and correlation matrix.

Scale Bars

Label	Distance (m)	Error (m)
target 49_target 50	0.500709	0.000818592
target 50_target 51	0.498607	-0.00049264
target 52_target 53	0.249968	1.77655e-005
target 53_target 54	0.249971	9.48925e-007
target 55_target 56	0.250112	0.000112187
target 57_target 58	0.499836	-0.000234085
target 60_target 61	0.249734	-0.000256241
target 61_target 62	0.250004	-6.56705e-005
Total		0.000362363

Table 3. Control scale bars.

Digital Elevation Model

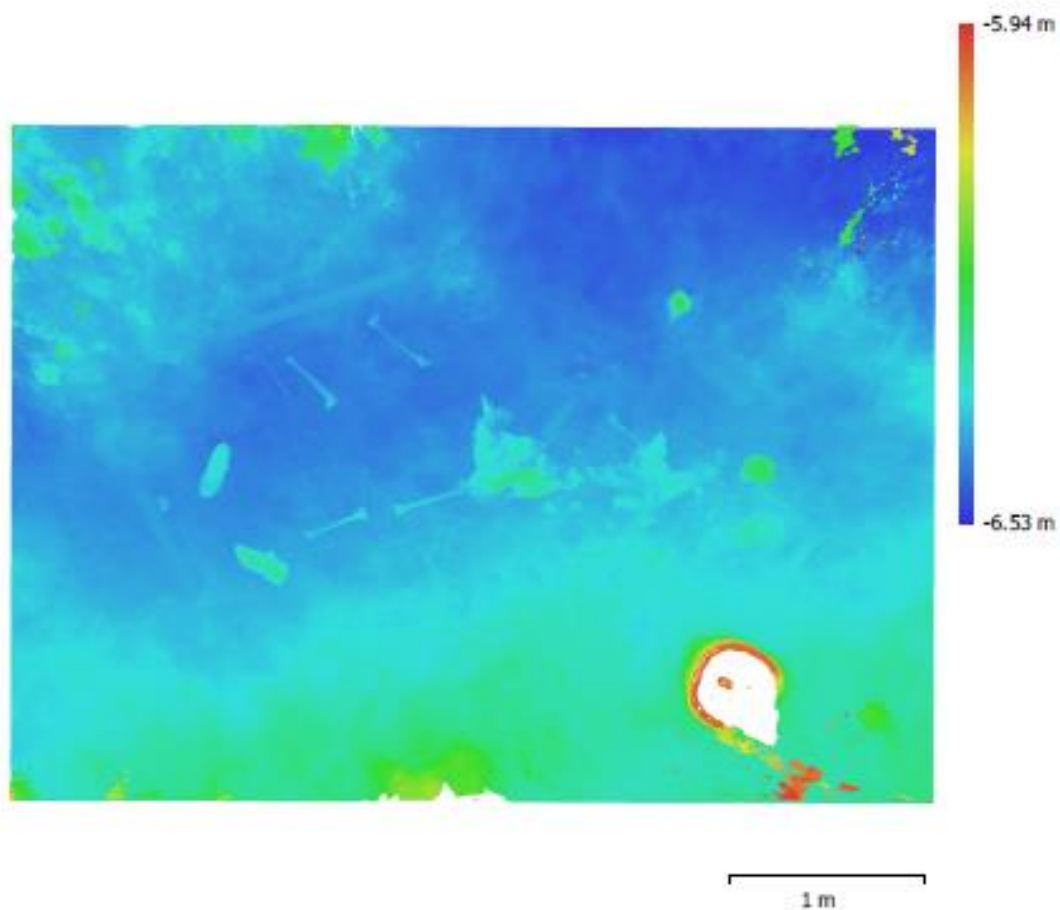


Fig. 3. Reconstructed digital elevation model.

Resolution: 0.717 mm/pix
Point density: 1.95 points/mm²

Processing Parameters

General

Cameras	360
Aligned cameras	360
Markers	15
Scale bars	8
Coordinate system	Local Coordinates (m)
Rotation angles	Yaw, Pitch, Roll

Point Cloud

Points	484,832 of 1,806,791
RMS reprojection error	0.260066 (0.863656 pix)
Max reprojection error	2.83802 (11.0805 pix)
Mean key point size	3.27256 pix
Point colors	3 bands, uint8
Key points	No
Average tie point multiplicity	3.13011

Alignment parameters

Accuracy	High
Generic preselection	Yes
Key point limit	60,000
Tie point limit	0
Adaptive camera model fitting	No
Matching time	26 minutes 16 seconds
Alignment time	22 minutes 33 seconds

Optimization parameters

Parameters	f, b1, b2, cx, cy, k1-k4, p1-p4
Adaptive camera model fitting	No
Optimization time	16 seconds

Depth Maps

Count	360
-------	-----

Reconstruction parameters

Quality	High
Filtering mode	Mild
Processing time	5 hours 20 minutes

Dense Point Cloud

Points	51,440,117
Point colors	3 bands, uint8

Reconstruction parameters

Quality	High
Depth filtering	Mild
Depth maps generation time	5 hours 20 minutes
Dense cloud generation time	5 days 17 hours

Model

Faces	10,287,883
Vertices	5,163,344
Vertex colors	3 bands, uint8
Texture	8,192 x 8,192, 4 bands, uint8

Reconstruction parameters

Surface type	Arbitrary
Source data	Dense
Interpolation	Enabled

General	
Quality	High
Depth filtering	Mild
Face count	10,287,883
Processing time	42 minutes 34 seconds
Texturing parameters	
Mapping mode	Generic
Blending mode	Mosaic
Texture size	8,192 x 8,192
Enable hole filling	Yes
Enable ghosting filter	Yes
UV mapping time	7 minutes 35 seconds
Blending time	41 minutes 51 seconds
Orthomosaic	
Size	13,265 x 9,741
Coordinate system	Local Coordinates (m)
Colors	3 bands, uint8
Reconstruction parameters	
Blending mode	Mosaic
Surface	Mesh
Enable hole filling	Yes
Processing time	20 minutes 25 seconds
Software	
Version	1.5.1 build 7618
Platform	Windows 64

LIST OF REFERENCES

- Agisoft LLC 2018 Agisoft PhotoScan User Manual: Professional Edition, Version 1.5. Electronic document, <https://www.agisoft.com/>, accessed 9/26/2019.
- Agosto, Eros, Andrea Ajmar, Piero Boccardo, Fabio G. Tonolo, and Andrea Lingua. 2008 Crime Scene Reconstruction Using a Fully Geomatic Approach. *Sensors* 8: 6280-6302.
- Aldridge, Kristina, Simeon A. Boyadjiev, George T. Capone, Valerie B. DeLeon, and Joan T. Richtsmeier. 2005 Precision and Error of Three-Dimensional Phenotypic Measures Acquired from 3dMD Photogrammetric Images. *American Journal of Medical Genetics Part A* 138(3): 247-253.
- Al-Ruzouq, Rami and Saleh A. Dabous. 2017 Archaeological Site Information Modelling and Management Based on Close-Range Photogrammetry and GIS. *Conservation and Management of Archaeological Sites* 19(3): 156-172.
- Andalo, Fernanda A., Fatih Calakli, Gabriel Taubin, and Siome Goldenstein. 2011 Accurate 3D footwear impression recovery from photographs.
- Andreou, Georgia M., Rachel Opitz, Sturt W. Manning, Kevin D. Fisher, David A. Sewell, Artemis Georgiou, and Thomas Urban. 2017 Integrated Methods for Understanding and Monitoring the Loss of Coastal Archaeological Sites: The case of Tochni-Lakkia, South-Central Cyprus. *Journal of Archaeological Science: Reports* 12: 197-208.
- Aziz, Saiful A.B., Zulkepli Bin Majid, and Halim Bin Setan. 2010 Application of Close Range Photogrammetry in Crime Scene Investigation (CSI) Mapping Using Iwitness and Crime Zone Software. *Geoinformation Science Journal* 10(1):1-16.
- Balletti, C., C. Beltrame, E. Costa, F. Guerra, and P. Vernier. 2015 Underwater Photogrammetry and 3D Reconstruction of Marble Cargos Shipwreck. *The International Archives of the Photogrammetry, Remote Sensing and Spatial Information Sciences, Volume XL-5/W5:7-13*.
- Barazzetti, L. R. Sala, M. Scaioni, C. Cattaneo, D. Gibelli, A. Giussani, P. Poppa, F. Roncoroni, and A. Vandone. 2012 3D Scanning and Imaging for Quick Documentation of Crime and Accident Scenes. *Proc. SPIE 8359, Sensors, and Command, Control, Communications, and Intelligence (C3I) Technologies for Homeland Security and Homeland Defense XI*, 835910.
- Behring, Dirk, Jan Thesing, Holger Becker, and Robert Zobel. 2012 Optical Coordinate Measuring Techniques for the Determination and Visualization of 3D Displacements in Crash Investigations. *Society of Automotive Engineers, Inc.* 03-B55.
- Bollinger, Michael J., Ursula Buck, Michael J. Thali, Stephan A Bolliger. 2012 Reconstruction and 3D Visualisation Based on Objective Real 3D Based Documentation. *Forensic Science and Medical Pathology* 8: 208-217.

- Bruschweiler, W., M. Braun, R. Dirnhofer, and M.J. Thali. 2003 Analysis of Patterned Injuries and Injury-Causing Instruments with Forensic 3D/CAD Supported Photogrammetry (FPHG): An Instruction Manual for the Documentation Process. *Forensic Science International* 132: 130-138.
- Buck, Ursula, Silvio Naether, Marcel Braun, Stephan Bolliger, Hans Friederich, Christian Jackowski, Emin Aghayev, Andreas Christe, Peter Vock, Richard Dirnhofer, and Michael J. Thali. 2007 Application of 3D Documentation and Geometric Reconstruction Methods in Traffic Accident Analysis: With High Resolution Surface Scanning, Radiological MSCT/MRI Scanning and Real Data Based Animation. *Forensic Science International* 170(1):20-28.
- Buck, Ursula, Silvio Naether, Beat Rass, Christian Jackowski, and Michael J. Thali. 2013 Accident or Homicide - Virtual Crime Scene Reconstruction Using 3D Methods. *Forensic Science International* 225: 75-84.
- Caroti, G. I. Martinez-Espejo Zargoza, and A. Piemonte. 2015 Accuracy Assessment in Structure From Motion 3D Reconstruction from UAV-Born Images: The Influence of the Data Processing Methods. *The International Archives of the Photogrammetry, Remote Sensing and Spatial Information Sciences*, Volume XL-1/W4:103-109.
- Casana, Jesse, John Kantner, Adam Wiewel and Jackson Cothren. 2014 Archaeological Aerial Thermography: A Case Study at the Chaco-Era Blue J Community, New Mexico. *Journal of Archaeological Science* 45: 207-219.
- Cavagnini, Gianluca, Giovanna Sansoni, and Marco Trebeschi. 2009 Using 3D Range Cameras for Crime Scene Documentation and Legal Medicine. *Proc. SPIE 7239, Three-Dimensional Imaging Metrology*.
- Cultural Heritage Imaging 2020 Photogrammetry Training
<http://culturalheritageimaging.org/Technologies/Photogrammetry/>, accessed March 10 2020.
- Chiabrando, Filiberto, Francesco D'Andria, Giulia Sammartano, and Antonia Spano. 2018 UAV Photogrammetry for Archaeological Site Survey. 3D Models at the Hierapolis in Phrgia (Turkey). *Virtual Archaeology Review* 9(18):28-43.
- Connor, Melissa A. 2007 *Forensic Methods: Excavation for the Archaeologist and Investigator*. Altamira Press, Lanham , MD.
- Constantino, D., M. G. Angelini, and F. Mazzone. 2016 Integrated Survey Methodology for the Crime Reconstruction. *The Imaging Science Journal* 64(6): 341-351.
- Crist, T. A. J. 2001 Bad to the bone?: Historical archaeologist in the practice of forensic science. *Historical archaeology* 35:39-56.
- De Reu, Jeroen, Gertjan Plets, Geert Verhoeven, Philippe De Smedt, Machteld Bats, Bart Cherrette, Wouter De Maeyer, Jasper Deconynck, Davy Herremans, Pieter Laloo, Marc

- Van Meirvenne, and Wim De Clercq. 2013 Towards a Three-Dimensional Cost-Effective Registration of the Archaeological Heritage. *Journal of Archaeological Science* 40: 1108-1121.
- Dirkmaat, Dennis C. 2012 Documenting Context at the Outdoor Crime Scene: Why Bother? In *A Companion to Forensic Anthropology*, Dennis C. Dirkmaat, editor, pp. 49-65. Wiley-Blackwell, UK.
- Dirkmaat, D. C., and J. M. Adovasio. 1997 The role of archaeology in the recovery and interpretation of human remains from an outdoor setting. In *Forensic taphonomy: the postmortem fate of human remains* (pp. 39-64), W. D. Haglund and M. H. Sorg (Eds.). CRC Press, Boca Raton, FL.
- Dirkmaat, Dennis C., and Luis L. Cabo. 2016 Forensic archaeology and forensic taphonomy: basic considerations on how to properly process and interpret the outdoor forensic scene. *Academic forensic pathology* 6(3):439-454.
- Doneus, Michael, Geert J. Verhoeven, Martin Fera, C. Briese, Mathias Kucera, and Wolfgang Neubauer. 2011 From Deposit to Point Cloud - A Study of Low-Cost Computer Vision Approaches for the Straightforward Documentation of Archaeological Excavations. *Geoinformatics* 6:81-88.
- Douglass, Matthew, Sam Lin, and Michael Chodoronek. 2015 The Application of 3D Photogrammetry for In-Field Documentation of Archaeological Features. *Advances in Archaeological Practice* 3(2): 136-152.
- Drap, Pierre, Odile Papini, Elisa Pruno, Michele Nucciotti, and Guido Vannini. 2017 Ontology-Based Photogrammetry Survey for Medieval Archaeology: Toward a 3D Geographic Information System (GIS). *Geosciences* 7(93): 1-33.
- Dupras, Tosha L., John J. Schultz, Sandra M. Wheeler, and Lana J. Williams. 2012 *Forensic Recovery of Human Remains, Second Edition*. CRC Press, Boca Raton, FL.
- Errickson, David, Tim J. U. Thompson, and Brian W. J. Rankin. 2014. The application of 3D visualization of osteological trauma for the courtroom: a critical review. *Journal of Forensic Radiology and Imaging* 2(3):132-137.
- Falkingham, Peter L. 2016 Trying All the Free Photogrammetry. Electronic document, <https://peterfalkingham.com/2016/09/14/trying-all-the-free-photogrammetry/>, accessed February 19, 2020.
- Faulkner, Sean. 2017 Photogrammetry of 3D footwear impressions forensic applications. Doctoral dissertation, Murdoch University.
- FLT Geosystems 2020. Leica ScanStation P40 3D Laser Scanner. Accessed June 10, 2020. <https://secure.fltgeosystems.com/laser-scanners-3d/leica-scanstation-p40-3d-laser-scanner-lca6009377/>.

- Forte, Maurizio. 2014 3D Archaeology: New Perspectives and Challenges - The Example of Catalhoyuk. *Journal of Eastern Mediterranean Archaeology and Heritage Studies* 2(1): 1-29.
- Fraser, Clive S., Harry Hanley, and Simon Cronk. 2005 Close-Range photogrammetry for accident reconstruction. *Optical 3D Measurements VII* 2:115-123.
- Fraser, Clive, Simon Cronk, and Harry Hanley. 2008 Close-range photogrammetry in traffic incident management. In *Proceeding of XXI ISPRS congress commission V, WGV*, Citeseer 1:125-128.
- Fulton, Carrie, Andrew Viduka, Andrew Hutchison, Joshua Hollick, Andrew Woods, David Sewell, and Sturt Manning. 2016 Use of Photogrammetry for Non-Disturbance Underwater Survey: An Analysis of In Situ Stone Anchors. *Advances in Archaeological Practice* 4(1): 17-30.
- Galantucci, Luigi M., Fulvio Lavecchia, and Gianluca Percoco. 3D Face measurement and scanning using digital close range photogrammetry: evaluation of different solutions and experimental approaches. In *Proceedings of the International Conference on 3D Body Scanning Technologies* 9-20.
- Garstki, Kevin, Marcus Schulenburg, and Robert A. Cook. 2018 Practical Application of Digital Photogrammetry for Fieldwork in the American Midwest: An Example from the Middle Ohio Valley. *Midcontinental Journal of Archaeology* 43(2): 133-150.
- Gidusko, Kevin. 2018 Testing the Capability of Close-Range Photogrammetry to Document Outdoor Forensic Scenes With Skeletal Remains Using Mock Scenarios. *Electronic Theses and Dissertations*. 6026.
- Green, Susie, Andrew Bevan, and Michael Shapland. 2014 A Comparative Assessment of Structure from Motion Methods for Archaeological Research. *Journal of Archaeological Science* 46: 173-181.
- Grip, Wayne M., Randall, W. Grip, and Robert D. Morrison. 2000 Application of Aerial Photography and Photogrammetry in Environmental Forensic Investigations. *Journal of Environmental Forensics* 1: 121-129.
- Haukaas, Colleen, and Lisa M. Hodgetts. 2016 The Untapped Potential of Low-Cost Photogrammetry in Community-Based Archaeology: A Case Study From Banks Island, Arctic Canada. *Journal of Community Archaeology & Heritage* 3(1): 40-56.
- Holowko, Elwira, Kamil Januszkiewicz, Pawel Bolewicki, Robert Sitnik, and Jakub Michonski. 2016 Application of Multiple-Resolution 3D Techniques in Crime Scene Documentation with Bloodstain Pattern Analysis. *Forensic Science International* 267: 218-227.

- Hoogeboom, Bart, Ivo Alberink, and Derk Vridag. 2015 Photogrammetry in Digital Forensics. In *Handbook of Digital Forensics of Multimedia Data and Devices*, First edition, Anthony T. S. Ho and Shujun Li, editors, pp. 185-218. John Wiley & Sons, Ltd, New York, NY.
- Howland, Matthew D., Ian W. N. Jones, Mohammad Najjar, and Thomas E. Levy. 2018 Quantifying the Effects of Erosion on Archaeological Sites with Low-Altitude Aerial Photography, Structure from Motion, and GIS: A Case Study from Southern Jordan. *Journal of Archaeological Science* 90: 62-70.
- Jalandoni, Andrea, Ines Domingo, and Paul S. C. Tacon. 2018 Testing the Value of Low-Cost Structure-from-Motion (SfM) Photogrammetry for Metric and Visual Analysis of Rock Art. *Journal of Archaeological Science: Reports* 17: 605-616.
- Jennings, Alan, and Jonathan Black. 2012 Texture-Based Photogrammetry Accuracy on Curved Surfaces. *AIAA Journal* 50(5): 1060-1071.
- Jones, Christine A., and Elizabeth Church. 2020 Photogrammetry is for Everyone: Structure-from-Motion Software User Experiences in Archaeology. *Journal of Archaeological Science: Reports* 30(102261).
- Komar, Debra A., Stephanie Davy-Jow, and Summer J. Decker. 2012 The Use of a 3-D Laser Scanner to Document Ephemeral Evidence at Crime Scenes and Postmortem Examinations. *Journal of Forensic Science* 57(1): 188-191.
- Kottner, Soren, Lars C. Ebert, Garyfalia Ampanozi, Marcel Braun, Michael J. Thali, and Dominic Gascho. 2017 VirtoScan-a mobile, low-cost photogrammetry setup for fast post-mortem 3D full-body documentations in x-ray computed tomography and autopsy suites. *Forensic science, medicine, and pathology* 13(1):34-43.
- Landeschi, Giacomo, Bjorn Nilsson, and Nicolo Dell'Unto. 2016 Assessing the Damage of an Archaeological Site: New Contributions from the Combination of Image-Based 3D Modelling Techniques and GIS. *Journal of Archaeological Science: Reports* 10: 431-440.
- Linder, Wilfried. 2003 *Digital Photogrammetry: Theory and Applications*. Springer, Berlin, Germany.
- Lynch, Elizabeth M., Neffra A. Matthews, and Tommy A. Noble. 2017 Unraveling the Enigma of Prehistoric Bedrock Ground Stone Features on the Chaquaqua Plateau, Using Close-Range Photogrammetry. *Quaternary International* 439:50-68.
- Majid, Zulkepli, Albert K. Chong, Anuar Ahmad, Halim Setan, and Abdul Rani Samsudin. 2005 Photogrammetry and 3D Laser Scanning as Spatial Data Capture Techniques for a National Craniofacial Database. *The Photogrammetric Record* 20(109): 48-68.
- Maksymowicz, Krzysztof, Wojciech Tunikowski, and Jacek Kosciuk. 2014 Crime event 3D reconstruction based on incomplete or fragmentary evidence material-case report. *Forensic science international* 242: e6-e11.

- Mann, Robert W., William M. Bass, and Lee Meadows. 1990 Time Since Death and Decomposition of the Human Body: Variables and Observations in Case and Experimental Field Studies. *Journal of Forensic Sciences* 35(1):103-111.
- Mathews, Neffra A. 2008 *Aerial and Close-Range Photogrammetric Technology: Providing Resource Documentation, Interpretation, and Preservation*. U.S. Department of the Interior, Bureau of Land Management, Denver, CO.
- Mayer, Cedric, Luisa Maria Gomes Pereira, and Thomas P. Kersten. 2018 A Comprehensive Workflow to Process UAV Images for the Efficient Production of Accurate Geo-Information. In IX National Conference on Cartography and Geodesy 1-8.
- Milliet, Quentin, Olivier Delemont, and Pierre Margot. 2014 A Forensic Science Perspective on the Role of Images in Crime Investigation and Reconstruction. *Science and Justice* 54:470-480.
- National Research Council. 2009 *Strengthening Forensic Science in the United States: A Path Forward*. Washington DC. The National Academics Press.
<https://doi.org/10.17226/12589>.
- Novotny, Anna C. 2019 Implementing Photogrammetry in Three Bioarchaeological Contexts: Steps for In-Field Documentation. *Advances in Arhcaeological Practice* 7(1): 87-96.
- Peng, Fei, Sam C. Lin, Jialong Guo, Huimin Wang, and Xing Gao. 2017 The Application of SfM Photogrammetry Software for Extracting Artifact Provenience from Paleolithic Excavation Surfaces. *Journal of Field Archaeology* 42(4): 326-336.
- Pierdicca, Roberto. 2018 Mapping Chimu's Settlements for Conservation Purposes Using UAV and Close Range Photogrammetry. *The Virtual Reconstruction of Palacio Tschudi, Chan Chan, Peru. Digital Applications in Archaeology and Cultural Heritage* 8: 27-34.
- Rieke-Zapp, Dirk, Alexander Reiterer, Catherine Berger, and Bastian Bommer. 2009 The Application of Photogrammetry for Process Quantification in Geomorphology - Examples of Modern Applications. In *Proceedings of RSPSoc Annual Conference* 776:379-387.
- Robinson, Edward M. 2012 *Crie Scene Photography, Second Edition*. Elsevier Press, Burlington, MA.
- Ruotsala, Anni-Helena. 2016 *Digital Close-Range Photogrammetry - A Modern Method to document Forensic Mass Graves*, Master's Thesis, University of Helsinki.
- Samaan, Miriam, Raphaele Heno, and Marc Pierrot-Deseilligny. 2013 Close-Range Photogrammetric Tools for Small 3D Archaeological Objects. *International Archives of the Photogrammetry, Remote Sensing, and Spatial Information Sciences, Volume XL-5/W2: 549-553*.

- Sansoni, Giovanna, Cristina Cattaneo, Marco Trebeschi, Daniele Gibelli, Pasquale Poppa, Davide Porta, Monica Maldarella, and Massimo Picozzi. 2011 Scene-of-Crime Analysis by a 3-Dimensional Optical Digitizer: A Useful Perspective for Forensic Science. *American Journal of Forensic Medicine and Pathology* 1(32): 280-286.
- Schultz, John J., and Tosha L. Dupras. 2008 The Contribution of Forensic Archaeology to Homicide Investigations. *Homicide Studies* 12(4): 399-413.
- Slot, Liselott, Peter K. Larsen, and Niels Lynnerup. 2014 Photogrammetric Documentation of Regions of Interest at Autopsy - A Pilot Study. *Journal of Forensic Science* 59(1): 226-230.
- Thali, Michael J., Marcel Braun, and Walter Bruschewiler. 2000 Matching Tire Tracks on the Head Using Forensic Photogrammetry. *Forensic Science International* 113: 281-287.
- Thali, Michael J., Marcel Braun, and Richard Dirnhofer. 2003 Optical 3D Surface Digitizing in Forensic Medicine: 3D Documentation of Skin and Bone Injuries. *Forensic Science International* 137: 203-208.
- Thomas, Hugh. 2017 A Methodology for Combining Terrestrial and Aerial Photographs to Create High Resolution Photogrammetric Models of Large-Scale Archaeological Sites: A Case Study for Methone, Greece. *Journal of Archaeological Science: Reports* 16: 27-33.
- Urbanova, Petra, Mikolas Jurda, Tomas Vojtisek, and Jan Krajsa. 2017 Using Drone-Mounted Cameras for On-Site Body Documentation. *3D Mapping and Active Survey. Forensic Science International* 281: 52-62.
- USGS National UAS Project Office. 2016 Unmanned Aircraft Systems Data Post-Processing. Accessed Jun 19, 2019. <https://search.usa.gov/search?affiliate=nctc.fws.gov&query=Unmanned+Aircraft+System+s+Data+Post-Processing.>
- USGS National UAS Project Office. 2017 Agisoft PhotoScan Workflow. Accessed April 9, 2019. [Uas.usgs.gov](http://uas.usgs.gov).
- Villa, Chiara, Nicolaj F. Hansen, Kamilla M. Hansen, Hans P. Hougen, and Christina Jacobsen. 2018 3D Reconstructions of a Controlled Bus Bombing. *Journal of Forensic Radiology and Imaging* 12: 11-20.
- Volk, M.I., T.S. Hocktor, B.B. Nettles, R. Hilsenbeck, F.E. Putz, and J. Oetting. 2017 Florida land use and land cover change in the past 100 years. In E.P. Chassignet, J.W. Jones, V. Misra, and J. Obeysekera (Eds.). *Florida's climate: Changes, variations and impacts* (pp. 51-82). Gainesville, FL: Florida Climate Institute.
- von Ubel, Max. 2020 Best Photogrammetry Software (Some Are Free). All3DP, April 14, 2020. <https://all3dp.com/1/best-photogrammetry-software/>.

- Yamafune, K., R. Torres, and F. Castro. 2017 Multi-Image Photogrammetry to Record and Reconstruct Underwater Shipwreck Sites. *Journal of Archaeological Method and Theory* 24: 703-725.
- Zancajo-Blazquez, Sandra, Diego Gonzalez-Aguilera, Higinio Gonzalez-Jorge, and David Hernandez-Lopez. 2015 An Automatic Image-Based Modelling Method Applied to Forensic Infography. *PLOS One* 10(3): e0118719.
- Zhan, Zongqian and Jianqing Zhang. 2006 Application of digital photogrammetry in surveying and mapping of the traffic accident site. *Journal of Highway and Transportation Research and Development* 10:147-150.